/N-02
158803
p-133

NASA Contractor Report 177612

Rotor Design Optimization Using a Free Wake Analysis

Todd R. Quackenbush, Alexander H. Boschitsch, Daniel A. Wachspress, and Kiat Chua

CONTRACT NAS2-13092
April 1993

National Aeronautics and
Space Administration

NASA Contractor Report 177612

Rotor Design Optimization Using a Free Wake Analysis

Todd R. Quackenbush, Alexander H. Boschitsch, Daniel A. Wachspress, and Kiat Chua

Continuum Dynamics, Inc.
P.O. Box 3073
Princeton, NJ 08543

Prepared for
Ames Research Center
CONTRACT NAS2-13092
April 1993

National Aeronautics and
Space Administration

Ames Research Center
Moffett Field, California 94035-1000

TABLE OF CONTENTS

NOMENCLATURE

A	matrix of blade-on-blade influence coefficients local area of cross-section of finite element
B	Hessian matrix approximation constructed according to Eqs. (5-16) and (5-17)
B_1, B_2, B_3	matrix quantities defined in Eqs. (4-14)
c_l	sectional 2D lift coefficient
$c_{l_{max}}$	maximum sectional 2D lift coefficient
C_T	thrust coefficient, $T/\rho_a \pi R^2 (\Omega R)^2$
C_P	torque coefficient, $P/\rho_a \pi R^3 (\Omega R)^2$
$\underline{d}$	vector of design variables, $\{ d_i \}^T$
E	Young's modulus
$\underline{f}$	nodal force vector
$\underline{f}$	body force vector due to blade rotation, $\{f_x , f_y , f_z\}^T$, defined in Eq. (4-20)
$\underline{f}^a$	vector of aerodynamic force per unit length, $\{ f_x^a , f_y^a , f_z^a \}^T$ along local x, y, and z axes.
$\underline{f}^{aero}$	nodal force vector due to aerodynamic loads
$\underline{f}^{rot}$	nodal force vector due to blade rotation
$\underline{F}$	integrated force vector, $\{F_x, F_y, F_z\}^T$, due to blade rotation defined in Eq. (4-23a)
g_j, g_k	inequality and equality constraint respectively
G	shear modulus
$\underline{I}, \underline{J}, \underline{K}$	unit vectors in XYZ coordinates
I_d	set of design variables
I_h	set of holonomic constraints
J	objective (cost) function
J_G , J_i	multi-objective cost function and single objective cost function respectively
j_A	set of active constraints
K	finite element stiffness matrix
K_E	contribution of material stiffness properties to K
k_R	fraction of blade radius from peak circulation to blade tip
K_R	contribution of distributed centrifugal forces to K

K_G	contribution of geometric stiffening to K
l	length of finite element
L	Lagrangian defined in Eq. (5-12)
l_i	lower bound imposed upon state variable, x_i
m	no. of constraints ($= m_i + m_e$)
$\underline{m}$	moment vector about elastic axis due to blade rotation defined in Eq. (4-22)
$\underline{M}$	integrated moment vector, $\{M_x, M_y, M_z\}^T$, due to blade rotation defined in Eq. (4-23b)
$\underline{m}^a$	vector of aerodynamic moment per unit length, $\{ m_x^a, m_y^a, m_z^a \}^T$, along local x, y, and z axes.
m_i, m_e	no. of inequality and equality constraints respectively
n	dimension of the state vector, $\underline{X}$
P	power
P_i, P_p	power arising from induced drag and profile drag respectively
q	optimization step
$\underline{q}$	vector of generalized finite element nodal deformations
Q	dynamic pressure downstream of a rotor blade (kPa) in Figs. 2-8 and 2-9 or rotor torque
$Q_{(\bullet)}$	influence coefficient w.r.t. (•)
r	radial distance from rotor hub
R	rotor radius (m)
$\underline{R}$	position vector in global reference frame (blade axes), $\{X, Y, Z\}^T$
R_X, R_Y, R_Z	rotations due to deformation about the global XYZ axes respectively
$\underline{s}$	nodal deformation vector
s_j	slack variables
SC	scaling terms for variable, x_i
SL	segment X-length
T	rotor thrust
$[T_{GL}]$	matrix relating local finite element displacement vector to the corresponding global quantities
$[T_{rot}]$	transformation matrix relating local finite element axes xyz and rotating blade axes XYZ defined in Equation 4-3
u, v, w	local finite element deformations along the x, y, and z directions respectively.

U, V, W	global finite element deformations along X, Y, and Z directions respectively
u_i	upper bound imposed upon state variable, x_i
$\underline{w}$	downwash at blade vortex lattice control points
w_i	cost function weighting terms used in Eqs. (5-22) and (5-23)
W^i, W^e	internal and external virtual work respectively
xyz	local axes for a finite element
$\underline{x}_c$	vector of wake collocation normal and binormal positions
$\underline{X}$	state vector, $\{ x_i \}^T$ used in optimization
XYZ	global (rotating blade) coordinates
$X_0Y_0Z_0$	XYZ position of the origin of local finite element axes
α	sectional angle of attack (rad.)
$\Delta\alpha_s$	angle of attack increment post stall
β	angle between the local y and η axes
γ	anhedral angle of beam finite element
$\underline{\gamma}$	vector of bound circulations for the vortex lattice
Γ	bound circulation
$\bar{\Gamma}_c$	circulation non-dimensionalized by ΩR^2
$\gamma_{x\eta}$, $\gamma_{x\zeta}$	engineering shear strains defined in Eqs. (4-11b,c)
$\varepsilon_{x\eta}$, $\varepsilon_{x\zeta}$	strain tensors defined in Eqs. (4-11b, c)
ε_{xx}	axial strain defined in Eq. (4-11a)
η, ζ	principal axes of the cross-section
θ	local twist displacement of finite element
λ_j, λ_k	Lagrange multipliers associated with inequality constraint, g_j, and equality constraint, g_k, respectively
Λ	sweep angle of beam finite element
μ_1, μ_2	Lagrange multiplier vectors associated with the lower and upper bounds respectively on $\underline{X}$
ξ	normalized coordinate, x/l
ρ	density of the blade material
ρ_a	air density
$\sigma_{x\eta}$, $\sigma_{x\zeta}$	shear stresses defined in Eqs. (4-15b,c)
σ_{xx}	axial stress defined in Eq. (4-15a)
$\{\Phi_2\}$,$\{\Phi_3\}$	vector of shape functions defined in Eq. (4-6)
$[\Phi]$	shape function matrix defined in Eq. (4-7)

$\Psi(x,\eta,\zeta)$	Saint Venant warping function relating out-of-plane warping to torsional displacement defined in Eq. (4-12)
Ω	rotor rotation frequency (radians/second)

$(\bullet)_{ea}$	refers to elastic axis
$(\bullet)_G$, $(\bullet)_L$	refers to global axes and local axes respectively
$(\bullet)_{ie}$	refers to element, ie
$(\bullet)_{,x}$	derivative w.r.t. x
$(\bullet)^T$	transpose operation
$(\bullet)^*$	denotes optimal quantity
$()'$	derivative w.r.t. ξ
$\delta(\bullet)$	variation operator
$\Delta(\bullet)$	change in argument per optimization step, as well as change in argument per EHPIC/HERO step
$\nabla(\bullet)$	gradient operator, $\partial(\bullet)/\partial\underline{X}$

1. INTRODUCTION

1.1 Background of the Present Effort

Design optimization is an issue of continuing importance in a variety of aeronautical applications, including rotorcraft performance analysis. Developing an effective compromise design that can meet the requirements of rotor performance in hover and in climb or high speed axial flight is an exceptionally difficult problem. Hover itself remains an important design point because of the critical role it plays in sizing the engine and establishing rotor disk loading and the blade twist distribution. Moreover, the axial flight condition has become even more critical, since the success of present and proposed tiltrotor designs depends on efficient performance of lifting rotors in propeller mode. The complexity of the problem increases still further when structural and dynamic constraints are considered. The primary objective of this effort was to develop a comprehensive design optimization capability suitable for analyzing both hover and axial flight conditions in modern helicopter and tiltrotor configurations.

An essential prerequisite for a practical and effective optimization analysis is for a refined, flexible, and well-validated hover performance code to be used as the basis of the performance calculation. The task of developing computational tools to reliably analyze rotor performance has been under study for many years. Much of the work in this area has centered around efforts to approximate crucial rotor wake effects through generalizations of vortex wake trajectories from empirical data (Refs. 1 and 2) or through interpolations between 'representative' free vortex computations (Ref. 3). It has long been clear that the preferred approach is the explicit computation of full free wake vortex flows; this approach avoids reliance on particular data sets and yields force-free, physically valid wakes which enhance confidence in performance predictions. The next section will summarize previous work in the development of free wake analyses as well as describe the formulation implemented here.

A second requirement for a successful optimization analysis is that it must efficiently evaluate candidate designs with minimal resort to repeated calls of the computationally expensive open-loop performance analysis. It is in this regard that the influence coefficient approach proves highly advantageous. An analysis incorporating this approach, designated EHPIC (Evaluation of Hover Performance using Influence Coefficients), has proved to be the ideal foundation for a free wake optimization routine, since its formulation permits straightforward evaluation and exploitation of information on the gradients in performance due to design changes. The results presented below will show how an optimization analysis based on influence coefficients can perform efficient exploration of design space without sacrificing the refined physical model associated with free wake treatments.

Previous reports and papers (Refs. 4 and 5) have described exploratory work on this topic, involving computations of improved performance on representative rotor configurations using a loose coupling of the EHPIC code to a linear optimization analysis. While these demonstration calculations were encouraging evidence of the feasibility of developing an optimization code based on EHPIC, they were restricted to using twist as a design variable and lacked the flexibility to realistically constrain the evolving designs. It was thus recognized that considerable additional development and validation work was required to implement a useful, practical optimization code.

References 6-9 summarize extensive performance validation efforts undertaken with the EHPIC code. These references describe correlation studies involving over thirty separate rotor configurations, including tiltrotor designs, conventional main rotors, and tail rotors. In general, these studies achieved quite accurate correlation with minimal resort to "dialing" of model parameters. This work in OGE (Out of Ground Effect) hover calculations has been supplemented by enhancement of the original EHPIC (Mod 0.0) code (Ref. 9) to include a ground plane to allow IGE (In Ground Effect) calculations (Ref. 10). Validation of IGE performance and wake geometry predictions discussed in References 10 and 11 has also been encouraging.

Thus, the underlying EHPIC hover model has undergone substantial testing and refinement since the original work described in Reference 9, but still other improvements were judged desirable to improve the flexibility and physical fidelity of the code. Many of these new features are described in Sections 2, with additional details on implementation and use provided in Reference 12. The new features of the model include: a provision for lift limitation due to airfoil stall; direct calculation of wake-induced velocity at specified points; refinements in vortex core modeling; research on vortex/blade encounter loading; and significant CPU reduction through the streamlining of influence coefficient evaluations. Sections 3 and 4 describe still more substantial improvements to the baseline EHPIC analysis, including a provision for high-resolution roll-up of tip vortices and computation of static structural deflection. Later sections directly take up the topic of the optimization algorithms implemented as well as the calculations undertaken to validate the functionality and capabilities of these algorithms.

1.2 Review of Previous Work in Rotor Design Optimization

There exists a large body of literature on numerical optimization procedures. Recent reviews of aerospace- and rotorcraft-oriented applications of numerical optimization give evidence of the maturity of these techniques (Refs. 13-14). As for particular applications, Moffitt and Bissell (Ref. 15) undertook a general examination of rotor airloads in both hover and forward flight using a prescribed wake aerodynamic model with circulation coupling. Their aim was to find airload distributions that led to a minimum power required for a specified thrust. Nagashima and Nakanishi (Ref. 16) studied hover performance optimization for coaxial rotors, employing both a closed-form "generalized momentum" model of the wake as well as a simplified free wake model based on vortex rings. Walsh, Bingham, and Riley (Ref. 17) and Chattapodhyay, Walsh and Riley (Ref. 18) describe the assembly of several existing aerodynamic and vehicle trim models and a commonly available optimization routine (CONMIN) into a broadly applicable blade design optimizer for hover and forward flight. This work is part of a larger effort to develop a multidisciplinary design optimization for rotorcraft (Adelman and Mantay, Ref. 19) which has been directed at achieving appropriate compromise designs across a wide range of performance measures. This in turn has been supplemented by more specialized studies performed by Chattapodhyay and McCarthy (Ref. 20).

Nearly all of the studies mentioned above rely on qualitatively similar approaches; an objective function (e.g., vibratory load levels or hover figure of merit) is defined along with a set of design parameters to be varied. Limitations are placed on the variations allowed in these quantities in the form of inequality constraints and initial estimates of parameter values to meet the specified performance levels are made. Using approximations to the actual nonlinear relations governing the objective function, the design parameters are varied in the vicinity of the initial estimate to reach the desired level of this function. The more recent work, (Refs.19 and 20), has expanded the scope of such methods to address multidisciplinary optimization efforts involving the simultaneous maximization or minimization of complex objective functions composed of weighted measures of performance (e.g. hover figure of merit and blade dynamic frequency placement, or climb power and noise signature).

All this work represents a broad range of accomplishment in design optimization, although as a general rule these efforts have featured simplified aerodynamic models in their performance calculations (e.g., strip theory and prescribed wake models). This doubtless has been a response to the need to provide designers with computationally efficient tools; however, now that more and more computational power is becoming routinely available, it is appropriate to employ more advanced methods. Simplified models lack the generality, accuracy and adaptability of the more advanced treatments now available and so their use in an optimization analysis undermines confidence in the true optimality of the designs computed. The advantage of the current effort is that the advanced free wake analysis embodied in the EHPIC code can be utilized to produce a more comprehensive, reliable and flexible optimization treatment. Furthermore, EHPIC's influence coefficient approach helps ameliorate potential increases in CPU time because in the course of its own solution it calculates many of the derivatives required by the optimization algorithm.

2. HOVER PERFORMANCE PREDICTIONS USING A FREE WAKE ANALYSIS

This section recapitulates the development of the EHPIC code and introduces the important concepts that were carried over into the current effort. The evolution of the EHPIC code from the Mod 0.0 version originally delivered to NASA in 1987 to the later Mod 1.0 and Mod 2.0 versions is summarized. Also described in this section are the major modifications that were incorporated in EHPIC/HERO to enhance performance and to adapt the EHPIC analysis to the tasks associated with design optimization.

2.1 The Influence Coefficient Approach to Free Wake Analysis

Early efforts to develop free wake hover models using time domain calculations (Refs. 21 and 22) were hampered by long computation time and poor (or nonexistent) convergence due to the inherent instability of the hovering rotor wake (Fig. 2-1). Reference 9 describes the development of an influence coefficient relaxation approach to the free wake problem that determines the wake geometry while circumventing the convergence problems associated with the time-marching simulations. As mentioned previously, the EHPIC code has produced accurate performance predictions for a wide variety of rotor systems in hover, and has proved to be flexible and robust. EHPIC also includes curved vortex elements (Reference 23) in the model of the rotor wake to enhance both the efficiency and the accuracy of the computation.

The general objective of a free wake hover analysis is to find the wake geometry that satisfies two conditions: first, that the wake filaments are in free motion; and second, that the flow tangency condition is satisfied on the blade. To achieve the free motion condition, the wake filament trajectories must be tangent to the local velocity vector evaluated on the filament when viewed in a rotating reference frame, i.e., there will be no crossflow velocity components at any point on the filaments under force free conditions. The coupled free wake/lifting surface hover analysis in EHPIC proceeds by first making an initial guess for the blade loads and the wake geometry. This initial guess will not, in general, satisfy the required conditions, and so must be adjusted in a succession of solution steps. To accomplish this, the independent variables in the problem (the bound circulation at stations along the blade and the vortex wake position coordinates) are systematically perturbed, and the effect of these perturbations on the dependent variables (the downwash on the blade and crossflow velocities in the wake) are summed and formed into influence coefficients (Fig. 2-2). These coefficients allow the construction of a set of simultaneous linear equations in matrix form which predict the change in dependent variables due to the changes in independent variables. The coefficient array so formed can be used to null the crossflow and downwash velocities by inverting it and multiplying it by the vector of residual velocities. The influence coefficient array appears in a linear system of equations in the following form:

$$\begin{bmatrix}\Delta\vec{q}\\ \Delta\vec{w}\end{bmatrix} = \begin{bmatrix} Q_{qx}\,Q_{q\gamma}\\ Q_{wx}\,Q_{w\gamma}\end{bmatrix}\begin{bmatrix}\Delta\vec{x}\\ \Delta\vec{\gamma}\end{bmatrix} \qquad (2\text{-}1)$$

The independent variables on the right hand side are, respectively, the position perturbations and bound circulation perturbations from the initial state, while the dependent variables on the left hand side represent the crossflow velocities in the wake and the downwash at the blade.

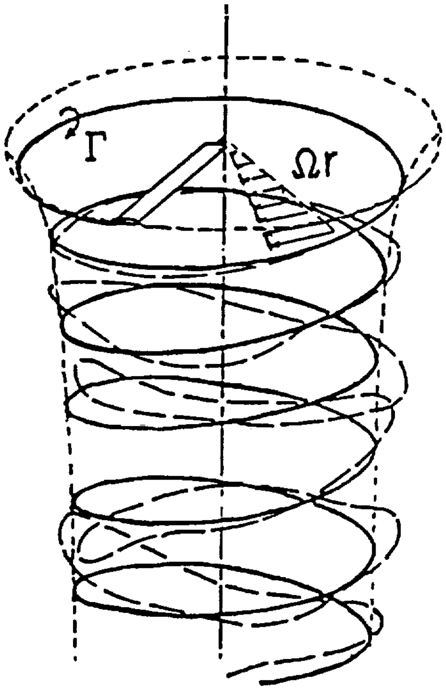

Figure 2-1. Typical form of time domain instabilities observed in free vortex calculations of hovering rotor wakes (dashed line); solid line represents the idealized contracting wake solution for this one-bladed rotor.

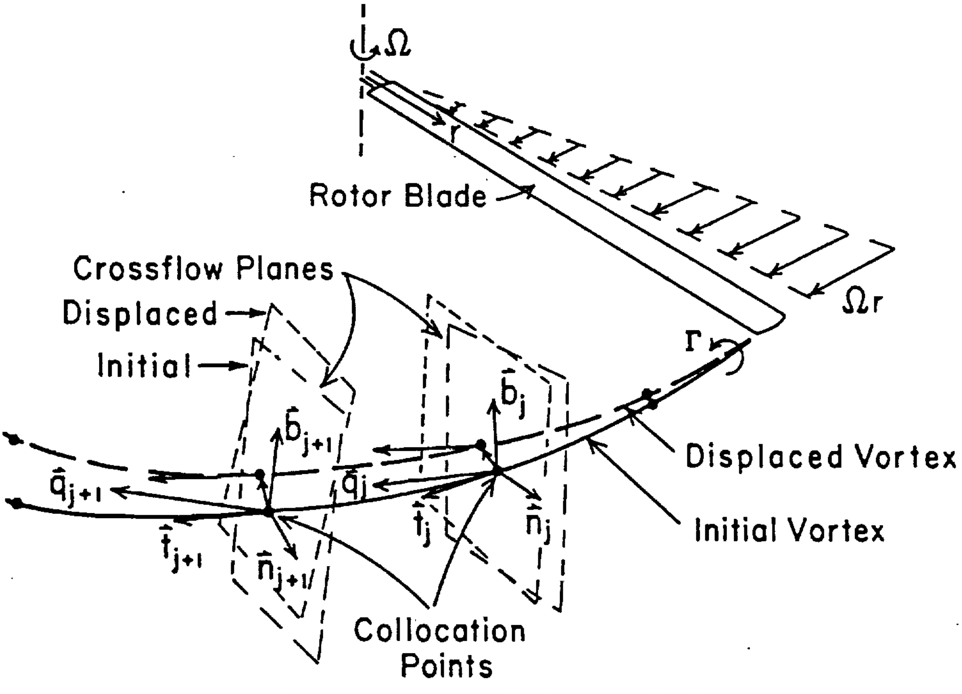

Figure 2-2. Method of displacing a vortex to eliminate velocity components in planes normal to the vortex curve. Equilibrium state is zero crossflow velocity in every plane.

These variables, of course, represent perturbations about an initial guess, which in general features some nonzero residual velocities on the left hand side. Were the problem purely linear, inverting this matrix and multiplying it by the residual velocity vector would yield a vector of wake displacements and circulation perturbations that would exactly null the velocities in question, i.e.,

$$\begin{bmatrix} \Delta\vec{x} \\ \Delta\vec{\gamma} \end{bmatrix} = - \begin{bmatrix} Q_{qx} & Q_{q\gamma} \\ Q_{wx} & Q_{w\gamma} \end{bmatrix}^{-1} \begin{bmatrix} \overrightarrow{q_{res}} \\ \overrightarrow{w_{res}} \end{bmatrix} \tag{2-2}$$

In general, the process must be repeated due to the inherent nonlinearity of the problem, and only small fractions of the residual velocities are nulled in each iteration. In practice, this approach has been found to have robust convergence properties, despite the complexity of the relaxation procedure. For most rotor configurations with up to ten wake filaments per blade, convergence is achieved after ten to twenty relaxation steps (Fig. 2-3). These solutions, while they are self-preserving vortex flows, can be shown to possess time-domain instabilities that preclude the success of time-marching calculations (Ref. 9).

In the EHPIC code, the wake vortex filaments are represented by curved vortex elements which provide an efficient means to perform the Biot-Savart integrations necessary for the evaluation of wake-induced velocities (Fig. 2-4). A vortex lattice/lifting surface analysis is used to evaluate the thrust and induced drag on the rotor. An array of thin lifting vortex quadrilaterals are used to model each blade, and the relaxation solution produces a vector of bound circulation values that null the downwash at the control point at the center of each quad. Using the local values of free stream and induced velocity, the Joukowski law is applied to find the force and moment on each lattice element. This procedure also produces a spanwise lift coefficient distribution that is used, along with the local Mach number, in a look-up scheme that provides the profile drag coefficient of that section.

One advantage of the influence coefficient approach is that it finds the physically correct, self-preserving wake geometry without the instabilities and consequent lack of convergence of earlier methods that convected the wake in a time-marching manner. Furthermore, once a converged solution has been obtained, adjacent solutions that are almost linearly close along a performance curve are readily obtained with only a few relaxation steps, eliminating the need to wash out the transients occurring in time-marching schemes.

2.2 Evolution of the EHPIC Code

The EHPIC code has evolved considerably since the original work summarized in Reference 9. This initial effort was directly purely at obtaining performance solutions for isolated rotors operating out of ground effect, and the resulting code was designated the Mod 0.0 version. Subsequent development work sponsored by NASA to upgrade the original code led to three major modifications: implementation of a ground plane model to allow for computations in ground effect; incorporation of an eigenanalysis package to permit evaluation of the linearized time domain stability of converged configurations; and substantial revision of the original coding to reduce the code's CPU requirements on vector processing computers. This version was designated Mod 1.0, and its development is described in detail in Reference 10.

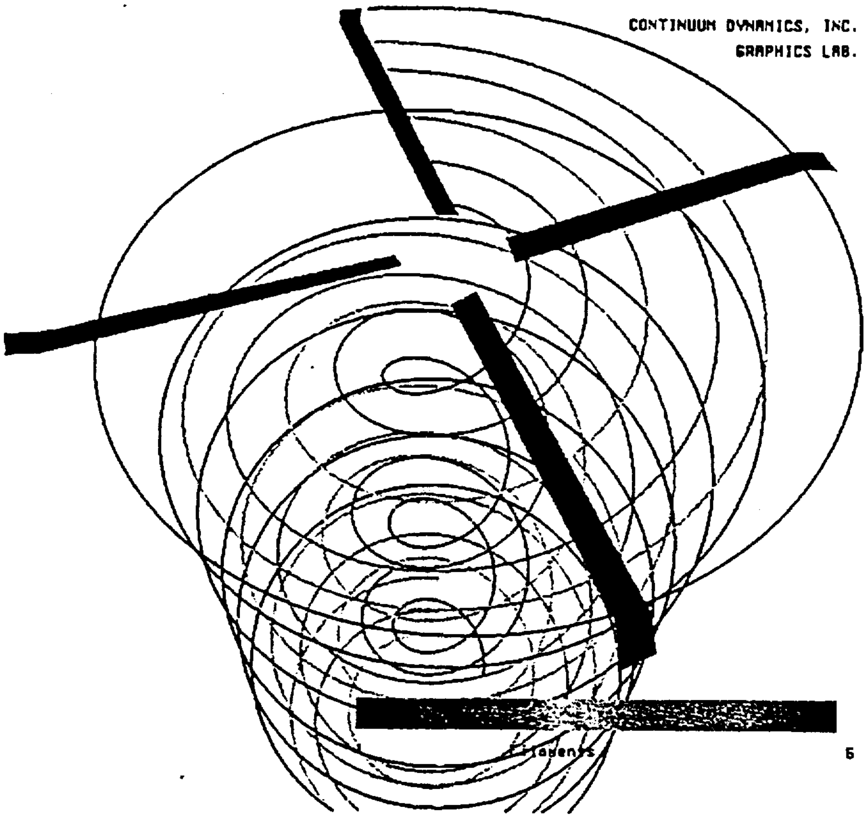

Figure 2-3. Typical converged rotor wake configuration for the EHPIC code (six free wake filaments trailing from each blade). (Wake from only one blade shown.)

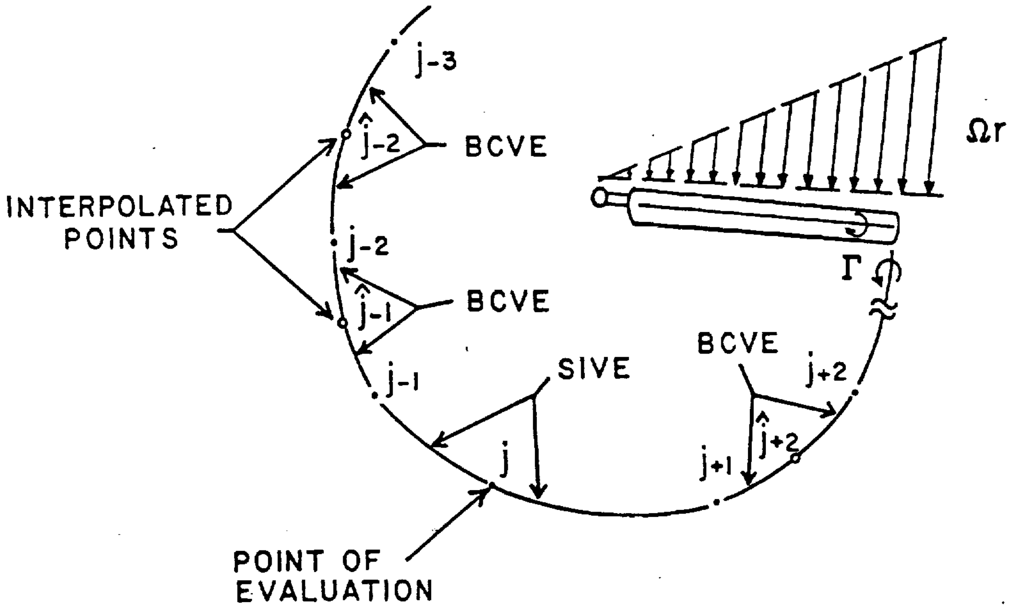

Figure 2-4. Typical arrangement of elements used to discretize trailing vortex filaments for wake-on-wake velocity calculations. The formulation of parabolic Basic Curved Vortex Elements (BCVE's) and Self-Induction Vortex Elements (SIVE's) given in Reference 23.

The ground plane model implemented in Mod 1.0 consists of an image system of vortices located symmetrically opposite the free vortex elements in the physical wake. A prescribed wake model completes the transition from the freely distorting filaments to an efficient far wake representation. References 10 and 11 both contain discussions of wake geometry and performance results obtained with the ground effect model.

This vectorized EHPIC Mod 1.0 variant achieved roughly a factor of four in computation time reduction over Mod 0.0 when implemented on a CRAY Y-MP. Additional computation time reductions - independent of computational platform - have been realized in a Mod 2.0 version developed under an internal effort at Continuum Dynamics. This version incorporates a broad range of efficiency enhancements, primarily limiting the frequency of updates of the influence coefficient array. Mod 2.0 contains the same physical model as Mod 1.0, but can run three to four times faster on the same machine. The speed-up in Mod 2.0 is independent of (serial or vector) platform, so a Mod 2.0 calculation operating on a CRAY Y-MP or similar vector processor can run over an order of magnitude faster than the original EHPIC Mod 0.0.

The Mod 2.0 variant was the starting point for the development of EHPIC/HERO described here. (Unless otherwise specified, any subsequent references to 'the EHPIC code' should be understood to refer to Mod 2.0). During the evolution of the EHPIC/HERO code from the baseline EHPIC analysis, a variety of extensions and revisions were incorporated independent of any optimization functions to relieve earlier limitations on the analysis and effect improvements in the consistency of the model, or simply to make the analysis more convenient to use. The remainder of this section describes the implementation of the most significant of these modifications, while discussion of two major extensions - the calculation of tip vortex roll-up and the implementation of a structural deformation model - is reserved for subsequent sections.

2.3 Calculation of Aerodynamic Loading

2.3.1 Vortex lattice model

In EHPIC and EHPIC/HERO, thrust and induced torque are computed using a vortex lattice formulation similar to that described in Reference 24. The present model allows substantial flexibility in the specification of the blade's planform so that complex designs may be accommodated. Currently, the lattice can be divided into as many as fifteen different regions, with separate linear distributions of twist, taper, and sweep within each. The spacing of the quadrilaterals in a vortex lattice analysis is an important consideration, as is discussed in Reference 25. The judicious selection of the density, spacing, and orientation of the quadrilaterals can considerably enhance the efficiency and rate of convergence of the blade loading. The current analysis has been provided with sufficient flexibility to arrange essentially arbitrary chordwise and spanwise distributions of lattice elements though the control points are always assumed to lie at the geometric center of the quadrilateral. All of the calculations discussed in this report feature uniform spacing of vortex quadrilaterals both in the chordwise and spanwise directions, unless otherwise noted. (Note: A special semicircle cosine spacing option similar to the Lan Type-B model discussed in Ref. 25 is currently available within the EHPIC/HERO code. The description of the vortex lattice structure in this section does not apply to this option. The semicircle spacing option was not used for any of the results presented in later sections.)

The vortex quadrilateral lattice is drawn in blade coordinates, which have their origin at the rotor hub with Z down along the shaft, X radially outward along the planform, and Y normal to the XZ plane (Figure 2-5). First the blade segments are laid out separately in the XY-plane applying taper and sweep. The lattice is displaced toward the trailing edge by a distance of one quarter of the chordwise length of the leading edge quadrilaterals. For one row of quads and an unswept rectangular planform, this puts the leading edge quadrilateral along the quarter chord line of the blade and the vortex lattice control points (center points of each quad) along the 3/4 chord line of the blade. The lattice is inset from the blade root and tip by a distance equal to a quarter of the width of the last quad at either edge (Ref. 26). For reference purposes, the quarter-chord line of the blade is taken as the line that connects the quarter chord points of each blade section, while the X axis of the blade coordinate frame is the line connecting the hub with the quarter-chord of the root section. The sweep angle for any segment is defined as the angle the local quarter-chord line makes with the X axis. Pitching moment calculations use the local quarter-chord line as a reference axis, however collective pitch is applied about the X axis.

In actual calculations, the order of operations is different than is shown in Figure 2-5; first, taper is applied linearly from root to tip along each segment. Then sweep is applied by displacing each segment toward its trailing edge (+Y-direction); the sweep angle is the angle between the X-axis and the quarter chord line. The twist gradient is applied by rotating each chord of the lattice about its quarter chord point. Finally, anhedral is applied by displacing each segment downward in the +Z-direction. The resulting vortex lattice structure is stored and written to a file that can be used in a graphical verification of the planform. Also, once assembly of the lattice is complete, it is subjected to a local stretching to account for the effects of compressibility on sectional lift and moment properties, as described in Reference 9; compressibility effects on sectional drag are captured through the look-up procedure described in Section 2.3.2.

In addition to the geometric inputs just described, a camber distribution for the blade may also be specified. Numerical input is used to describe the geometry of the camber line. When camber is present, the lattice itself is not deformed to fit the specified distribution, rather the boundary conditions at the vortex quadrilateral control points are altered to introduce the surface slope into the calculation. However, a certain minimum chordwise density of quadrilaterals is required to resolve the camber distribution; an absolute minimum of three quadrilaterals chordwise should be used, with five or more being desirable. This level of quadrilateral density can create a substantial computational burden. An alternative approach for including empirical zero lift angles is also available for cases where improved computational efficiency is desired. An appropriate rotation of the vector normal to the blade at the control points of each quadrilateral will alter the effective angle of attack of the section and can be used to introduce the shift of the zero lift angle of attack. In this manner, realistic zero lift angles of attack can be introduced into the calculations with only one quadrilateral chordwise. The introduction of the zero lift angle and the option for invoking the pitching moment coefficient from two-dimensional tables are described later.

The solution method used to find the bound circulation given the vortex lattice is essentially a straightforward implementation of the classical approach described in the literature on lattice methods for fixed wing applications (e.g., Ref. 24). Each of the quadrilaterals is examined individually and a mean vector normal to the quadrilateral surface is established as shown in Figure 2-6, which also shows the location of the 'control point' associated with the quadrilateral. Given this and the location and orientation of each of the quadrilaterals on the blade, the velocity induced by the blade lattice on each of the control points is determined, assuming unit strength for each quadrilateral. Then the resulting velocity is resolved in the normal direction at each

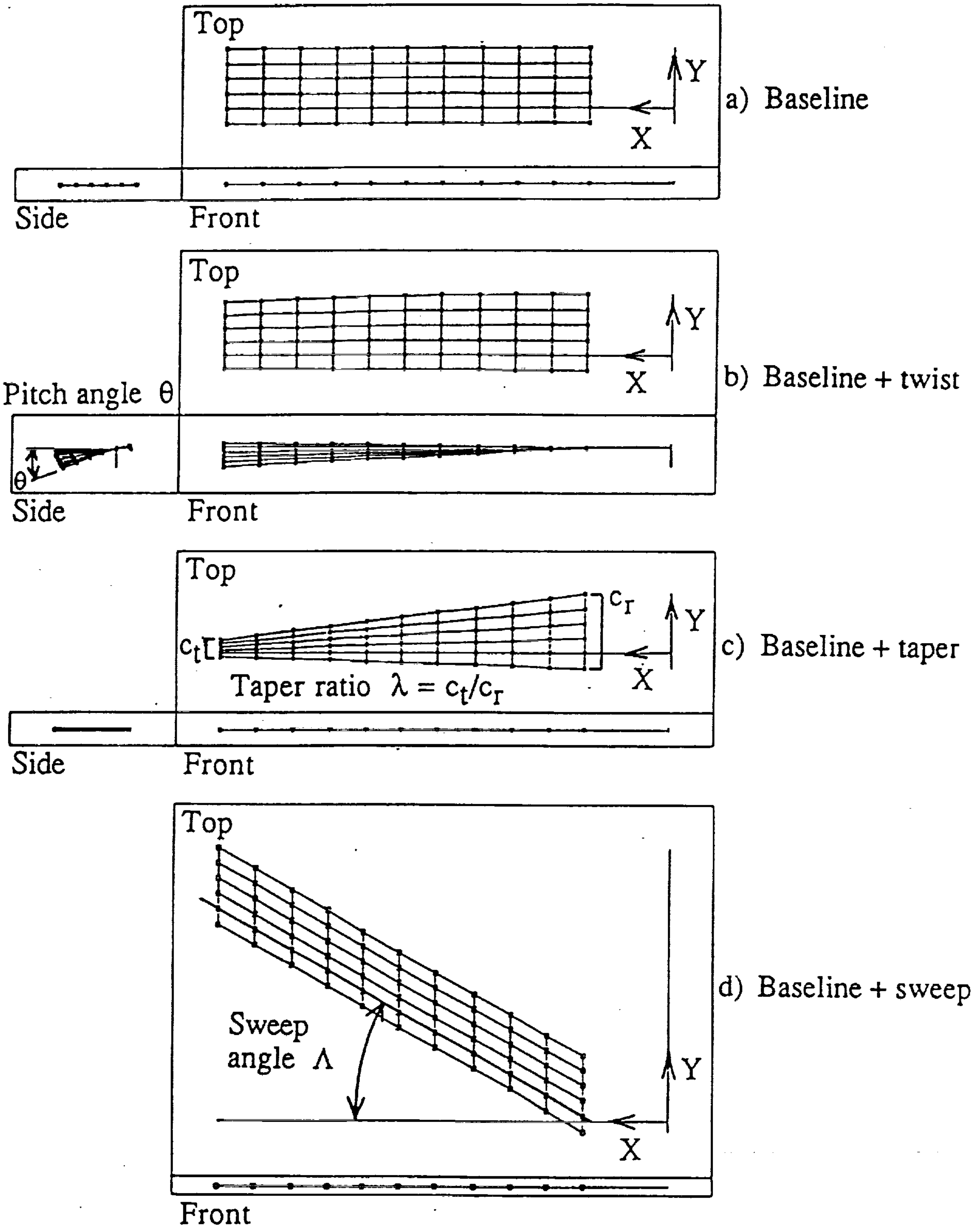

a) Baseline

b) Baseline + twist

c) Baseline + taper

d) Baseline + sweep

Figure 2-5. Sample blade layout: illustration of definition of taper, twist and sweep on a 5 x 20 lattice.

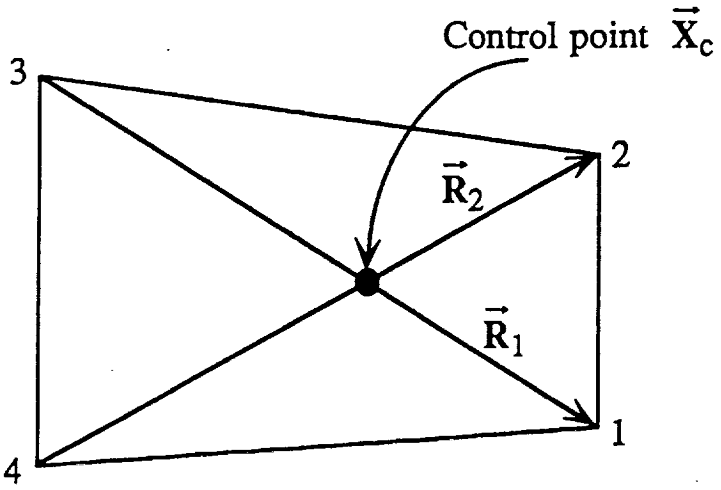

Normal vector at $\vec{X}_c$ is $\vec{n} = \vec{R}_1 \times \vec{R}_2$

$$\vec{X}_c = 0.25\left(\vec{X}_1 + \vec{X}_2 + \vec{X}_3 + \vec{X}_4\right)$$

Figure 2-6. Typical vortex quadrilateral, showing the corner indices and diagonal vectors. Control point found using the mean of the corners. Normal vector defined as indicated.

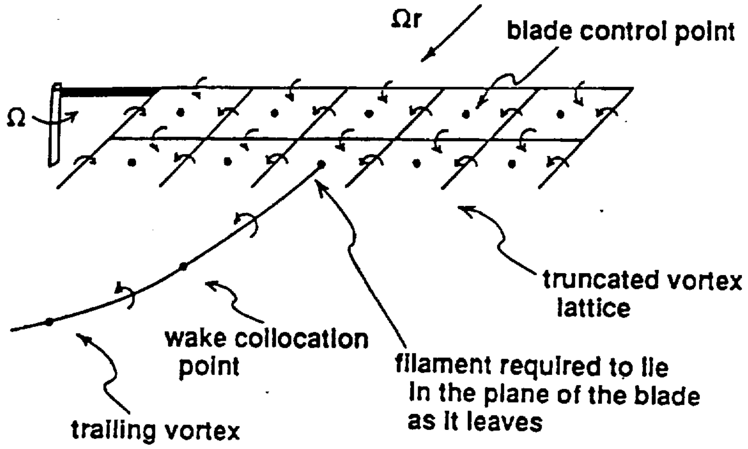

a) implementation in EHPIC

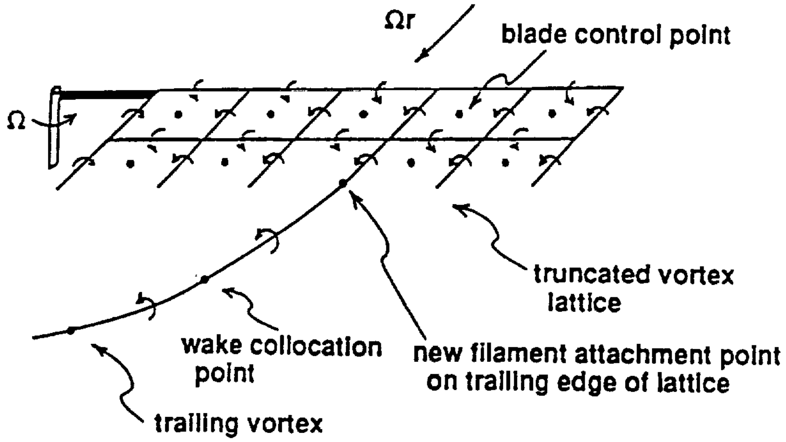

b) new implementation in EHPIC/HERO

Figure 2-7. Schematic of the blade/wake junction with a single trailing filament.

control point, yielding an array of influence coefficients relating the vector of bound circulations $\underline{\gamma}$ to the vector of downwashes $\underline{w}$ at each control point:

$$\underline{w} = A\underline{\gamma} \tag{2-3}$$

The vector $\underline{\gamma}$ can then be used to solve for the forces and moments on each vortex quadrilateral edge by applying the Joukowski Law , i.e.,

$$\underline{F}_{jk} = \rho\, \gamma_j\, (\underline{q}_{jk} \times \underline{s}_{jk})\, l_{jk} \qquad j = 1, \ldots n \quad k=1,2,3,4 \tag{2-4}$$

Here, $\underline{s}_{jk}$ is the unit vector directed along edge k of quadrilateral j ; l_{jk} is the length of this side, and γ_j is the strength of the quad. The reference velocity $\underline{q}$ for the evaluation of forces is computed at the midpoint of the edge k. The forces on each quad edge are then summed to yield the integrated forces on each blade:

$$\underline{F} = (H\underline{I} + Y\underline{J} + T\underline{K}) = \sum_j \sum_k \underline{F}_{jk} \tag{2-5}$$

Moments exerted by the blade about the sectional quarter-chord reference axis can also be computed:

$$\underline{M} = (L\underline{I} + M\underline{J} + N\underline{K}) = \sum_j \sum_k \underline{F}_{jk} \times \underline{r}_{jk} \tag{2-6}$$

Here, $\underline{r}$ is the vector from the reference axis to the point of action of $\underline{F}$. Moments about the blade root are taken to compute the coning and in-plane deflection, while pitching moments can be computed for each section to use for the calculation of torsional deformation.

It is appropriate here to note a change implemented in EHPIC/HERO involving the blade/wake junction. In EHPIC, the trailing vortex filaments were assumed to be attached to the control points at the trailing edge of the lattice. As described in the outline of the near wake model in Reference 9, the influence of the wake elements attached to the blade are deleted and replaced with an 'overlap' region consisting of an extension of the bound vortex lattice into the near wake. One new aspect of the aerodynamic model in EHPIC/HERO was the implementation of a refined model of the near wake that could be used to replace the overlap model. One step required for the implementation of this high-resolution near wake model (described in the next section) was to arrange a new blade/wake junction, illustrated in Figure 2-7. The filaments now attach to the trailing edge of the vortex lattice; this shift in the release points of the wake can have a noticeable effect on rotor performance, as will be shown in Section 6. The overlap model used in EHPIC may still be invoked, if desired.

2.3.2 Sectional drag and moment characteristics

To introduce forces generated by profile (viscous and pressure) drag into the calculation, the only practical approach at present is the use of two-dimensional airfoil data. In the EHPIC code, the form of the data input required involved tabulated values for sectional drag coefficients as a function of Mach number and lift coefficient. EHPIC/HERO now requires C-81 format tables of lift, drag, and moment coefficients as a function of angle of attack. However, section lift coefficient and Mach number are still the variables used to enter the tables, while angle of attack is simply an intermediate parameter. In the present calculation, the section lift coefficient is computed using the vortex lattice analysis described above, and the C-81 lift coefficient table is entered with this value and the Mach number to find an effective angle of attack for the section. Using this angle as a parameter, the drag coefficient (and, if desired, the moment coefficient) are computed for the local Mach number. The lift coefficient table is also used to find the zero lift angle as well as the maximum section c_l for use in the lift stall calculation described in Section 2.4.

The two-dimensional coefficients are, of course, defined only for a specific airfoil section. Many rotor blades feature more than one section along the span. In the current analysis, as many as ten different sections along the span may be specified. For any given spanwise station, the section coefficients are computed for each of the two airfoils that bound the segment containing the station of interest and then interpolated linearly to the desired point. Similarly, for each Mach number/lift coefficient pair, bilinear interpolation is used to find the appropriate coefficients within each look-up table of drag and moment coefficients. The user has the option of applying pitching moment computations from either the look-up process or through the vortex lattice calculation.

2.4 Modeling of Lift Stall

The original EHPIC model included no provision for limiting the lift generated by the vortex lattice aerodynamic model. EHPIC/HERO incorporates an option to use the empirical information on $c_{l_{max}}$ to preclude unrealistically high lift values. The present stall model works by tilting the vectors normal to the blade surface of quadrilaterals in stalled sections by the amount required to reduce c_l computed without stall to the $c_{l_{max}}$ for the section. This "stall adjustment angle", $\Delta\alpha_s$, is assigned to each blade quadrilateral of the stalled section. Once a section is stalled, the correction angle adjusts to ensure that c_l never exceeds $c_{l_{max}}$. As the calculation proceeds, it is possible for the section to drop out of stall, especially during the design optimization process. In this case, the adjustment angle resets to zero and the section is no longer considered to be in stall.

Even though c_l never increases above $c_{l_{max}}$, it is appropriate for the profile drag to continue to increase as the angle of attack of a stalled section increases. The value of $\Delta\alpha_s$ is exactly the increment of angle of attack of the lattice section over the stall angle. Therefore, when invoking the look-up tables, an angle of attack of $\alpha + \Delta\alpha_s$ is used to compute the drag coefficient. One simplification in the present model is that the section lift coefficient is assumed to stay constant at $c_{l_{max}}$ as the angle of attack is increased beyond stall, rather than decreasing as is typically the case for 2D airfoils. The existence of a multi-valued lift function was found to cause dithering in the optimization calculations for very heavily loaded rotors. Results of demonstration calculations of the stall feature on a realistic rotor configuration is shown in Section 6.

2.5 Scan Plane Calculations

EHPIC/HERO includes a provision for computing the wake-induced velocity at specified sets of scan points in the vicinity of the rotor. The present implementation sets up points lying in "scan planes" at particular azimuth angles relative to the blade. Radial and vertical spacing of points are defined by the user. Thus, planes of "crossflow" velocity data at a given azimuthal location relative to the blade are easily captured, while planes of data normal to the rotor disk can be captured simply by using results from within a large number of such crossflow planes at a particular vertical location. It should be noted that the wake geometry and thus the resulting flow field are at all times assumed to be axisymmetric.

Sample calculations were undertaken to demonstrate and validate the scan plane velocity computations. The data set selected involved the downwash velocity measurements on the .658-scale V-22 rotor described in Ref. 27. For this case, EHPIC/HERO was run with nine filaments trailing from the span. Downwash computations were made in four crossflow planes downstream of the reference blade and then suitably averaged in an attempt to duplicate the time-averaged measurements given in Ref. 27. Two operating conditions were considered, both with a tip speed of 232 m/s (760 fps) and thrust coefficients 0.0117 and .0059. The comparisons of the predictions with the time-averaged data are shown in Figures 2-8 and 2-9. As is evident, the predictions capture the behavior of the measured wake reasonably well, with the exception of a single anomalous point in the center of the measured distribution.

2.6 Determination of Trailing Vortex Strength

Figures 2-10 and 2-11 illustrate the procedure for determining vortex filament strengths in the EHPIC/HERO code. The circulation distribution along the blade is divided up into zones which each correspond to a particular vortex filament. The change in circulation across each zone is assigned to the vortex filament associated with that zone, as shown. In order to have a physically consistent wake model, it is necessary that each filament trail from the centroid of the circulation distribution it represents.

In the original EHPIC code, the zone boundaries were input by the user and remained fixed throughout the calculation. After a calculation was complete, the user typically had to adjust the zone boundaries and vortex release points to ensure that all the circulation generated on the blade was trailed into the wake and that vortex filaments were released from the appropriate centroid positions. Though this scheme works fine for performance calculations at particular operating conditions, it was found to be inadequate for the optimization calculations to be undertaken in this effort. During the optimization process, substantial design changes inevitably lead to changes in the circulation distribution that require the position and strength of the trailing filaments to adjust. Without some form of internal adjustment, the optimization process will almost invariably lead to a non-physical solution.

The EHPIC/HERO code offers two new approaches that allow the wake model to adapt to a varying circulation distribution. These methods are illustrated in Figures 2-10 and 2-11. In both methods, the code determines the circulation zones internally, updating zone boundaries when necessary as the circulation distribution evolves. In the first method, the zone boundaries are placed equidistant between vortex filament release points. Zones on either side of the peak circulation location are treated separately. Hence, if the peak circulation location moves, the zone boundaries will adjust even if the vortex filament release points are fixed, (as shown in Figure 2-10b). The strengths of the vortex filaments adjust to accommodate the changing circulation distribution so that the wake always contains the appropriate amount of circulation. EHPIC/HERO also allows the option to have filament release points move to the centroids of the zones they represent automatically. This usually leads to a physically consistent model once the solution converges. Allowing the filaments to move can slow the optimization process

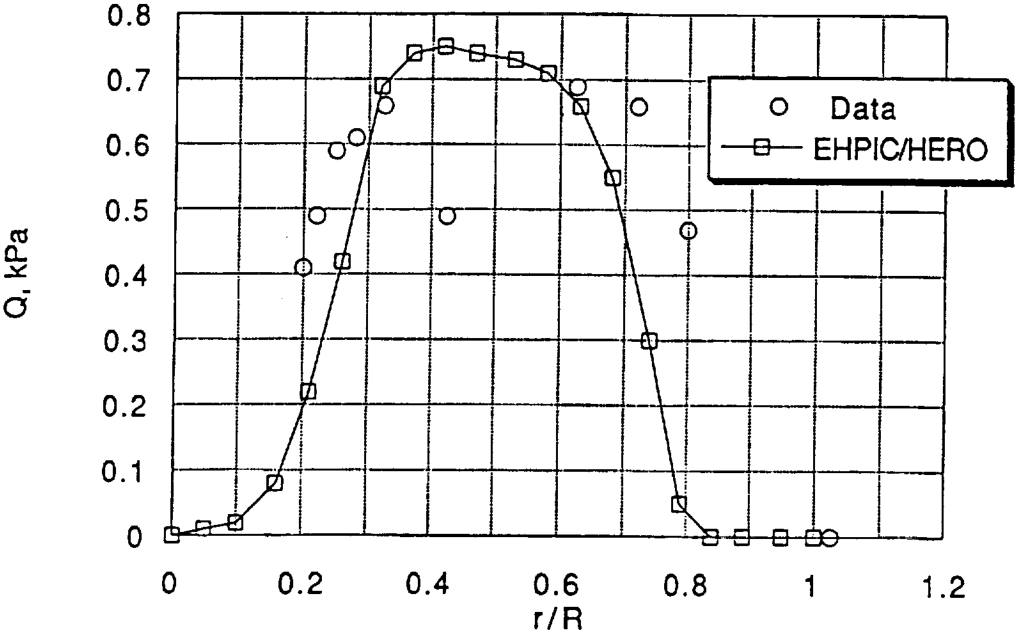

Figure 2-8. Measured and computed dynamic pressure in the wake of a V-22 rotor in hover (thrust coefficient .0117).

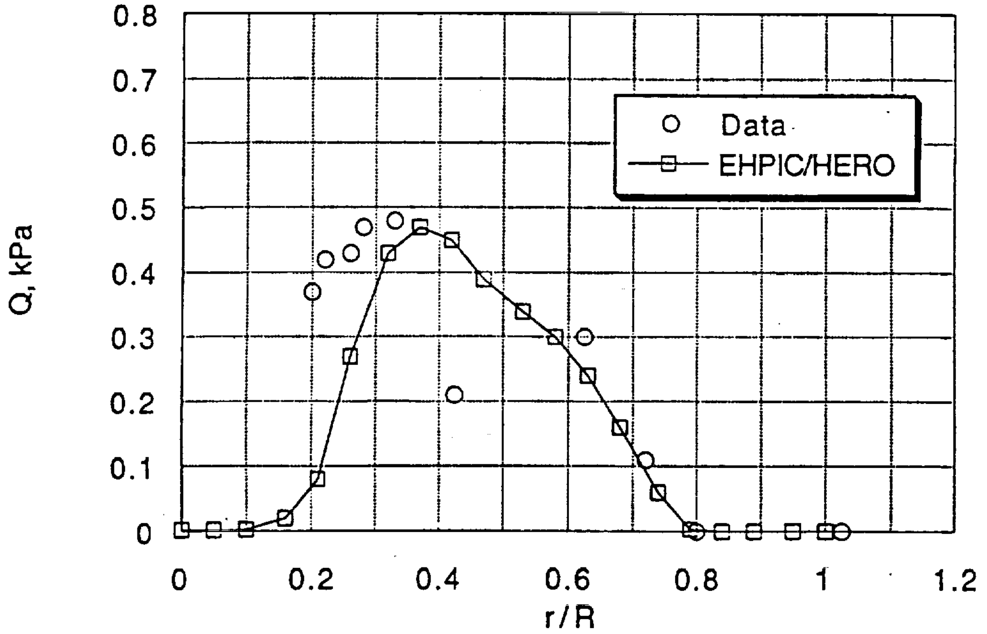

Figure 2-9. Measured and computed dynamic pressure in the wake of a V-22 rotor in hover (thrust coefficient .0059).

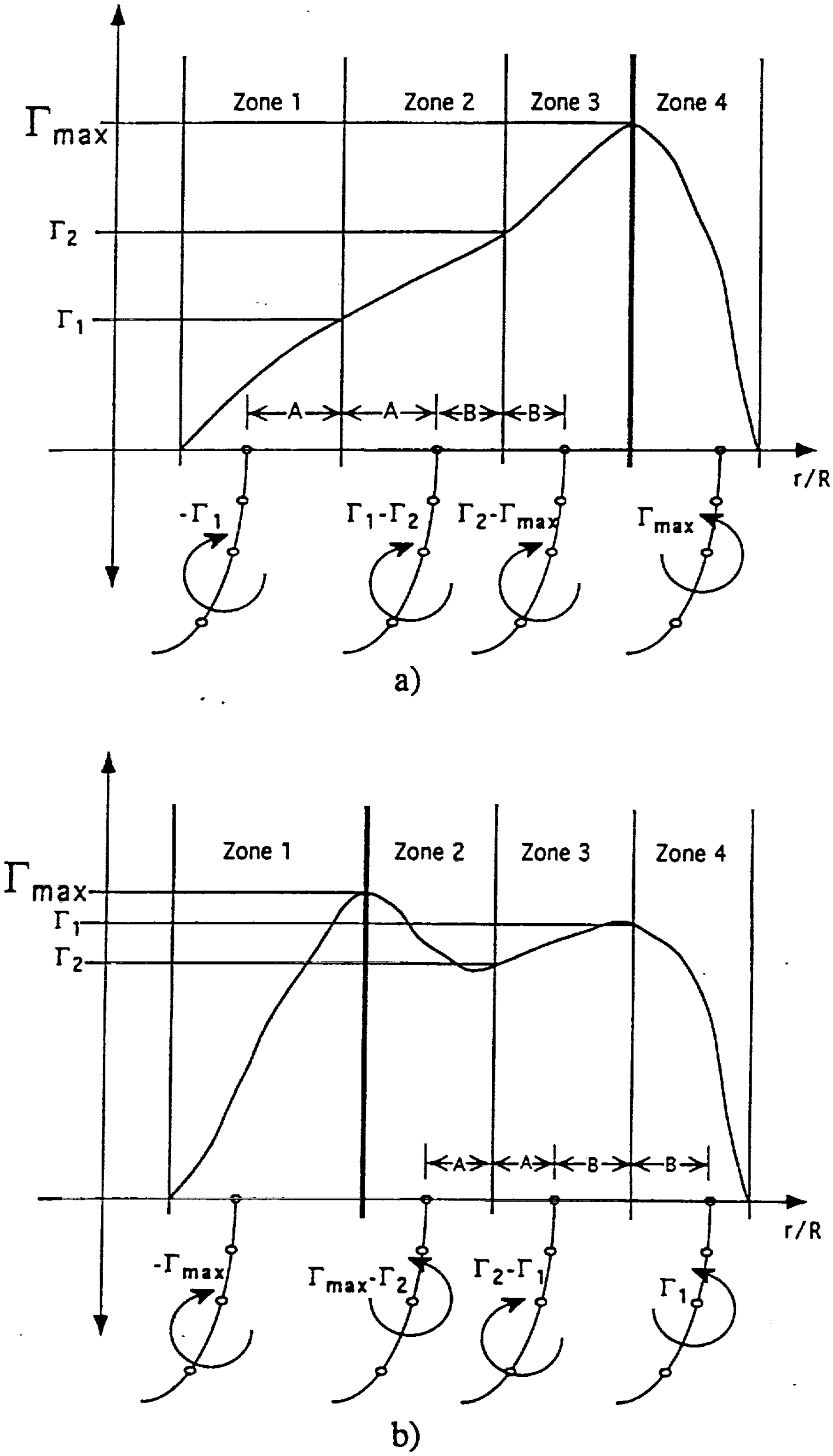

Figure 2-10. Determination of vortex filament strengths with zone boundaries placed equidistant between filament release points.

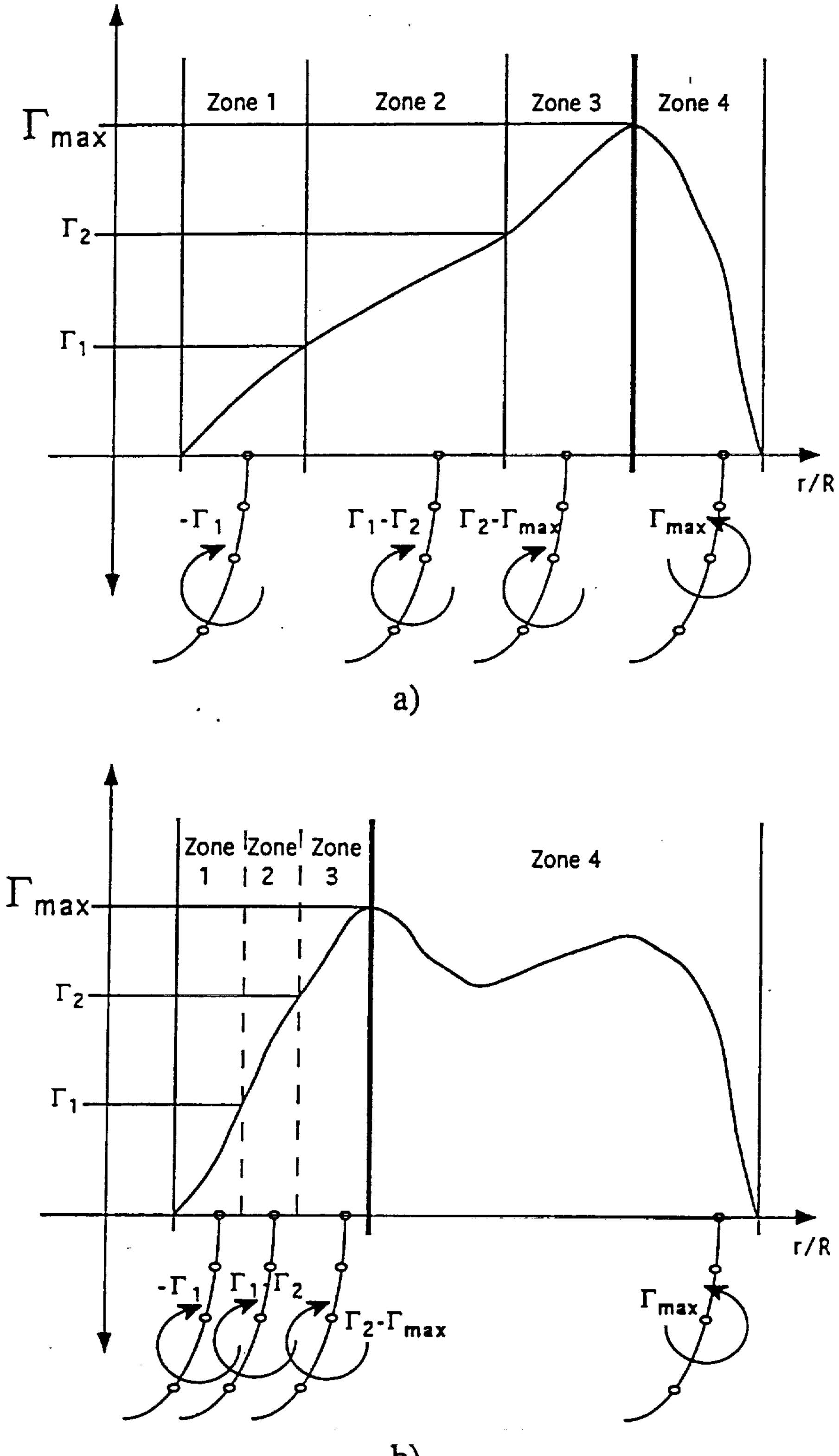

Figure 2-11. Determination of vortex filament strengths with zone boundaries scaled as fractions of peak circulation.

and is often not even necessary for this method because the filament release points will always be near the centroids of the zones they represent.

In the second approach, illustrated in Figure 2-11, the user assigns fixed values for the fraction of the peak circulation to be associated with each zone, and therefore, to be assigned to the corresponding filament. Figure 2-11 shows an example where three inboard zones (and filaments) are each assigned one third the total circulation trailed inboard of the circulation peak and one tip vortex is assigned the total outboard circulation. It is usually wise to have the filament release points move automatically to the centroid of the zones for this method because the zone boundaries are no longer tied to the filament release points. If the zones and filaments have to traverse long distances during the calculation or if they tend to bunch together (as in Figure 2-11b), this approach can suffer from convergence difficulties. However, when successful, it offers a method by which the code creates a physically consistent, evolving wake model that requires no post-calculation iterations by the user. Again, the optimization process is delayed when filament release points move, but once the calculation is near the optimum circulation distribution, the release points will cease to change and the optimization algorithm will proceed even more rapidly than the previous method because the fractional strengths of the vortex filaments are fixed from step to step. The choice of the best method often depends on the user's preference and the particular problem being studied. Additional discussion on this point is contained in Reference 12.

2.7 Investigation of Close Blade/Vortex Interaction Modeling

Hover performance is in general highly sensitive to the calculation of aerodynamic loading in the blade tip region. The tip loading is often influenced by the strong interaction with the vortex from the preceding blade. One topic of research during the present effort involved methods for more accurate and efficient treatment of this effect.

A candidate method for accurate resolution of blade-vortex interaction involves the application Analytical/Numerical Matching (ANM) (Refs. 28 and 29). This approach includes the development of a new way to handle near-field interactions between the tip vortex and the rotor blade tip of the following blade. The problem arises because the inflow velocity at the blade and the resulting blade loading, which are rapidly varying in space, must be defined accurately to assure correct performance predictions. To calculate the velocity induced at enough points on the blade to assure adequate resolution is computationally expensive in the context of a vortex lattice model, and would in general require a special high-resolution region of the lifting surface. Furthermore, this region would have to be adaptive since the position of the vortex is not known ahead of time.

ANM involves an approach similar to the method of matched asymptotic expansions. This approach uses a low resolution numerical calculation in conjunction with an analytical near-field correction. As a result, the lifting surface calculation is needed at very few points on the rotor blade, with the high-resolution near field being constructed from the local analytical solution. To implement this approach, the numerical free wake velocity field must be smoothed with an artificially fat vortex core when velocities on the rotor blade are computed. Because this smoothing produces very gradual variations in velocity, even due to near-field contributions, only relatively few control points on the blade are required to reconstruct this velocity field accurately. Note that the far-field which lies outside the fat vortex core, and which actually includes most of the free wake, is relatively smooth anyway. The fat core smoothing is used only to calculate wake effects on the rotor blade, whereas the actual core is used when calculating velocities on the wake itself, so that the vortex filament positions are still being accurately computed.

To implement this method it is necessary to develop an accurate near-field solution, ideally an analytical solution based on the local filament configuration. This solution should incorporate the position and orientation of the vortex filament passing near an idealized semi-infinite blade. Actually, two such filaments must be superimposed. One filament adds the contribution of a vortex with a physically realistic core, and the other subtracts a vortex filament with the same fat core used in the numerical calculation. The net effect in the near field is to cancel the numerical fat core effect and add the effect of the actual core size. At the same time, the far-field effect remains unchanged since the two portions of the analytical solution cancel in the far field. The vortex filament trajectories are obtained from the numerical free wake calculation modified by the analytical solution effect on the vortex.

Figure 2-12 shows how the blade-vortex interaction can be decomposed into a low resolution numerical solution and a high-resolution analytical solution. The numerical solution encompasses the full complexity of the problem, except that the fat core smoothes out the strong gradients due to the local blade-vortex interaction. The portions of the numerical solution outside the fat core radius give the correct velocity contribution on the blade. Because of the local smoothing, a relatively low density of vortex quadrilaterals can be used on the rotor blade. Basically, the fat core size must be comparable to the quadrilateral spacing to assure accuracy. Taken alone, however, this approach will give an accurate answer to the wrong problem. The local analytical solution then corrects the numerical solution to obtain the correct solution to the original problem.

Figure 2-12 also illustrates the role of the local numerical solution. This solution can be obtained from the superposition of a vortex with the actual core size and an opposite sign fat core vortex. These vortices can be modeled as straight vortices of infinite extent, oblique to the blade. The vortices should be positioned to lie tangent to the actual curved tip vortex filament at the point of closest passage beneath the blade. It does not matter that these two vortices are straight since they cancel each other in their far field, namely at distances beyond the fat core size. However, local curvature effects can be added as a refinement, if this is found to be necessary; distant curvature effects are handled by the numerical solution. In the near-field region, the opposite sign fat core analytical solution cancels the fat core numerical solution, leaving the actual core analytical solution. By appropriate choice of the fat core size relative to other problem length scales a mathematical overlap region is created, producing a uniformly valid result when all the parts of the problem are added together.

In the course of this effort, the groundwork for the ANM implementation was laid down by incorporation of a feature permitting the use of the artificial fat core for wake-on-blade interactions. The critical feature needed for full implementation, of course, is the near-field solution that characterizes the close interaction of the vortex filament with the blade surface (except for the case of direct impingement, which is beyond the scope of this study). This near-field solution is composed of two parts: a refined model of the vortex core structure and an efficient, high-resolution model of the lifting blade surface.

A vortex core model was identified for use in this context, drawn from the work of Bliss (Ref. 30). The roll-up calculation and core structure model identified in Reference 30 provides for a three-layer representation of the vortex core, involving a laminar sub-core, a potentially turbulent intermediate region, and an inviscid outer roll-up region.

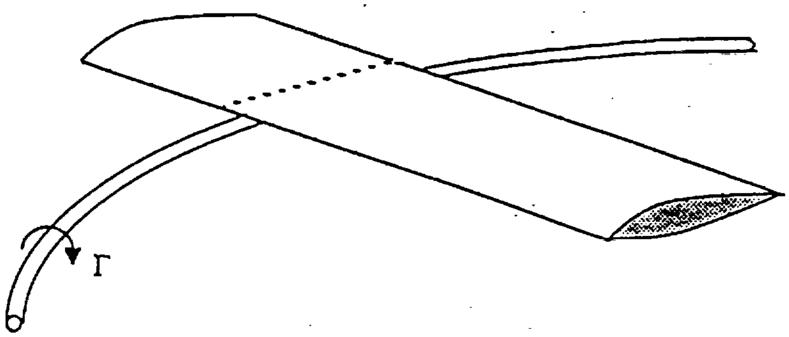

Actual Blade/Vortex Interaction

EQUALS

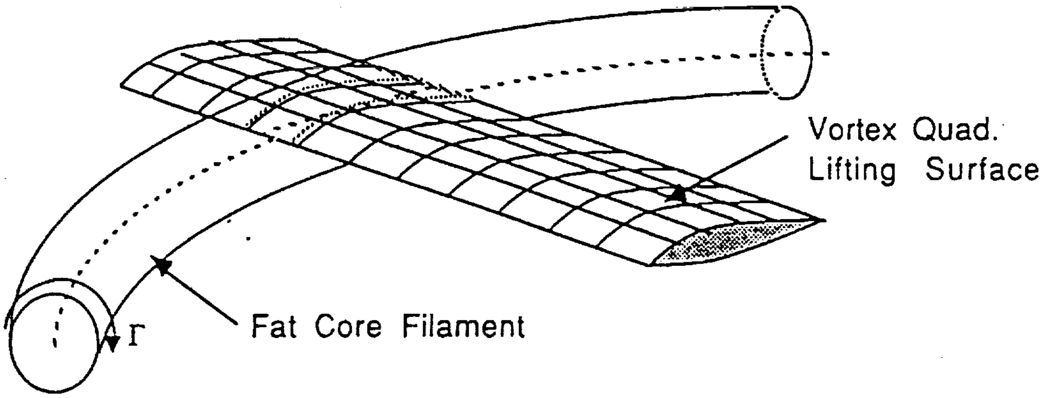

Low Resolution Fat Core Numerical Solution

PLUS

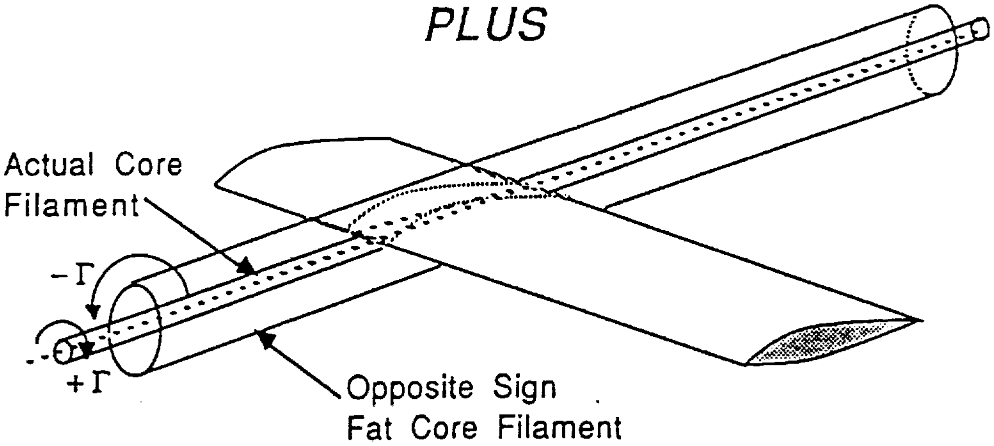

High Resolution Local Analytical Solution

Figure 2-12. Decomposition of the actual blade-vortex interaction problem into a low resolution numerical solution and a high resolution local analytical solution.

The analysis in Reference 30 also provides a way to relate some of the important integrated properties of the core to spanwise lift and drag loading on the generating blade.

Identification of an appropriate analytical lifting surface model proved more difficult. The approaches presently in the literature (e.g., Ref. 31) involve infinite-span lifting wings, while proper treatment of tip effects requires a semi-infinite span to be used. Reviews of the available literature on analytical lifting surface methods (e.g., Ref. 32) did not yield a method sufficiently flexible to be easily incorporated in a local solution. Further investigation indicated that a numerical inner solution was called for. Previous experience in adapting relatively simple numerical methods to serve as the inner solution in an ANM (or 'NNM') implementation indicated that while not ideal, high accuracy could nonetheless be achieved while still retaining a net gain in computational efficiency.

Two numerical methods were studied. The first involved the use of a high-resolution panel solution for the lifting blade in the vicinity of the tip, using an extension of the fixed wing compressible panel method described by Magnus, et. al. (Ref. 33). This method, which is implemented in the commercial panel code PANAIR, employs a mix of source and doublet singularities to capture both the thickness and lifting effects. Calculations of subsonic flow around thick, lifting wings and pressure correlations with existing airfoil section data were encouraging. However, it was found that the computational demands of the panel method inner solution, even when restricted to an isolated high-resolution region close to the tip, has so far kept this implementation from being cost effective.

Investigation into another more promising possibility began recently. Reference 34 describes an exceptionally simple (hence efficient) numerical lifting surface method originally developed for the analysis of unsteady flow over wings with control surface deflection. This approach involves distributing a set of point doublet singularities over a set of panels on the mean camber line of the lifting surface. Though this method lacks a representation of thickness, when reduced to the steady case, the point doublet method offers a very efficient method for resolving the loading near blade tips and during close vortex interactions. Also, the simplicity and efficiency of the model appears to make it a suitable candidate for implementation in the ANM framework presently in place. Work on this topic is ongoing, and this refined tip model is a candidate for implementation in future versions of EHPIC/HERO.

3. HIGH RESOLUTION ROTOR WAKE COMPUTATIONS

The work described in this section was motivated by the high sensitivity of rotor performance to the wake structure trailing from the blade tip. As discussed in Reference 9, EHPIC calculations typically involve using a single vortex to model the wake of the tip region. Both experiment and experience with numerical performance correlations to date support the use of this approach in many physically important cases. However, it is not a fully general representation. This section describes the formulation of a high-resolution numerical model of the blade wake designed to be more generally applicable and, in particular, to offer greater flexibility in modeling the wake trailed from the blade tip region.

3.1 Rotor Tip Vortex Roll-Up

Recently there has been much interest in the rotorcraft community concerning the flow near the tip of a helicopter rotor blade; much of this has been inspired by the possibilities of improved aerodynamic performance resulting from advanced blade tip design, e.g., swept-tapered planforms such as the S-76, the UH-60, and the BERP tip. The advent of tiltrotor configurations with highly twisted blades that depart significantly from conventional design also calls for better resolution of the dominant physical phenomena which are present in the rotor wake. Under typical operating conditions, these rotor blades all tend to exhibit bound circulation distributions that depart from the pattern characteristic to conventional untapered planforms with moderate twist, i.e., an abrupt drop in bound circulation near the tip (Fig. 3-1). The presence of gradual tip load roll-off (e.g., Fig. 3-2) may lead to incomplete tip vortex roll-up by the time of the first blade encounter. This introduces a requirement for an analysis that explicitly computes tip vortex roll-up.

General methods for the analysis of tip vortex formation in rotorcraft are not available, though experimental work has yielded significant insights into the structure of tip vortices. References 35 and 36, among others, have carried out measurements of swirl and axial velocities in rotor vortex cores with the objective of characterizing the core structure. This work has also provided empirical support for models of the flow field inside the vortex core used in previous calculations . Indirect evidence of the behavior of rotor blade wakes can also be obtained from smoke and shadowgraph visualizations carried out over the last twenty years (Refs. 1, 2 and 37). These studies have confirmed the basic wake structure originally observed by Gray in 1956 (Ref. 38), i.e., a single strong tip vortex accompanied by a more diffuse inboard wake sheet. The formation of this tip vortex is caused by the rapid roll-up of the wake immediately downstream of the rotor tip, which in turn is driven by the large gradient of bound circulation near the tip. The presence of such loading distributions on conventional planforms is a well-established fact, but significant exceptions to this pattern exist on tiltrotor blades as noted above. At present, there exists very little measured spanwise load distribution data on tilt rotors (Ref. 39 is one of the few examples), but what does exist - coupled with available computations like that shown in Figure 3-2 - indicates that load distributions have very broad peaks located well inboard of the tip and characterized by gradual load roll-off outboard.

Such bound circulation distributions will inevitably lead to more gradual roll-up of the trailing vorticity, with the likelihood that not all of the maximum bound circulation will be found in a concentrated tip vortex. Shadowgraph visualizations of model tiltrotor wakes have indicated the presence of distinct tip vortices (Ref. 37), though in the absence of simultaneous measurements of the circulation of these vortices, it is difficult to reach a

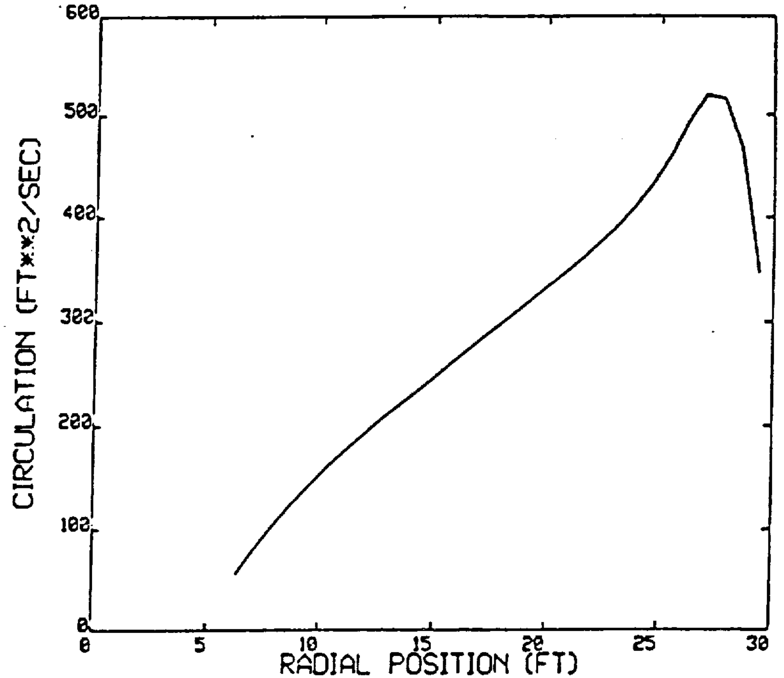

Figure 3-1. Typical bound circulation distribution on a representative low-twist rotor in hover (CH-47B at thrust coefficient .0068).

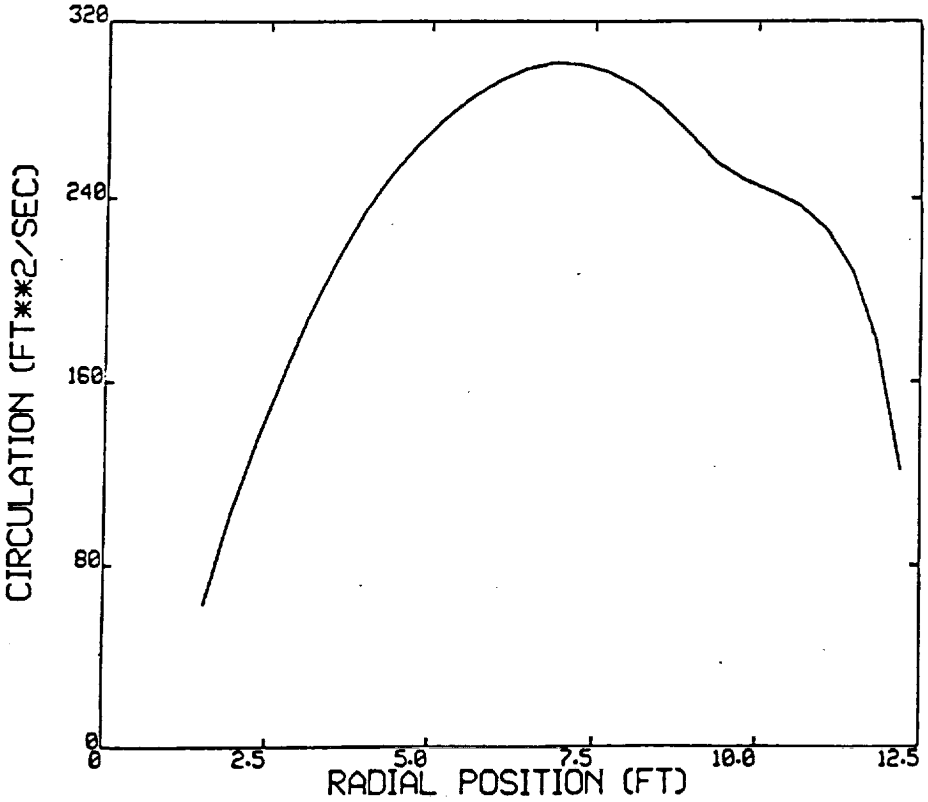

Figure 3-2. Computed bound circulation on a high-thrust tilt rotor blade (XV-15/ATB of thrust coefficient .0118).

conclusion as to the fraction of the peak bound circulation they represent. Scaling calculations that borrow from work on fixed wing wake roll-up (e.g., Ref. 40) can be used to estimate the degree of concentration of the trailed vorticity at the time of first blade encounter. Figure 3-3 shows a schematic of the bound circulation on a fixed wing along with the trailing wake distribution, as well as the major governing equations of the Betz/Donaldson vortex roll-up model described in Reference 40. The model yields an estimate of the core radius and circulation strength of the tip vortex of a wing as a function of the downstream distance, given the peak value of the bound circulation as well as its functional distribution.

Figure 3-4 shows the evolution of the core properties using this model as a function of nondimensional downstream distance for elliptic, parabolic, and linear bound circulation distributions. The downstream distance on the horizontal axis is nondimensionalized as a function of aspect ratio AR, the wing lift coefficient C_L, and distance from the location of the peak circulation out to the centroid of the trailing wake. This analysis is not directly applicable to rotary wing tip vortex roll-up because of the absence of the symmetry of the trailing wake about the peak circulation as well as because of the effects of rotation. It was nonetheless judged to provide a useful guide for scaling tip vortex core sizes and for estimating the degree of roll-up that occurs in typical rotary wing calculations.

To investigate this point, assume that the Γ_0 specified in these figures is treated as the peak bound circulation near the tip and that the rotor blade tip wake rolls up into a single vortex. If the further suppositions are made that the distance from the position of the peak circulation to the blade tip can be equated to the wing semispan in the analysis of Reference 40 and that the downstream distance is roughly equivalent to the curved path described by the circular wake, then an estimate of the scale of the vortex core size and circulation as a function of azimuth angle downstream can be computed. Denoting the nondimensional distance from the peak circulation to the blade tip as $k_R R$ and normalizing the peak circulation by ΩR^2 yields a measure of the distance downstream of the blade for use in the plot shown in Figure 3-4:

$$D = \frac{1}{2}\frac{\bar{\Gamma}_{max}}{k_R^2}\psi \tag{3-1}$$

(Here, ψ is the azimuth angle downstream of the generating blade in radians). This formula applies for both linear and parabolic distributions and can be used as a rough guide to the point at which the horizontal axis of Figure 3-4 should be entered to estimate the fraction of roll-up that has taken place. For example, on an XV-15 rotor, a typical value for $\bar{\Gamma}_{max}$ is .03, and the location of most interest is the first blade encounter which occurs at $\psi = 2\pi/3$. Assuming that the tip roll-off is parabolic and that $k_R = .05$ (i.e., the peak circulation is five percent inboard of the tip), D is 12.56 at the first blade encounter; the plot of Figure 3-4 indicates that essentially all of the trailing vorticity will have rolled up into the vortex by this point, since the fraction Γ/Γ_0 plateaus at 1.0 at values of D between 3 and 6. However, for typical XV-15 cases k_R is at least 0.15, in which case D would be reduced to 1.4. As indicated in Figure 3-4, for a parabolic roll-off the roll-up fraction at first blade encounter would then be about 0.8 for parabolic tip loading and about 0.5 for linear loading. Realistic loading is probably closer to the former rather than the latter, but in either case it seems likely that the tip vortex structure that the following blade encounters will not be dominated by a single strong,

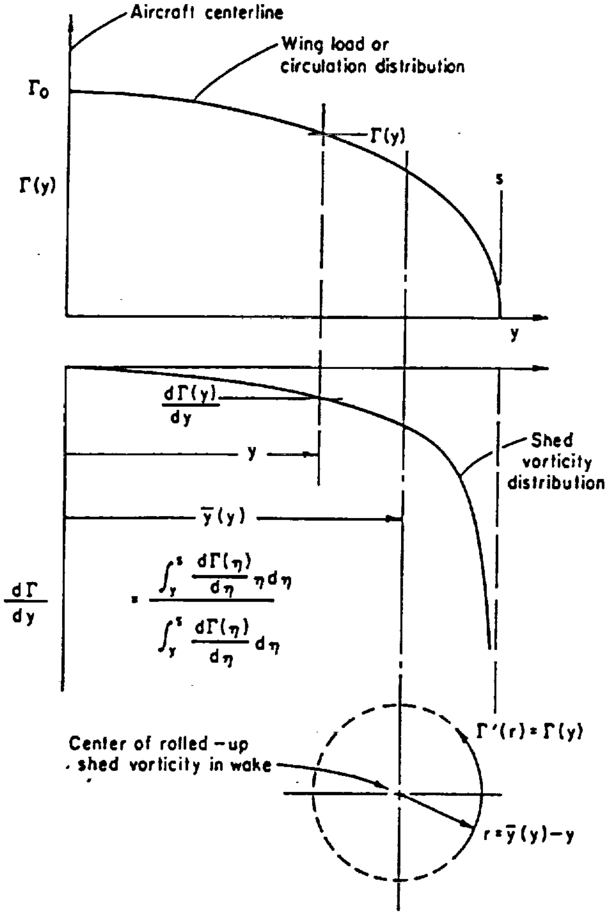

Figure 3-3. Schematic of the roll-up of bound circulation from wing with bound circulation distribution $\Gamma(y)$ on the semispan (Ref. 40).

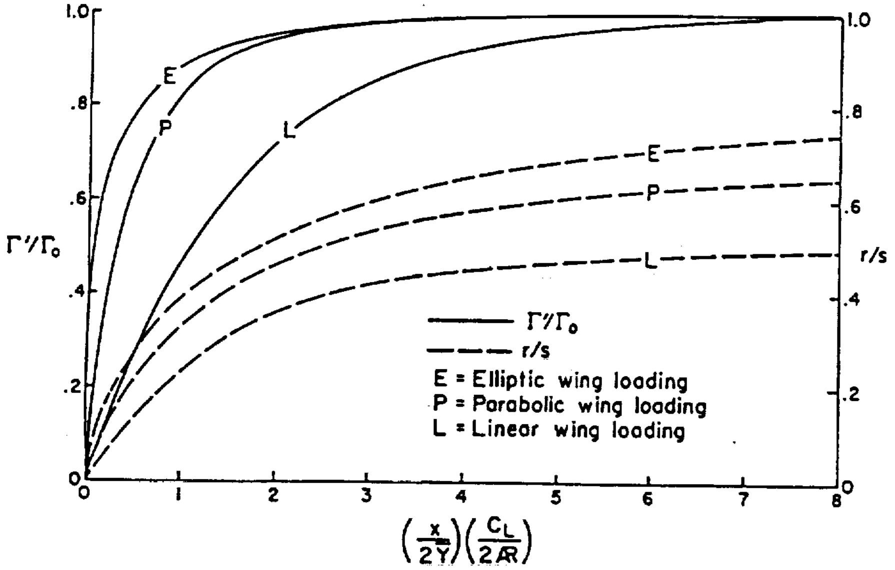

Figure 3-4. Estimated trailing vortex circulation strength and radius as a function of downstream distance (Ref. 40).

fully rolled-up tip vortex. Most of the vorticity will have rolled up, but a substantial fraction will remain outside the core, leaving a partially rolled-up filament whose strength is substantially below the full value of the bound circulation peak.

3.2 Structure of Vortex Roll-Up Calculations

In principle, a variety of options exist for obtaining improved computational resolution of the rolling-up vortex wakes. Recent work in this area has included attempts to apply both Euler and Navier-Stokes solvers to the computation of wingtip roll-up (Refs. 41 and 42). To date, the interrelated problems of high numerical diffusion and large computation time have precluded practical application of such tools to the rotary wing problem. In the context of EHPIC/HERO, it was judged most appropriate to develop a refinement of the present Lagrangian free wake model using vortex filaments.

3.2.1 Initial resolution of rolling-up near wake

In the EHPIC code, an initial guess of the vortex wake geometry is successively refined by an iterative relaxation approach based on the influence coefficient method described in Section 2. Formally, this iterative relaxation can be considered a systematic method for reducing the error in the position of the initial guess relative to the converged solution. Within the iteration, various 'error modes' associated with the initial solution are successively damped and the solution is marched toward the converged state. Typically, several relatively widely spaced filaments are used to represent the inboard vortex sheet and a single vortex filament is used to represent the strong rolled-up tip vortex. Early attempts to use a high-resolution treatment of the vortical flow near the tip region in EHPIC encountered numerical difficulties (Ref. 9). This was a direct result of the strong amplifications of the high frequency components of the error modes associated with the initial guess (which may be far from the converged wake geometry) and the highly nonlinear variations in the wake-induced velocity field.

In the present effort, a new computational technique was developed that builds on the existing wake model to permit a high-resolution treatment of the flow downstream of the blade tip. The new method is based on the use of a sequence of coarse-to-fine Lagrangian grids and is developed in the spirit of a multi-grid method which is widely used in finite-difference and finite-element calculations (Reference 43). The key idea behind the present technique is the observation that at the outset of the calculation where the approximate discrete solution deviates substantially from the actual 'continuous' solution (i.e., the converged wake geometry), the error norm of the guessed initial solution is large. If this solution is projected onto a fine grid using small elements, the high frequency error mode would amplify rapidly because of the non-linearity of the problem (the iterative influence coefficient method is based on a linear Newton's method and neglects the non-linear terms in the problem). However, if a coarse grid (i.e., a small number of vortex filaments each discretized using a few BCVE elements with large arc-length) is used, the fast growing high frequency error components are not present. Thus, the error norm can be represented as a Fourier series comprising of various Fourier modes but with the highest frequency limited by that resolvable on the given grid.

The slow growing low frequency modes are damped in the iterative relaxation process and the calculation converges to an approximate coarse grid discrete solution, which is presumably 'closer' to the actual continuous solution than the initial guess. Thus, the first approximation to the desired high-resolution solution is thus the single-tip-filament solution obtained in previous EHPIC calculations. The error norm associated with the coarse discrete single-filament solution is correspondingly lower than the initial guess. This solution can be projected onto a fine grid, and because the amplitude of the resulting high frequency error mode is much lower, the non-linearity of the problem is not significant (any non-linear term is small) and the discrete solution can be marched toward a converged state on the finer grid. The fine grid discrete solution will represent a better approximation of the actual continuous solution compared to the coarse grid representation.

Based on the this general numerical strategy, we have incorporated an optional algorithm for the high-resolution calculation of flow near a blade tip into the EHPIC/HERO code. In this algorithm, a baseline calculation using a coarse-resolution wake representation comprised of a single tip vortex filament and several inboard wake filaments is carried out. A representative configuration of the wake is given in Figure 3-5. This configuration is first iterated toward a converged state with a single strong tip vortex as in the EHPIC code. After the initial convergence, multiple copies (depending on the desired level of resolution at the tip) of the spatial geometry of the tip filament are made and attached to the trailing edge of the blade at stations close to but inboard of the tip. An example of this is shown in Figure 3-6, where a converged tip filament has been mapped inboard, resulting in a two-filament representation of the trailing wake at the tip. Once this initial configuration is set up, the relaxation solution is recommenced and this solution is again iterated toward a high-resolution converged state. Usually, convergence is achieved within several steps because the error norm of the guessed solution in the fine-grid calculation is much lower than would have been the case had two such closely placed filaments been started "from scratch".

The two-filament case shown in Figure 3-6 is only one example of the possible application of this technique. To date, calculations with as many as five trailers from the tip vortex roll-up zone have been used. Additional refinement is possible within this scheme, however computational constraints still limit full resolution of the roll-up process, as will be discussed at the end of this section.

3.2.2 Amalgamation of multiple tip vortex filaments

In the context of the present scheme, the vortex sheet trailing from the tip, discretized into a relatively diffuse set of vortex filaments, typically rolls up into a tighter bundle with the filaments effectively collapsing into a single vortex tube far downstream of the generating blade. As discussed in Section 3.1, the speed at which this proceeds (i.e., the distance downstream required for the roll-up to be completed) scales with the size of the tip vortex zone and the steepness of the bound circulation gradient. In general, complete resolution of this process is not feasible, nor is it necessary in most practical calculations of interest in the current context. A significant question then arises as to how to compute the roll-up in a way that leads to robust convergence properties without compromising reasonable physical accuracy. In terms of quantities of interest, such as surface pressure distribution on the blade immediately following the generating blade, the resolution of the rolled-up filaments once they pass by is inconsequential and the multiple filaments can be replaced by a single filament while conserving circulation. This is also desirable because it reduces the computation time without significantly compromising numerical accuracy.

In EHPIC/HERO, then, the second stage of the high-resolution tip calculation involves a merging algorithm that amalgamates the vortex trailers and replaces the portion of the multiple tip filaments which are beyond the first blade encounter by a single filament. In this part of the calculation, a cross-flow analogy is used to carry out the final stages of the amalgamation. The general three-dimensional roll-up problem is steady in the rotating reference frame, and thus can be approximated as a two-

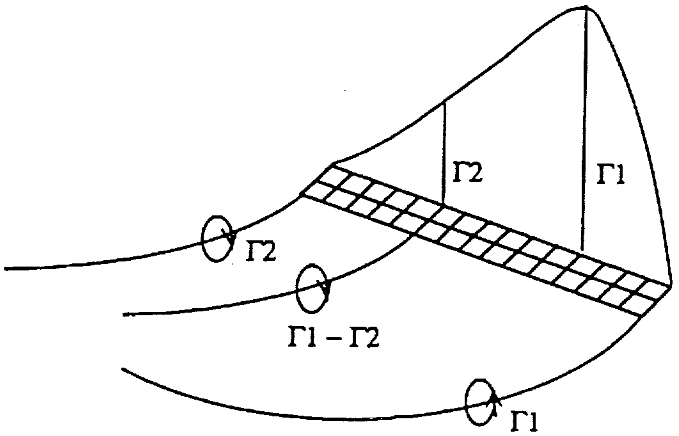

Figure 3-5. Representative wake configuration of a baseline calculation with a single tip filament.

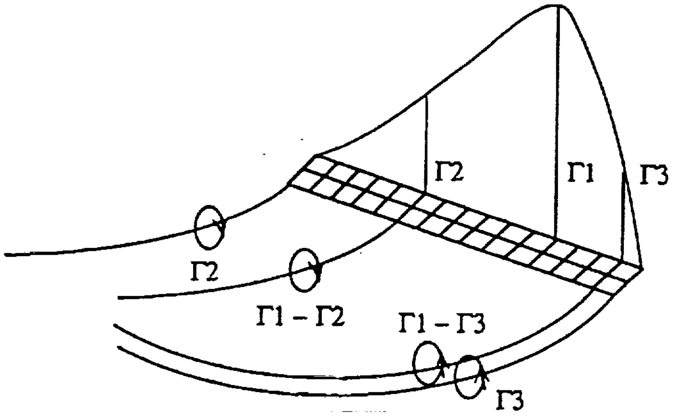

Figure 3-6. Representative wake configuration of a fine grid calculation starting from a converged baseline calculation; tip filament is mapped inboard to give a multiple filament representation of the rolled-up wake.

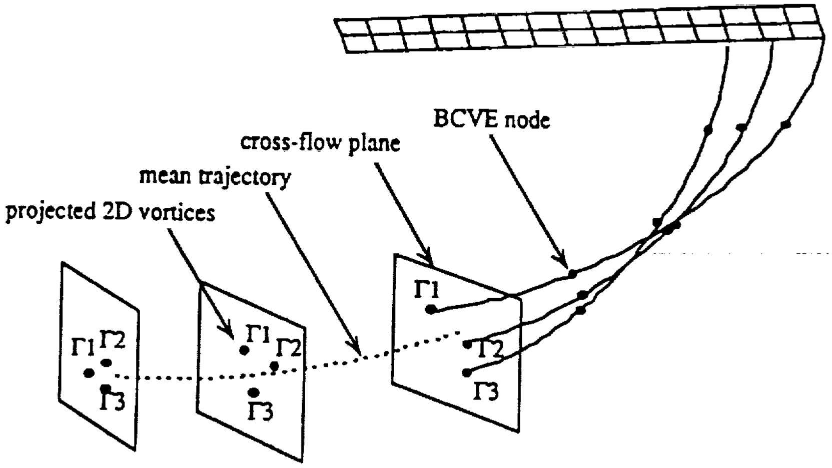

Figure 3-7. Schematic illustrating the merging of multiple tip filaments computed using a two-dimensional crossflow analogy.

dimensional unsteady problem, with distance along the curvilinear trajectory of the centroid of the vortex bundle being the 'time-like' variable. The use of a cross-flow analogy in three-dimensional steady flow calculations is not new and has been extensively exploited in the calculations of separated flow over simple bodies of revolution (e.g., missiles) at high angle of attack (Ref. 44).

This amalgamation procedure requires that the user select an azimuthal station for the beginning of the merging process. This station should be well downstream of both the generating blade tip and the first blade encounter; a location halfway between the first and second blade encounters is typically appropriate. Its exact location is computed as the centroid of the multiple free filaments in the initial roll-up at this azimuthal station. A trajectory starting from this point and consisting of stations along each of the multiple filaments is then computed, with the centroid of the bundle being computed at each azimuthal station. A cross-flow plane is then created at each station with its unit normal vector computed from the mean tangential vectors of the multiple tip filaments at the given station (see Figure 3-7). The multiple tip filaments are then projected onto the plane and represented as two-dimensional vortices.

The time evolution of these quasi-2D vortices is computed in the cross-flow plane by integrating the two-dimensional vorticity transport equation. A small time step size is chosen such that several steps are executed between a given pair of stations, and a fourth-order Runge-Kutta integration scheme is used to ensure high numerical accuracy. At each station, the computed locations of the two-dimensional vortices give the cross-plane location of the nodes of the vortex filaments. A separation criterion is specified in terms of a fraction of the core size of the vortices. If the separation distance between any pair of two-dimensional vortices at a given station is less than the separation criterion, the two vortices are lumped into a single vortex located at their mutual centroid. The corresponding pair of vortex filaments are also merged. Typically, merging of all the vortices is completed within five to ten azimuthal stations.

3.3 Sample Calculation

The high-resolution tip vortex calculation, coupled with the two-dimensional time analogy merging algorithm, have been successfully implemented in EHPIC/HERO and several test calculations have been carried out. The focus of interest here is on rotors whose bound circulation distributions exhibit relatively slow roll-up of the tip vortex. Test computations have been carried out on an S-76A main rotor as well as on various tiltrotor configurations. Selected tiltrotor results are presented here since they best illustrate the high-resolution model at work and are in fact potentially one of the most important applications for this capability.

As stated above, computed results on tiltrotor blades often show low bound circulation gradients near the tip, indicating that the tip vortex may be only partially rolled up by the time it reaches the following blade. Though a concentrated tip vortex almost always is present at the first blade encounter, the strength of this vortex tube may well be substantially less than the peak bound circulation, and the distribution of vorticity in the tube may be poorly represented by a single vortex. To investigate this possibility, successively more refined multiple vortex runs were undertaken for the case of an XV-15 main rotor. Test data on the hover performance of this configuration is available in Reference 45. The blade is 3.81 m (12.5 ft.) in radius, with a constant chord of 0.354m (1.16 ft.). The tip speed is 234 m/s (769 fps), and the blade has roughly 37 degrees of washout, distributed in a nonlinear fashion across the span. Detailed performance correlation for this rotor is discussed in Section 6.

A baseline calculation was run with the root pitch at 42.5 deg., initially employing a very coarse wake with four free filaments trailing from the span: three distributed evenly inboard, with a single vortex trailing from the tip (Fig. 3-8). This coarse initial condition was chosen to dramatize the effect of the refinement afforded by the multiple filament roll-up calculation. This very simplified wake model yields a predicted thrust coefficient of 0.0120 and a Figure of Merit of 0.741, substantially lower than the value of roughly 0.78 that is estimated from the measured performance data in Reference 45. Note that to facilitate this demonstration, the tip filament was trailed from the tip of the blade, one quadrilateral outboard of the centroid of the tip circulation zone. This partially accounts for the under prediction of the Figure of Merit.

To improve the resolution of the tip wake, three additional filaments were added to the high-resolution zone, which extended 75 deg. beyond the first blade encounter. Top and oblique views of the geometry of the refined wake are shown in Figures 3-9 and 3-10, indicating the trajectories of the filaments in the high-resolution region. Each filament uses 14 free elements subtending 10 degrees of arc in this region. An estimate based on a computation of D in Equation 3-1 suggests that the roll-up should be complete in roughly 150 degrees of arc, so elements of this arc length are sufficient to resolve at least the full rotation of the tip vortex bundle. The prescribed amalgamation zone applies the quasi-2D flow described in the previous section over 70 degrees of arc, leading to the smooth merging seen in Figure 3-9.

The bunching of the three outer vortices, representing 87% of the peak circulation strength, is evident in the figure, and allows a more realistic representation of the flow field in the vicinity of the blade. The gross features of the roll-up process are captured, and the improved resolution is reflected in the improvement in the predicted performance; a Figure of Merit of 0.772 at a thrust coefficient of 0.0121 is predicted, close enough to the measured performance curve to be within the scatter of the data. Figure 3-11 shows a comparison of the predicted thrust distribution along the span, indicating the sharper peak that is associated with the implementation of the high-resolution wake model.

As indicated by these calculations, the high-resolution multiple vortex model presently in place has a substantial capability to obtain refined computations of the wake trailing from the tip region. However, certain computational limitations still restrict the applicability of the present model. The trailing wake should in principle be represented by a continuum of trailing filaments rather than by the relatively coarse discretization used here. Adding filaments will drive up the CPU time, but it is more the issue of robustness that is of most concern. At present, selecting the vortex core radius to be 1.0 to 2.0 times the distance to adjacent filaments in the high-resolution region produces generally consistent, well-behaved results. However, additional spanwise refinement brings a requirement to introduce still smaller azimuthal segments to properly resolve the wake-on-wake interactions. This leads in general to greater difficulty with convergence, though this situation can be aided substantially if the limitations on wake-on-wake velocity discussed in Reference 12 (see the input parameter ICON) are invoked. For highly refined wakes, though, the overlapping of filament cores becomes inadequate, and a higher order model should be used, possibly including vortex sheet elements.

In addition, this type of inviscid roll-up model is appropriate only to resolve the larger scales of the vortex formation process. Refinement of the order of less than a few percent of core radius requires implementation of a direct model of viscous and turbulent flow within the core, as discussed in Section 2.7. To date, adding this level of refinement has not proved cost-effective for the performance optimization applications explored here.

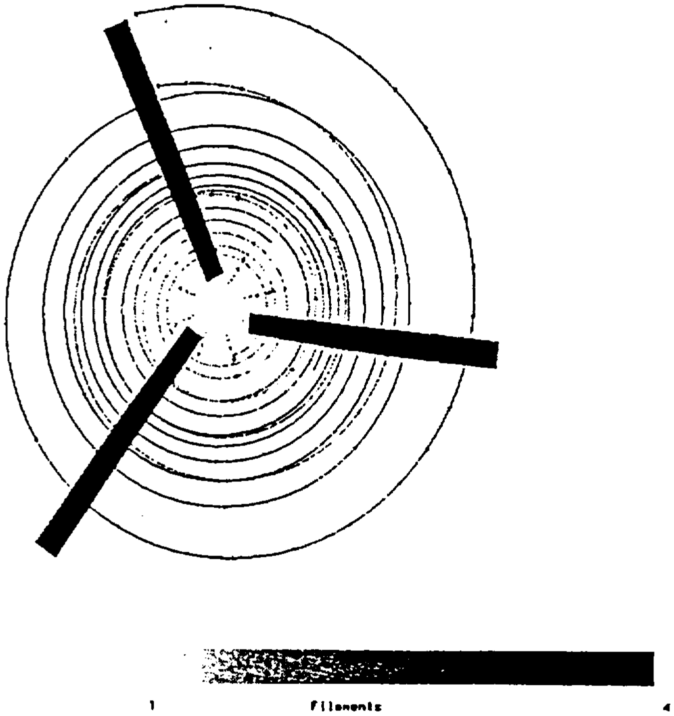

Figure 3-8. Top view of the initial coarse-resolution solution for the XV-15 rotor (wake of one blade only shown).

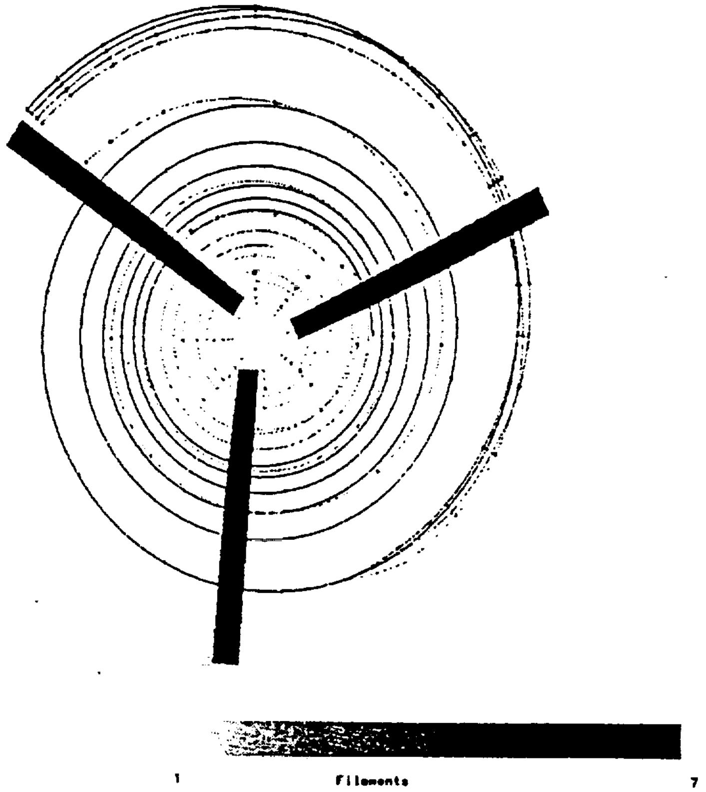

Figure 3-9. Top view of the converged high-resolution wake geometry solution for the XV-15: four filaments used in the high-resolution tip zone (wake of one blade only shown).

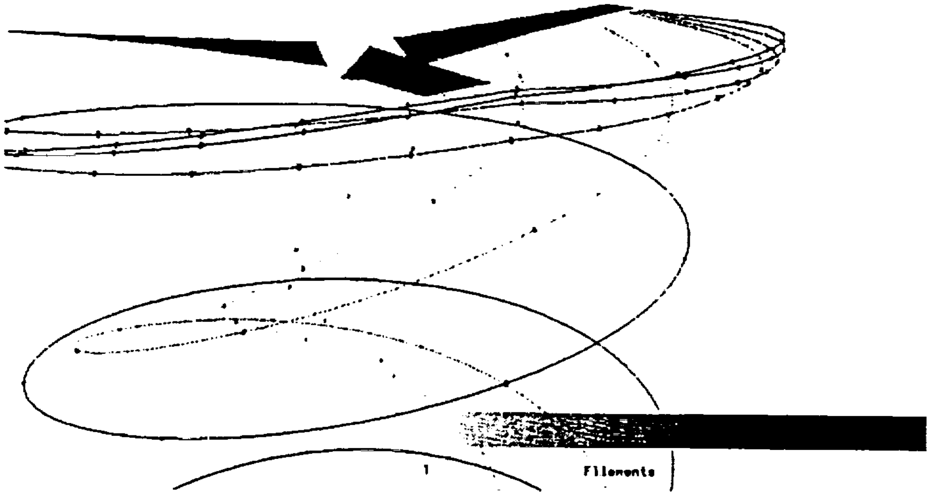

Figure 3-10. Side/oblique view of the converged high-resolution solution for the XV-15 rotor (wake of one blade only shown).

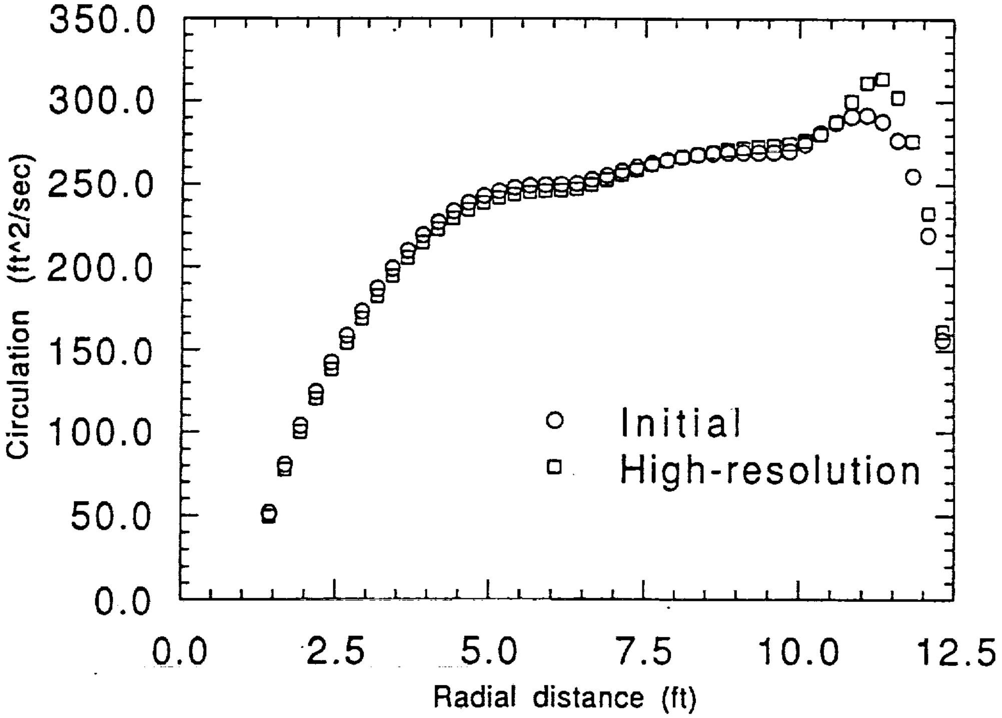

Figure 3-11. Bound circulation distribution with initial coarse-resolution and final high-resolution wake models for the XV-15 case.

3.4 Side-edge Separated Flow Modeling

In the present effort, an approximate method for computing the effect of flow separation on the side-edge of a blade has been developed. In general, this is a viscous phenomenon whose details cannot be computed with the present inviscid model. The motivation for this particular feature of the model was to attempt to develop a simple model that quantifies the likely effect of the 'lift-off' of tip vortices from the blade edge, and to permit the user to assess its importance in particular cases.

The present method represents an extension of the two-dimensional cross-flow calculation developed for the merging of multiple vortex filaments, as described in the previous section, to the edge flow problem. In this calculation, the cross-flow analogy is applied to the treatment of the flow along the side-edge of the blade, and the three-dimensional steady separated flow is computed as a two-dimensional unsteady separated flow problem. In this case, cross-flow planes are computed which are in-plane with the unit normal vector $\underline{n}$ of the blade surface and the radial direction of the blade (Fig. 3-12). The plane is placed along the edge of the blade and the flow velocity normal to the blade, resulting from the angle of attack of the blade airfoil, is projected onto the plane. This results in a two-dimensional unsteady problem involving a flow past a flat plate normal to the flow direction. Time integration of this two-dimensional problem gives the location of the separated vortex along the side edge of the blade. At $t = c/U_\infty$, where c is the chord length of the blade and U_∞ is the projected free-stream velocity in the two-dimensional case, the two-dimensional calculation gives the location of the separated vortex near the trailing edge of the blade, which is used as an attachment point for the tip vortex in the three-dimensional case.

Unsteady separated flow past a normal flat plate is a classical problem that has been extensively studied (Refs. 46 - 48). The work of Pullin (Ref. 48) is of particular interest and can be directly applied to the present calculation. In his model, the self-similar rolled-up vortex sheet emanating from an impulsively started flat plate is computed. Based on his self-similar results, it is straightforward to derive the following relation between the location of the separated vortex and the total circulation in the vortex and time:

$$Z = \left\{ \frac{3}{4} \frac{\Gamma}{2.64} t \right\}^{1/2} \qquad (3\text{-}2)$$

where Z is the height of the vortex above the blade, Γ is the circulation of the vortex and t is time. This relation suggests that given a vortex with known location and circulation, the locations of all other vortices with different circulations can be estimated based on this similarity.

This has been tested by computing the separated vortex of a two-dimensional normal flat plate. Two separate flow configurations were examined, which resulted in two vortices of different net circulations. It was found, however, when the coordinates are properly scaled, the two vortices appear to be similar, with nearly identical locations. This is shown in Figure 3-13a and 3-13b and the similarity argument is well proven. This similarity relation considerably simplifies the implementation of a simple side-edge separation model in EHPIC/HERO since we need only to compute the location of the vortex once (at the first step for a given blade pitch angle); at all subsequent iterations, the location is obtained by using the scaling in Equation 3-2. The effect of this model

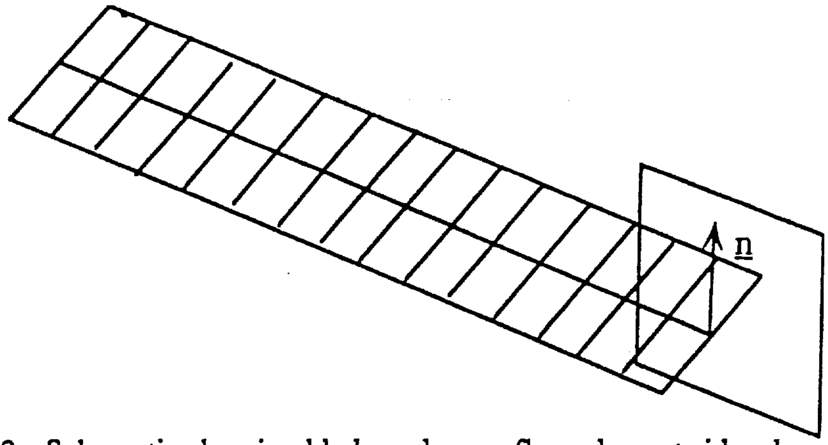

Figure 3-12. Schematic showing blade and cross flow plane at side edge of blade.

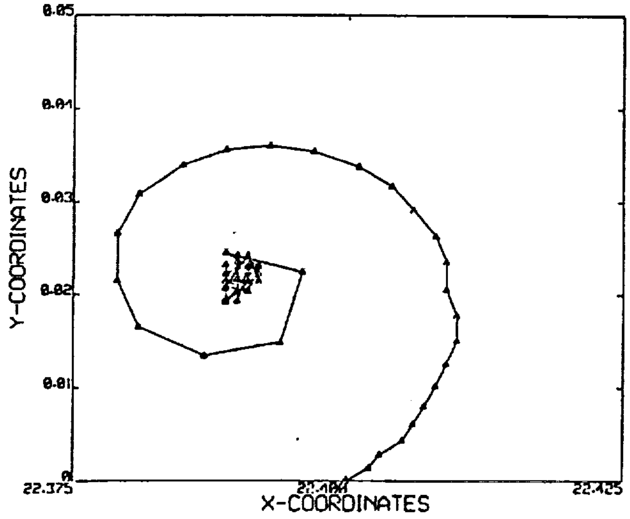

a) Normalized circulation = 1.0

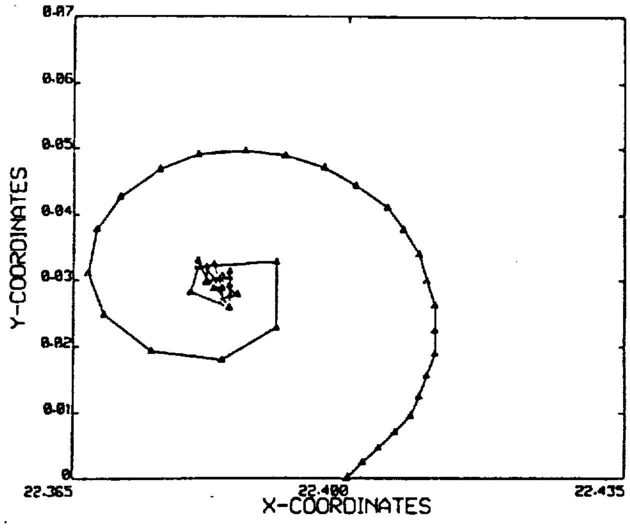

b) Normalized circulation = 2.0

Figure 3-13. Demonstration calculation of a self-similar 2D unsteady vortex solution, modeling the flow development on a blade edge. Calculations are at equal times.

when invoked is to alter the vertical release point of the tip filament. The inputs required for this model are described in Reference 12.

4. FORMULATION OF THE ROTOR BLADE STRUCTURAL MODEL

The structural properties of the helicopter blade are in many cases important to the evaluation of the performance of a helicopter in forward flight. Thus, one of the major efforts within the development of the EHPIC/HERO code has been to incorporate a realistic finite element (F.E.) representation of the blade. This section discusses the formulation of the structural model together with its capabilities and limitations and the manner in which it is coupled to the aerodynamic wake model. Further description of the inputs required for this portion of the analysis are given in Reference 12.

4.1 Finite Element Structural Model of the Helicopter Blade

The particular finite element (F.E.) model used here to represent the helicopter blade accounts for extension, twist and transverse bending displacements. To accurately simulate these deformations, the blade is discretized into a number of beam finite elements each having a total of 14 degrees of freedom (d.o.f.). Stiffness properties for each element are computed from the cross-section geometry and material properties supplied by the user. Similarly, the blade mass distribution is used to both define the nodal forces due to blade rotation and also the contributions of blade rotation inertia forces to the stiffness matrices (geometric stiffening). The resulting elemental stiffness matrices are then assembled and any constrained d.o.f. eliminated to finally yield the global stiffness matrix for the complete blade structure. The approach taken is similar to previous implementations of F.E. methods for rotorcraft applications, such as Reference 49.

The transfer of information between the structural and the aerodynamic models is achieved by requiring force equilibrium and by specifying the kinematic relations that define the blade geometry in terms of the undeformed blade shape and the vector of nodal deflections. In essence, nodal forces, $\underset{\sim}{f}$, are computed from the distributed aerodynamic forces and the blade rotation. The steady state deflections are determined by solving the linear system of equations, $[K]\underset{\sim}{s}=\underset{\sim}{f}$. Finally, the deformation vector is used in conjunction with the undeformed blade geometry to furnish the deformed blade geometry. The geometry update perturbs the flow-field which in turn alters the nodal forces. Thus an iterative process is invoked until convergence is attained. This iterative process is done in parallel with the wake relaxation calculations so that the entire process essentially converges to the final deformed blade and associated flow-field. The remainder of this section explains in greater detail the derivation of the structural model and the manner in which it is coupled to the wake model.

4.1.1 Assumptions

The assumptions inherent in the blade model and geometry are stated below:

- The blade displacements are of sufficiently small magnitude that:
  - linear constitutive relations between stress and strain are applicable,
  - the transformation matrix relating the local axes of each element may be regarded as constant and equal to the corresponding matrix in the undeformed state,

  - rotations due to deformation are assumed to commute, and,
  - the twist, bending and extension deformations may be linearly superimposed.

- The blade material is assumed isotropic and the stress-strain relation obeys Hooke's law.
- The elastic axis for each element is defined. The elastic axes of any two adjacent elements coincide at their mutual joining section (see Fig. 4-1). In other words, the elastic axis is continuous along the blade. This is necessary to correctly define the assembly of the individual blade F.E. s.
- The principal axes of the cross-section for each element are assumed to be perpendicular to the elastic axis of that element. This implies that if there are sweep and anhedral changes between consecutive elements then their principal axes will not coincide at their mutual section. The degree of approximation introduced into the bending calculation will increase with the amount of sweep and anhedral change between adjacent elements. It will also decrease with slenderness of the element since the discrepancies resulting from non-alignment of the principal axes occur locally in the neighborhood of the joining section.

Note that the last two assumptions are mainly due to the fact that warping effects are modeled in the analysis. One of the chief advantages of the finite element method is its versatility in the assembly of the constituent elements. For simple elements, e.g., pure beam elements and bar elements, one is free to assemble the components in whatever orientations one chooses. Furthermore, discontinuities in the mass and stiffness properties from element to element are permitted. However, when modeling warping deformations the line of shear centers, or elastic axis, plays a significant role. The current formulation approximates the elastic axis by a sequence of straight line segments and it is the desire to accurately represent the elastic axis that results in the preceding last two assumptions. Thus to the extent that warping effects are significant, failure to satisfy the last two assumptions and suitably approximate the elastic axis leads to error in the solution. In most cases however, and for the closed tubes representative of helicopter rotor blades, warping effects will be dominated by deformations arising from pure bending and torsion, and thus violation of these assumptions will not lead to significant error. This has been verified by numerical testing of the F.E. model for loaded structures containing 90° elbow joints and discontinuities in the beam stiffness properties.

4.1.2 Blade geometry

Each of the blade segments defined in the EHPIC/HERO blade geometry input corresponds to a single structural finite element. This is assumed to be adequate for the hover situation where static deflections are sought. The global axes for the assembled blade are denoted by XYZ corresponding to the blade axes defined in Figure 2-5. Local axes, xyz, are defined for each element such that the x-axis coincides with the elastic axis, or the line of shear centers, of the element. Axes y and z are derived from the transformation applied to the global Y and Z axes as described below. The transformation matrix relating the local element axes to the global axes is derived from the local segment layout specifications. The segment geometry is specified as follows (see Fig. 4-2):

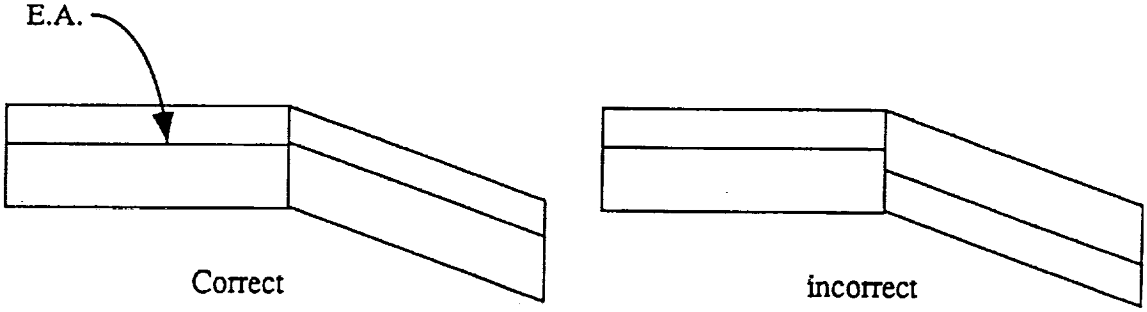

Figure 4-1. Correct and incorrect alignment of the elastic axis (E.A.) between adjacent elements.

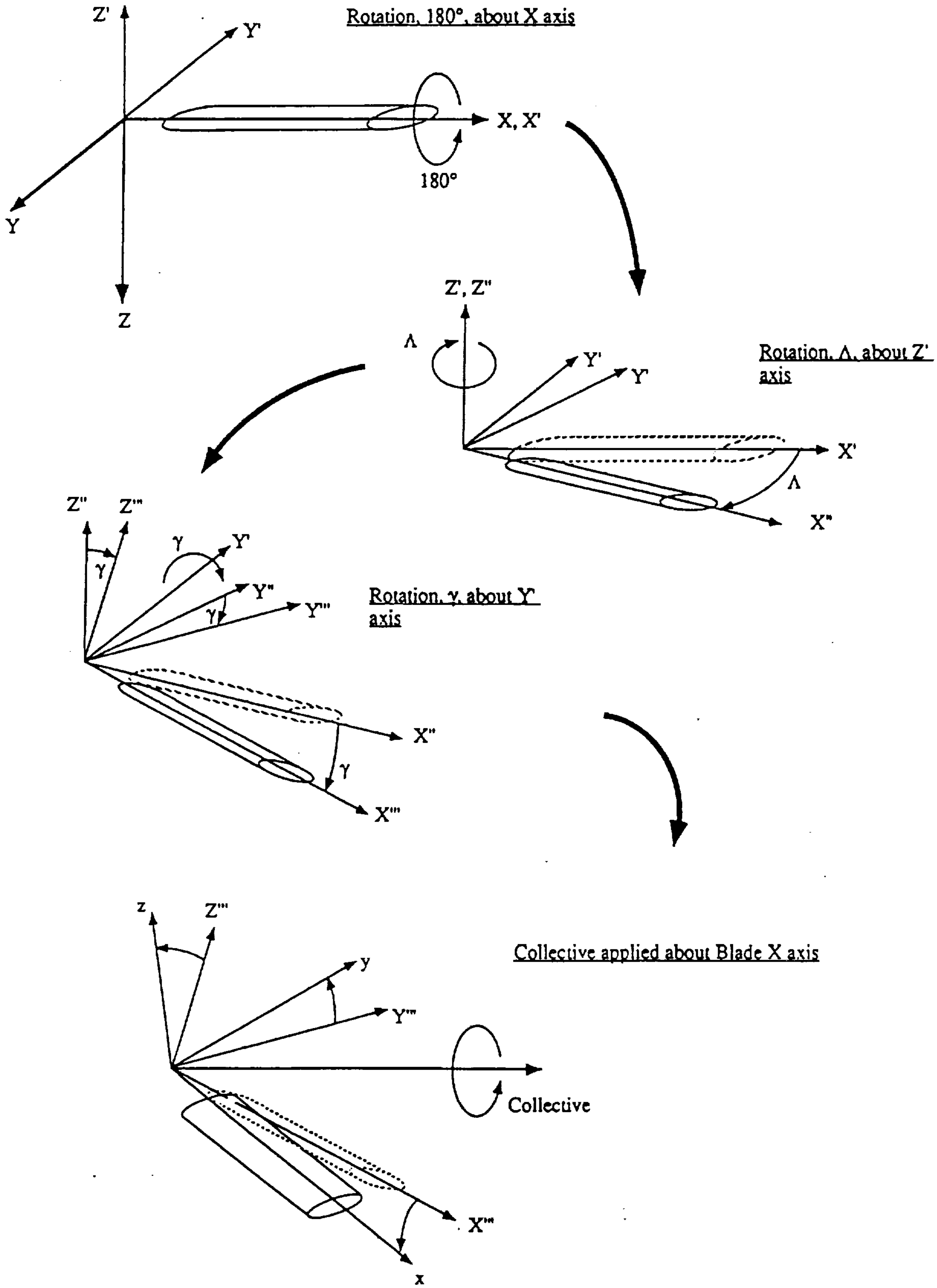

Figure 4-2. Sequence of rotations to go from blade axis system (X,Y,Z) to local element coordinate system (x,y,z).

(1) The planform is first defined. Each blade segment has length, SL, along the global X-direction and chord length, c, in the global Y-direction. The sweep, Λ, defines orientation of the quarter chord line for the segment. Note that for non-zero sweep, the length of the finite element along the quarter chord length differs from the length measured along the blade X-axis. If one finite element is associated with each blade segment then the element length shall in fact be:

$$l = \frac{SL}{\cos\gamma} \tag{4-1}$$

where γ is the anhedral (see step 3 below).

(2) A camber and then a pre-deformation twist gradient are defined over each segment. This information is not included in the transformation matrix since any effects due to camber and pre-twist upon structural properties can be more accurately specified in the information on blade cross-section properties (see Reference 12). Addition of camber would be reflected in the cross-sectional moments of area and pre-twisting would affect primarily the orientation of the principal axes. These parameters are directly specified in the blade cross-section input file discussed in Reference 12.

(3) Anhedral is then applied to each segment about an axis parallel to the global Y axis and passing through the left hand end (nearest to the rotor hub) of the segment. The direction of this rotation is in the negative Y-direction., i.e., positive anhedral, γ, results in the blade drooping down.

(4) Finally, collective pitch in the form of a rotation about the global X-axis is applied to the assembled structure.

This sequence of rotations is used to define the transformation matrix relating the local axes to the global ones of the EHPIC/HERO code. An additional 180° rotation about the global X-axis precedes the above rotations since the local finite element z-axis is positive upward whereas the global Z-axis is positive in the downward direction. The preceding parameters are supplied in the blade geometry input file.

From the above sequence of rotations the local and global axes are related by:

$$\begin{Bmatrix} X \\ Y \\ Z \end{Bmatrix} = \begin{Bmatrix} X_0 \\ Y_0 \\ Z_0 \end{Bmatrix} + T_c T_\gamma T_\Lambda T_{180°} \begin{Bmatrix} x \\ y \\ z \end{Bmatrix} \tag{4-2}$$

where $T_{180°}$, T_Λ, T_γ and T_c are the transformation matrices corresponding to the 180° rotation, sweep, anhedral and collective operations respectively, and the coordinates, $X_0Y_0Z_0$, are the global coordinates of the origin of the local axes. Here the origin lies on the elastic axis at the end of the element nearest the rotor hub. The combined matrix,

$$[T_{rot}] = T_c T_\gamma T_\Lambda T_{180°} = \begin{bmatrix} c_\gamma c_\Lambda & c_\gamma s_\Lambda & s_\gamma \\ c_c s_\Lambda - s_c s_\gamma c_\Lambda & -c_c c_\Lambda - s_c s_\gamma s_\Lambda & s_c c_\gamma \\ s_c s_\Lambda + c_c s_\gamma c_\Lambda & -s_c c_\Lambda + c_c s_\gamma s_\Lambda & -c_c c_\gamma \end{bmatrix} \tag{4-3}$$

where $s_{(\bullet)}$ and $c_{(\bullet)}$ denote sin(•) and cos(•) respectively. Note that the rotations due to deformation can also be referred to the global axes using this transformation since the deformations are assumed small and the rotations thus commute.

4.1.3 Element degrees of freedom

The specification of the shape functions and the fourteen degrees of freedom of each element is summarized here. Each element has two end nodes and one node at its midpoint, as shown in Figure 4-3. The degrees of freedom correspond to translational and rotational deformations at these nodes. The deformation of the element at any point is estimated by interpolation of the nodal displacements using the shape functions. Let u, v, and w denote the displacements along the local x, y, and z axes respectively and let θ denote the twist deformation about the x axis. Then the generalized displacement vector is defined as:

$$\text{Lag:} \begin{Bmatrix} q_1 \\ q_2 \\ q_3 \\ q_4 \end{Bmatrix} = \begin{Bmatrix} v(0) \\ v_{,x}(0) \\ v(l) \\ v_{,x}(l) \end{Bmatrix} \qquad \text{Flap:} \begin{Bmatrix} q_5 \\ q_6 \\ q_7 \\ q_8 \end{Bmatrix} = \begin{Bmatrix} w(0) \\ w_{,x}(0) \\ w(l) \\ w_{,x}(l) \end{Bmatrix}$$

$$\text{Twist:} \begin{Bmatrix} q_9 \\ q_{10} \\ q_{11} \end{Bmatrix} = \begin{Bmatrix} \theta(0) \\ \theta(l/2) \\ \theta(l) \end{Bmatrix} \qquad \text{Axial:} \begin{Bmatrix} q_{12} \\ q_{13} \\ q_{14} \end{Bmatrix} = \begin{Bmatrix} u(0) \\ u(l/2) \\ u(l) \end{Bmatrix} \tag{4-4}$$

where the subscript $(\bullet)_{,x}$ denotes the derivative with respect to the local x axis coordinate and l is the element length. Thus q_1 and q_2 refer to the displacement and corresponding slope due to bending in the y-direction at the left hand node. The corresponding right hand node deformations are q_3 and q_4, and so forth for the other displacements. Note that the slopes, $v_{,x}$ and $w_{,x}$, can be regarded as a small positive rotation about the local z-axis and a small negative rotation about the local y-axis respectively.

The transverse displacements, v and w, are interpolated using cubic Hermitian polynomials as is the common practice in beam finite element formulation. Quadratic polynomials are used to interpolate the torsional and axial deformations. This is the simplest element interpolation scheme yielding a consistent formulation for coupled torsion-bending (Reference 49). Specifically:

$$v(x) = \{\Phi_3\}^T \begin{Bmatrix} q_1 \\ q_2 \\ q_3 \\ q_4 \end{Bmatrix} \qquad w(x) = \{\Phi_3\}^T \begin{Bmatrix} q_5 \\ q_6 \\ q_7 \\ q_8 \end{Bmatrix}$$

$$\theta(x) = \{\Phi_2\}^T \begin{Bmatrix} q_9 \\ q_{10} \\ q_{11} \end{Bmatrix} \qquad u(x) = \{\Phi_2\}^T \begin{Bmatrix} q_{12} \\ q_{13} \\ q_{14} \end{Bmatrix} \tag{4-5}$$

Local Degrees of Freedom for Blade Element

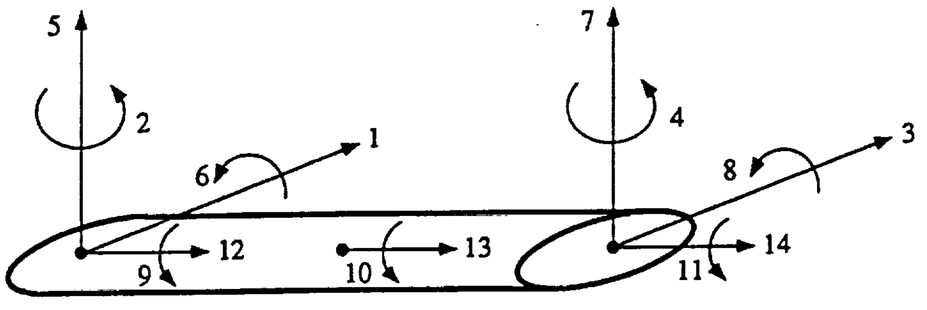

Assembly and Ordering of Global Degrees of Freedom

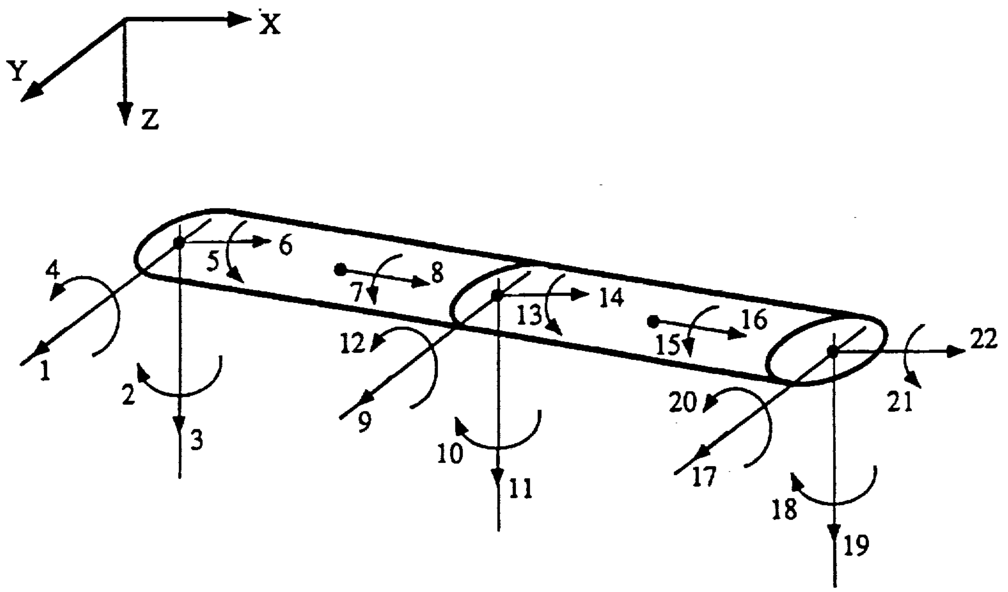

Figure 4-3. Definition of finite element degrees of freedom and schematic of the element ordering scheme.

where, $$\{\Phi_3\} = \begin{Bmatrix} 1 - 3\xi^2 + 2\xi^3 \\ (\xi - 2\xi^2 + \xi^3)\,l \\ 3\xi^2 - 2\xi^3 \\ (-\xi^2 + \xi^3)\,l \end{Bmatrix} \; ; \; \{\Phi_2\} = \begin{Bmatrix} 1 - 3\xi + 2\xi^2 \\ 4\xi - 4\xi^2 \\ -\xi + 2\xi^2 \end{Bmatrix} \tag{4-6}$$

and $\xi = x/l$. The preceding relations may be expressed in compact form as:

$$\begin{Bmatrix} v(x) \\ w(x) \\ \theta(x) \\ u(x) \end{Bmatrix} = [\,\Phi\,]\,\underline{q} \tag{4-7}$$

where $\{q\}$ is the vector of generalized displacements and $[\,\Phi\,]$ is a (4×14) matrix appropriately constructed from Eqs. (4-5) and (4-6).

Finally in the formulation of the elemental stiffness and mass matrices it is valuable to define principal axes of the cross-section, η and ζ, which are oriented such that:

$$\int_A \eta\zeta \, dA = 0 \tag{4-8}$$

The angle β is then the angle between the local y and η axes.

The global degrees of freedom are obtained by resolving the deformations along the global axes using the transformation matrix derived previously. At an end node, all of the three translational and three rotational d.o.f. are available (since the slopes of the transverse bending displacements correspond to rotations). Thus, the translation between the local element d.o.f.s and the global ones is achieved using the transformation matrix, T_{rot} :

$$\begin{Bmatrix} U \\ V \\ W \end{Bmatrix} = [\,T_{rot}\,] \begin{Bmatrix} u \\ v \\ w \end{Bmatrix} \; ; \; \begin{Bmatrix} R_X \\ R_Y \\ R_Z \end{Bmatrix} = [\,T_{rot}\,] \begin{Bmatrix} \theta \\ -w_{,x} \\ v_{,x} \end{Bmatrix} \tag{4-9}$$

where R_X , R_Y , and R_Z , are rotations due to deformation about the global XYZ axes respectively. At the mid-node the preceding translation is more involved since only two d.o.f., the twist and axial deformations, are available in the local axes and additional constraints are necessary to uniquely define the twist and stretch in the global directions. One approach would be to specify the four remaining local d.o.f at the mid-point by interpolating from the end-nodes using the element shape functions, i.e. evaluating $v(l/2)$, $w(l/2)$ and their slopes using Eqs. (4-5)-(4-7). These together with the local twist and extension deformations completely define the six local displacements from which the global deformations readily follow. However, it was found that this led to numerical problems in the resulting transformation matrix, since the complete element is singular for certain blade geometries. This might be expected from the observation that 18 global displacements (6 at each node) have been defined in terms of only 14 element d.o.f. Hence, the inverse transformation from global to local deformations is in fact non-unique.

The approach taken here is to simply define the global deformations to coincide with the respective local ones at the mid-node, i.e.,

$$\begin{Bmatrix} q_{10} \\ q_{13} \end{Bmatrix}_G = \begin{Bmatrix} q_{10} \\ q_{13} \end{Bmatrix}_L \tag{4-10}$$

This both simplifies the transformation and results in an orthogonal element transformation matrix, i.e., if the elemental transformation which will be composed of elements of $[T_{rot}]$ is denoted by $[T_{GL}]$ so that $\underline{q}_G = [T_{GL}]\,\underline{q}_L$ then $[T_{GL}]^{-1} = [T_{GL}]^T$. An alternative procedure would be to eliminate the mid-node d.o.f. using static condensation. However, this is unnecessary in light of the small number of d.o.f.s of the fully assembled model, the additional programming complexity and the further approximation that would thus be introduced.

4.1.4 Derivation of the element strains and stresses

In order to compute the elemental stiffness matrix the strains arising from the preceding displacements must be evaluated. The nonlinear expressions for the strains are stated:

$$\begin{aligned} \varepsilon_{xx} = {} & u_{,x} + (\Psi\theta_{,x})_{,x} + \frac{1}{2}(\eta^2 + \zeta^2)\,\theta_{,x}^{\,2} \\ & + \frac{1}{2}\,v_{,x}^{\,2} - v_{,xx}\,\{\,\eta\cos(\beta+\theta) - \zeta\sin(\beta+\theta)\,\} \\ & + \frac{1}{2}\,w_{,x}^{\,2} - w_{,xx}\,\{\,\zeta\cos(\beta+\theta) + \eta\sin(\beta+\theta)\,\} \end{aligned} \tag{4-11a}$$

$$\gamma_{x\eta} = 2\,\varepsilon_{x\eta} = (\Psi_{,\eta} - \zeta)(\theta_{,x} + \theta_{nl}) \tag{4-11b}$$

$$\gamma_{x\zeta} = 2\,\varepsilon_{x\zeta} = (\Psi_{,\zeta} + \eta)(\theta_{,x} + \theta_{nl}) \tag{4-11c}$$

and all other strains are assumed zero. Here, θ_{nl} is a nonlinear second order torsion term, and $\Psi(x,\eta,\zeta)$ is the Saint Venant warping function expressing the out-of-plane displacement, u_{warp}, due to torsion:

$$u_{warp}(x,\eta,\zeta) = \Psi(x,\eta,\zeta)\,\theta_{,x} \tag{4-12}$$

The linear expressions are easily obtained from above:

$$\begin{aligned} \varepsilon_{xx} = {} & u_{,x} + (\Psi\theta_{,x})_{,x} \\ & - v_{,xx}\,\{\,\eta\cos\beta - \zeta\sin\beta\,\} - w_{,xx}\,\{\,\zeta\cos\beta + \eta\sin\beta\,\} \end{aligned} \tag{4-13a}$$

$$\gamma_{x\eta} = (\Psi_{,\eta} - \zeta)\,\theta_{,x} \;;\quad \gamma_{x\zeta} = (\Psi_{,\zeta} + \eta)\,\theta_{,x} \tag{4-13b,c}$$

These strains are expressed in terms of the vector of generalized d.o.f., $\{q\}$, and the shape functions and their derivatives w.r.t. x , by substituting for the occurrences of u, v, w, and θ using the expressions, Eqs. (4-11)-(4-13). This results in:

$$\begin{aligned} \varepsilon_{xx} &= \left\{ \begin{matrix} -[\,\eta\cos\beta - \zeta\sin\beta\,]\,\{\Phi_3''\} \\ -[\,\zeta\cos\beta + \eta\sin\beta\,]\,\{\Phi_3''\} \\ \Psi_{,x}\,\{\Phi_2'\} + \Psi\{\Phi_2''\} \\ \{\Phi_2'\} \end{matrix} \right\}^T \{q\} \\ &= \{\,B_1\,\}^T\,\{q\} \end{aligned} \tag{4-14a}$$

$$\begin{aligned} \left\{ \begin{matrix} \gamma_{x\eta} \\ \gamma_{x\zeta} \end{matrix} \right\} &= \left\{ \begin{matrix} \Psi_{,\eta} - \zeta \\ \Psi_{,\zeta} + \eta \end{matrix} \right\} \left\{ \begin{matrix} 0 \\ 0 \\ \{\Phi_2'\} \\ 0 \end{matrix} \right\}^T \{q\} \\ &= \left\{ \begin{matrix} \{B_2\}^T \\ \{B_3\}^T \end{matrix} \right\} \{q\} \end{aligned} \tag{4-14b,c}$$

The corresponding stresses are derived from the Hooke's Law:

$$\sigma_{xx} = E\,\varepsilon_{xx} \tag{4-15a}$$

$$\sigma_{x\eta} = G\,\gamma_{x\eta} \quad ; \quad \sigma_{x\zeta} = G\,\gamma_{x\zeta} \tag{4-15b,c}$$

4.2 Derivation of the Equations of Static Equilibrium

The discussion above defines the relationships for stresses and strains for the current F.E. formulation. The required equilibrium equations are obtained via the principle of virtual displacements where virtual work expressions are constructed by considering the internal and applied forces subject to virtual displacements. In this framework, the usual material stiffness properties are represented by an internal virtual work expression, W^i, which in this case is equivalent to the variation of the strain energy expression. Since the internal virtual work can be written down directly, it is unnecessary to execute the intermediate step of obtaining an expression for the strain energy. The rotating XYZ reference frame gives rise to both inertial forces and geometric stiffening which can both be conveniently represented by an external virtual work term, W^e. The aerodynamic forces computed in the wake analysis constitute a further external virtual work term. Finally, the equations for static equilibrium are obtained by equating $W^i=W^e$.

The structural stiffness matrix K is composed of three terms, K_E, K_R, and K_G, where K_E is the usual material stiffness matrix obtained from the internal virtual work, and K_G and K_R are contributions due to the blade rotation. K_R is due to the centrifugal loading. This distributed inertial load gives rise to both a nodal force vector due to blade rotation and also a softening of the blade. The latter is physically due to the fact that displacement of a blade element places it at a different radial location and therefore alters its loading. A simple example of this is the case of deformation along the X-axis, u, at a radial location, r, for a blade rotating with angular velocity, Ω. A deformation u increases the centripetal acceleration from Ωr^2 to $\Omega(r+u)^2$ with a proportional increase in loading. This load increase induces a further displacement, δu, and in the linear F.E. model is equivalently accounted for by K_R. In the steady state deflection case for hover, K_R is obtained by developing an external virtual work term for the virtual displacements in the presence of the distributed centrifugal forces. The contribution K_G accounts for the geometric stiffening due to the axial tensile loading induced by blade rotation. The geometric stiffening plays a major role in the range of angular velocities typical for helicopters. This effect is analogous to the buckling problem where the axial force is compressive and generates internal distributed moments when the blade deforms.

For simple blade bending examples the blade stiffening effect, K_G, is found to be twice the softening contribution, K_R, leading to a net increase in blade stiffness, as is clearly the expected behavior. K_G is derived by expressing the forces and moments due to rotation explicitly and regarding these as externally applied loads that are accounted for by an additional external virtual work term. The external virtual work expression then results from these applied loads undergoing virtual displacements. This approach is frequently adopted in buckling analysis and bending and torsion problems where axial forces are present.

4.2.1 Construction of K_E

The internal virtual work due is given by:

$$W^i = \int_V \sigma_{xx} \cdot \delta\varepsilon_{xx} + \sigma_{x\eta} \cdot \delta\gamma_{x\eta} + \sigma_{x\xi} \cdot \delta\gamma_{x\xi} \, dV \qquad (4\text{-}16)$$

Substituting for the stresses and breaking up the volume integral:

$$W^i = \int_0^l \{ \int_A E\varepsilon_{xx} \cdot \delta\varepsilon_{xx} + G\gamma_{x\eta} \cdot \delta\gamma_{x\eta} + G\gamma_{x\xi} \cdot \delta\gamma_{x\xi} \, dA \} \, dx \qquad (4\text{-}17)$$

Substituting for the strains using Eq. (4-14) and performing the integrations results in:

$$W^i = \delta \underset{\sim}{q}^T [K_E] \underset{\sim}{q} \qquad (4\text{-}18a)$$

where the desired stiffness matrix is

$$K_E = \int_0^l \{ \int_A E\{B_1\}\{B_1\}^T + G(\{B_2\}\{B_2\}^T + \{B_3\}\{B_3\}^T) \, dA \} dx \qquad (4\text{-}18b)$$

The construction of K_E requires a sequence of integrations, the first being an area integration over the area of cross-section at a given station, x , along the element, and the second being the integral along the length of the element. Evaluation of the area integral results in expressions containing various properties of cross-section multiplied by the shape functions and their derivatives w.r.t. x . These properties include the cross-sectional area, moments of area, area centroids relative to the η and ζ axes, and a total of nine integrals involving the warping function, Ψ. The finite element implementation employed in EHPIC/HERO does not compute these properties, but instead requires that the various cross-sectional area integrals be input directly via the blade cross-section input file. The finite element code requires that these properties be specified at the end nodes of each element and assumes that they vary linearly between the end nodes. The final integration along the element length involves products of the shape functions and their derivatives and is effected numerically using Gaussian integration. A list of the cross-section area integrals required in the analysis is given in Reference 12.

4.2.2 Construction of K_R and $\underline{f}^{rot}$

In order to determine the contributions to the stiffness matrix and the nodal forces due to blade rotation one first defines the position vector of a point on the blade in blade coordinates,

$$\underline{R}(X,Y,Z) = X\underline{I}+Y\underline{J}+Z\underline{K}$$

or,
$$\begin{Bmatrix} X\\ Y\\ Z\end{Bmatrix} = \begin{Bmatrix} X_0\\ Y_0\\ Z_0\end{Bmatrix} + [T_{rot}]\begin{Bmatrix} x_{ie}+u\\ v+\eta\cos(\beta+\theta)-\zeta\sin(\beta+\theta)\\ w+\eta\sin(\beta+\theta)+\zeta\cos(\beta+\theta)\end{Bmatrix} \tag{4-19a}$$

which in local coordinates is,

$$\begin{Bmatrix} x\\ y\\ z\end{Bmatrix} = [T_{rot}]^T\begin{Bmatrix} X_0\\ Y_0\\ Z_0\end{Bmatrix} + \begin{Bmatrix} x_{ie}+u\\ v+\eta\cos(\beta+\theta)-\zeta\sin(\beta+\theta)\\ w+\eta\sin(\beta+\theta)+\zeta\cos(\beta+\theta)\end{Bmatrix} \tag{4-19b}$$

where x_{ie} is the distance along the elastic axis of the element containing the point. Then the body force at any point on the blade due to rotation is:

$$\underline{f} = -\rho\,(\Omega\underline{K})\times\{(\Omega\underline{K})\times\underline{R}\} \tag{4-20}$$

where ρ is the density of the blade material, and the unit vectors are aligned with the global axes. When expressed in the local coordinate system of a particular element, this becomes,

$$\begin{Bmatrix} f_x\\ f_y\\ f_z\end{Bmatrix} = \Omega^2[T_{rot}]^T\left(\begin{Bmatrix} X_0\\ Y_0\\ 0\end{Bmatrix} + \begin{bmatrix} 1 & 0 & 0\\ 0 & 1 & 0\\ 0 & 0 & 0\end{bmatrix}[T_{rot}]\begin{Bmatrix} x_{ie}+u\\ v+\eta\cos(\beta+\theta)-\zeta\sin(\beta+\theta)\\ w+\eta\sin(\beta+\theta)+\zeta\cos(\beta+\theta)\end{Bmatrix}\right) \tag{4-21}$$

The moment about a point on the element elastic axis, $\underline{R}_{ea} = X_{ea}\underline{I}+Y_{ea}\underline{J}+Z_{ea}\underline{K}$, due to the rotational force acting on a volume element located at $\underline{R}$ somewhere on the blade is,

$$\underline{m} = (\underline{R} - \underline{R}_{ea}) \times \underline{f}\, dA\, dx \tag{4-22}$$

The net forces and moments at a point on the elastic axis defined by x_{ea} are:

$$\underline{F} = \int_{X_{ea}}^{R} \left\{ \int_{A} \underline{f}(x,y,z)\, dA \right\} dX \tag{4-23a}$$

$$\underline{M} = \int_{X_{ea}}^{R} \left\{ \int_{A} [\underline{R}(X,Y,Z) - \underline{R}_{ea}(X_{ea},Y_{ea},Z_{ea})] \times \underline{f}(X,Y,Z) dA \right\} dX \tag{4-23b}$$

where R is the value of X_{ea} at the blade tip. The domain of integration extends from X_{ea} to the blade tip since the net force and moment vectors vanish at the blade tip.

The external virtual work for the inertial forces is obtained by considering the body force due to blade rotation, $\underline{f}$, as a distributed external force. Imposing virtual displacements upon the blade under this distributed load results in the formation of the external work term:

$$W_R^e = \int_0^1 \int_A f_x \delta u + f_y \delta v + f_z \delta w + (y f_z - z f_y)\delta\theta \, dA \, dx_{ie} \tag{4-24}$$

The remaining procedure is laborious, but straightforward and is briefly summarized below:

- Resolve Eqs. (4-19) to (4-24), in the local element coordinate system.
- Substitute for all occurrences of u , v , w , and θ , and their derivatives using Eqs. (4-5) and (4-4).
- Replace $\sin(\beta+\theta)$ and $\cos(\beta+\theta)$ by the small θ approximations.
- Substitute for $\underline{f}$ in Eq. (4-24) and discard all terms of order higher than 2.
- Carry out the cross-section area integrations. As in the computation for K_E, this area integral can be directly expressed in terms of certain cross-section properties. Since the blade material density, ρ, is now present in the analysis these cross-section properties will be quantities such as the mass per unit length, cross-sectional center of mass, torsional moment of inertia per unit length, etc. The complete list of parameters needed is given in Reference 12.
- Finally, evaluate Eq. (4-24) from $x_{ie}=0$ to $x_{ie}=1$ using Gaussian integration.

The resulting integral assumes the form,

$$W_R^e = -\delta\underline{q}^T \Omega^2 \int_0^l [A_0]\,\underline{q} - \{B_0\}\,dx$$

or,
$$W_R^e = \delta\underline{q}^T \left(-[K_R]\,\underline{q} + \underline{f}^{rot} \right) \qquad (4\text{-}25)$$

where the contribution to the stiffness matrix,

$$K_R = \Omega^2 \int_0^l [A_0]\,dx \qquad (4\text{-}26)$$

and the nodal force vector due to the centrifugal forces,

$$\underline{f}^{rot} = \Omega^2 \int_0^l \{B_0\}\,dx \qquad (4\text{-}27)$$

4.2.3 Construction of K_G

The virtual work expression for the net blade rotation forces undergoing virtual deformations that accounts for the geometric stiffening effects is stated (see Reference 49):

$$W_G^e = \int_0^l \{F_x\,(v'\delta v' + w'\delta w') + M_y\,\delta(v''\theta) + M_z\,\delta(w''\theta)$$
$$+ Q\theta'\delta(\theta') + \frac{1}{2} M_x\,\delta(v''w' - w''v')\ \}\,dx_{ie} \qquad (4\text{-}28)$$

Here,

$$Q = \frac{1}{A}\int_A F_x\,(y^2 + z^2)\,dA \qquad (4\text{-}29)$$

and the terms, F_x, M_x, M_y, and M_z are simply the local components of the net forces and moments due to rotation summed over the portion of blade lying outboard of the point x_{ie} on the elastic axis. Note that the first term in Eq. (4-28) represents the usual additional stiffening due to an axial force. The virtual work contribution for this first term may be viewed as a differential moment arising from structural deformation, $dM_z = F_x(v'dx)$ and $dM_y = F_x(-w'dx)$, moving through virtual rotations, $\delta v'$ and $\delta(-w')$.

Eqs. (4-19)-(4-23) and (4-28)-(4-29) contain all of the information necessary for the computation of $[\,K_G\,]$. Again the actual computation is laborious, but straightforward.

One begins by substituting for $\underline{f}$, m_x, F_x, $\underline{M}$, and Q in Eq. (4-28) and discarding all terms of order higher than 2. The sin(•) and cos(•) are replaced by their small θ angle approximations, and the occurrences of u, v, w, and θ are evaluated from Eqs. (4-4) and (4-5). The cross-section area integrations are performed to define mass moments of area. Finally, use of integration by parts where possible simplifies the integration along the element from $x_{ie}=0$ to $x_{ie}=l$ of Eq. (4-28). For example, the first term,

$$\int_0^l \{F_x (v'\delta v'+w'\delta w')\, dx_{ie} = \left[F_x(x_{ie}) \int_0^{x_{ie}} v'\delta v'+w'\delta w' d\mu \right]_{x_{ie}=0}^{x_{ie}=l}$$

$$+ \int_0^l f_x \{ \int_0^{x_{ie}} (v'\delta v'+w'\delta w')\, d\mu \} \; dx_{ie} \qquad (4\text{-}30)$$

The quantity $(v'\delta v'+w'\delta w')$ is easily evaluated from Eq. (4-7) in terms of the element shape functions and the generalized vector of nodal displacements, $\underline{q}$. Thus the integral contained in the brackets {•} can be written down analytically. The final integration along the element from $x_{ie}=0$ to $x_{ie}=l$ is done by Gaussian integration. and results in,

$$W_r^e = - \delta\underline{q}^T [K_G] \underline{q} \qquad (4\text{-}31)$$

where the geometric stiffening matrix, K_G, is proportional to Ω^2 .

4.2.4 Computation of $\underline{f}^{aero}$

The coupling of the structural model to the aerodynamic wake analysis is achieved by evaluating the nodal force vector, $\underline{f}^{aero}$, due to the distributed aerodynamic forces and moments. The associated external virtual work term is derived in a very similar procedure to that used in developing the rotational force vector, $\underline{f}^{rot}$. The wake analysis presents the finite element routines with an array, QFRC(iseg,ic,k), which represents the aerodynamic force on chordwise panel, ic, of blade segment, iseg, in the global blade axis direction, k. The index k=1,2,3 denotes the aerodynamic force in the X, Y, Z directions respectively (thus k=2 denotes the drag and k=3 the negative of the thrust for the chordwise panel), and k=4 represents the aerodynamic pitching moment about the X-axis.

To derive the corresponding nodal forces, the aerodynamic forces per unit length is first obtained by dividing entries of QFRC by the panel width, dX. The resulting vector is rotated into the local reference frame to obtain local forces and moments per unit length,

$$\underset{\sim}{f}^a = \begin{Bmatrix} f_x^a \\ f_y^a \\ f_z^a \end{Bmatrix} \quad ; \quad \underset{\sim}{m}^a = \begin{Bmatrix} m_x^a \\ m_y^a \\ m_z^a \end{Bmatrix} \tag{4-32}$$

The external virtual work expression for the aerodynamic forces is then (c.f. Eq. (4-24))

$$W_A^e = \int_0^1 f_x^a \delta u + f_y^a \delta v + f_z^a \delta w + m_x^a \delta\theta + m_y^a \delta(-w,_x) + m_z^a \delta(v,_x) \;\; dx_{ie} \tag{4-33}$$

which is evaluated as before by substituting for the deformations, u, v, w, and θ, and numerically integrating to obtain,

$$W_A^e = \delta \underset{\sim}{q}^T \underset{\sim}{f}^{aero} \tag{4-34}$$

4.2.5 Equations of equilibrium

The derivation of the virtual work terms is now complete. The equations of motion follow immediately from equating the internal and external virtual work terms, $W^i = W^e$, using Eqs. (4-18), (4-25), (4-31), and (4-34):

$$\delta \underset{\sim}{q}^T [\, K_E \,] \underset{\sim}{q} = \delta \underset{\sim}{q}^T (\, -[K_R] \underset{\sim}{q} + \underset{\sim}{f}^{rot} \,) - \delta \underset{\sim}{q}^T [\, K_G \,] \underset{\sim}{q} + \delta \underset{\sim}{q}^T \underset{\sim}{f}^{aero}$$

or, since the virtual displacements are arbitrary,

$$[\, K_E + K_R + K_G \,] \underset{\sim}{q} = \underset{\sim}{f}^{rot} + \underset{\sim}{f}^{aero} \tag{4-35}$$

4.3 Assembly of the Global Stiffness Matrix and Forces

The preceding equation, Eq. (4-35), implies an assembly process of the individual element stiffness matrices and nodal forces into a corresponding global stiffness matrix and applied force vector for the complete helicopter blade. The assembly process involves three sub-procedures: the first involves referring the elemental matrices and nodal forces to the global axes, the second defines the array indexing that relates the local degrees of freedom for each element to the global ones, and the final step entails implementation of the boundary conditions at the blade root.

Rotation of the element matrices and nodal forces into a global coordinate frame is accomplished in the standard manner:

$$[\, K_{global} \,] = [T_{GL}] [\, K_{local} \,] [T_{GL}]^T \tag{4-36a}$$

$$\{\underset{\sim}{f}^{rot}\}_{global} = [T_{GL}] \{\underset{\sim}{f}^{rot}\}_{local} \tag{4-36b}$$

$$\{\underline{f}^{aero}\}_{global} = [T_{GL}]\{\underline{f}^{aero}\}_{local} \qquad (4\text{-}36c)$$

as may be easily verified by noting that the potential energy and the virtual work are independent of the choice of reference frame. Here, $[T_{GL}]$ is the transformation matrix described in Section 4.2 relating local d.o.f., $\underline{q}$, and global generalized d.o.f., $\underline{s}$: $\underline{s} = [T_{GL}]\,\underline{q}$.

The blade elements are then laid end to end in sequence from blade root to blade tip. Global deformations are defined as outlined in Eqs. (4-9) and (4-10). However, the ordering of the global degrees of freedom is different from the local ones, Eq. (4-4). Each element degree of freedom is associated with a global one via an indexing array or splay matrix, C(k,ie), where k is the local degree of freedom (k=1,2,...14), ie is the element number, and C(k,ie) is the global degree of freedom. Having specified a C(k,ie) for each element then the global matrices may be constructed by 'splaying' components of the elemental mass and stiffness matrices into their corresponding positions in the global matrices. For example, the [i,j] entry of the elemental stiffness matrix for finite element, ie, is added to the [C(i,ie),C(j,ie)] entry of the global stiffness matrix. In like manner, the global nodal force vector is built up from nodal forces for each element.

It remains to specify the actual ordering of the global degrees of freedom. Degrees of freedom are numbered upwards starting at the blade root. Using the definitions for global displacements and rotations given in Section 4.2, Eqs. (4-9) and (4-10), the global degrees of freedom are summarized in Table 4-1 (see also Fig. 4-3).

The construction of the global stiffness matrix is completed by imposing the boundary conditions at the root. For articulated blades, it is implicitly assumed in EHPIC/HERO that the blade is freely hinged in both flap and lag directions, but that the remaining degrees of freedom at the root - the three translational displacements and the twist about the X axis - are constrained. The boundary conditions are implemented by simply deleting the rows and columns of the global stiffness matrix corresponding to these four degrees of freedom. For cantilevered blades, by definition all root deformations are zero and thus all six degrees of freedom at the root must be removed.

4.4 Solution of the Structural Equations

For a given nodal force vector, $\underline{f}=\underline{f}^{rot}+\underline{f}^{aero}$, it is required to solve the finite element equations,

$$[K]\,\underline{s} = \underline{f} \qquad (4\text{-}37)$$

for the global deformation vector, $\underline{s}$. The iterative solution process whereby the final deformed blade geometry and associated wake structure are obtained, gives rise to a series of nodal force vectors, $\underline{f}$, which changes as the flow-field is updated. For a fixed undeformed blade planform [K] remains unchanged so that Eq. (4-37) is repeatedly solved for a sequence of right hand sides. The LU decomposition procedure is most amenable to this type of problem since the LU decomposition of [K] need only be performed once. The solution $\underline{s}$ for any $\underline{f}$ is then obtained by a computationally cheap backsubstitution procedure.

The end-to-end layout of the beam elements and numbering of the d.o.f. results in a banded stiffness matrix with maximum bandwidth, mb=22. In EHPIC/HERO, the non-zero elements of [K] are stored in an array B according to,

$$B(j-i+14\,,\,i) = [K]_{ij} \qquad (4\text{-}38)$$

This is the storage form required by the pair of efficient banded LU decomposition and backsubstitution subroutines DECB and SOLB of Reference 50. The LU decomposition is performed once by calling DECB immediately subsequent to the construction of the array, B. The nodal deflections are then obtained for each of the nodal force vectors by the backsubstitution routine SOLB.

For certain wake layouts and blades, the iterative process has been observed to become unstable, particularly for high resolution wake models or relatively soft blades. This is believed to be due to the change in structural deformation, and hence the blade geometry, that takes place between consecutive iterations. If this change is too large, kinks in the trailing filaments develop and undermines convergence. To counter this possibility, the maximum change in deformation state during an iteration, $\Delta \underline{s}$, is limited by the parameters DLD and DLR supplied by the user. Here DLD is the maximum change in displacement deformation between EHPIC/HERO iteration steps, and DLR the corresponding maximum change in rotation deformation. If any element of $\Delta \underline{s}$ is found to exceed these limits, then the whole vector, $\Delta \underline{s}$, is scaled so that the maximum change requirement is satisfied. The deformation state is then updated, $\underline{s} \leftarrow \underline{s} + \Delta \underline{s}$, using the scaled version of $\Delta \underline{s}$. This limiting is not applied during the initial relaxation since this portion of the calculation tends to be relatively insensitive to characteristic changes $\Delta \underline{s}$.

Since the overall process is iterative, a tolerance parameter, analogous to those used to test for wake convergence, is supplied to verify that the structural computation has converged. The required test for all i takes the form:

displacement deformations: $\Delta s_i < \mathrm{CONVGS} * R$ (4-39a)

rotation deformations: $\Delta s_i < \mathrm{CONVGS}$ (4-39b)

where CONVGS is the user supplied tolerance parameter.

4.5 Update of Blade Geometry

The coupling of the structural model is completed by specifying the relation between the global deformation vector, $\underline{s}$, and the geometrical parameters used to specify the blade layout. As described in Reference 12, the blade geometry is defined by the variables:

SL(iseg) - segment X-length
SWEEP(iseg) - segment sweep
TWG(iseg) - segment twist gradient
TWR(iseg) - twist at left hand end of segment
ANH(iseg) - segment anhedral
CHORD(iseg) - chord length at left hand end of segment
COLL - blade collective.

In EHPIC/HERO, the undeformed versions of these quantities are input by the user and for optimization problems represent the design variables. The blade layout routines require the deformed quantities which are obtained by superimposing the deformation vector, $\underline{s}$, upon the undeformed shape. Table 4-1 summarizes the information contained in the vector, $\underline{s}$. Denoting the variables at the left hand end of a segment by $(\bullet)_L$, those at the right hand end by $(\bullet)_R$, and the undeformed geometry by $(\bullet)_0$, then the deformed geometry,

$$
\begin{aligned}
&\mathrm{SL} && = \mathrm{SL}_0 + U_L - U_R \\
&\mathrm{SWEEP} && = \mathrm{SWEEP}_0 + \mathrm{AVS0}*\cos(\mathrm{COLL}) + \mathrm{AVG0}*\sin(\mathrm{COLL}) \\
&\mathrm{TWG} && = \mathrm{TWG}_0 + \left[(R_X)_L - (R_X)_R \right] / \mathrm{SL} \\
&\mathrm{TWR} && = \mathrm{TWR}_0 + (R_X)_L \\
&\mathrm{ANH} && = \mathrm{ANH}_0 + \mathrm{AVG0}*\cos(\mathrm{COLL}) - \mathrm{AVS0}*\sin(\mathrm{COLL}) \\
&\mathrm{CHORD} && - \text{ unchanged by } \underline{s} \\
&\mathrm{COLL} && - \text{ unchanged by } \underline{s}
\end{aligned}
\tag{4-40}
$$

where,
$$
\begin{aligned}
\mathrm{AVS0} &= \tfrac{1}{2}\left[(R_Z)_L + (R_Z)_R \right] \\
\mathrm{AVG0} &= -\tfrac{1}{2}\left[(R_Y)_L + (R_Y)_R \right]
\end{aligned}
$$

This takes into account the global rotation about the X-axis of the entire blade when applying the collective after the blade planform has been defined.

4.6 A Note on the Wake/Structure Coupling Matrix

The structural equations, Eq. (4-37) can be expressed as,

$$\Delta \underline{f} = \{ \underline{f} - K\underline{s} \} = K\,\Delta \underline{s} \tag{4-41}$$

where the deformation is updated $\underline{s} \leftarrow \underline{s} + \Delta\underline{s}$. This can be combined with the wake equations so that,

$$
\begin{Bmatrix} \Delta \underline{q} \\ \Delta \underline{w} \\ \Delta \underline{f} \end{Bmatrix}
=
\begin{bmatrix} Q_{qx} & Q_{q\gamma} & 0 \\ Q_{wx} & Q_{w\gamma} & 0 \\ 0 & 0 & K \end{bmatrix}
\begin{Bmatrix} \Delta \underline{x}_c \\ \Delta \underline{\gamma} \\ \Delta \underline{s} \end{Bmatrix}
\tag{4-42}
$$

The left hand side residuals formed from nonlinear equations are driven to zero by an iterative process that amounts to a Newton method for updating the $\underline{x}_c$, $\underline{\gamma}$, and $\underline{s}$. The right hand matrix of first order linear derivative terms does not reflect the coupling between the aerodynamic and structural equations and so the question arises as to whether the coupling terms should also be derived. Note that the accuracy of the analysis is entirely dependent upon the computation of the left hand vector of Eq. (4-42). The implicit coupling of the two sets of equations is also embodied in the left hand terms. The role of the right hand side matrix is to enhance the convergence of the iterative scheme providing superior stability and rate of convergence to the overall scheme. Thus, provided that this goal is achieved, one is at liberty to make approximations to its elements.

Our experience indicates that neglecting the block off-diagonal coupling matrices is both an adequate and desirable approximation. Earlier version of the code included the off-diagonal coupling terms which were derived at considerable computational cost. It was found that the overall rate of convergence was minimal when compared against the present case with matrix coupling entries neglected. Furthermore, the robustness of the overall solution scheme was comparable in both cases and was found to be best controlled by specifying the parameters DLD and DLR in sensitive cases. The approximation is very desirable for several reasons: 1) Evaluation of the off-diagonal terms is very expensive in computer time and requires substantial storage space; 2) The advantages of the efficient banded LU decomposition scheme described in Section 4.4 are forfeited. Instead, the Gaussian elimination scheme employed in EHPIC/HERO for solving the N wake equations is now applied to an (N+NF)*(N+NF) array where NF is the no. of degrees of freedom in the structural model. Hence the number of operations involved in Gaussian elimination increases from $O(N^3)$ to $O([N+NF]^3)$. 3) There is a substantial reduction in coding complexity. 4) For optimization studies, the effects of structural deformation are more efficiently incorporated by recomputing the structural stiffness properties and deflections for perturbed designs. Therefore, the coupling entries in the right hand matrix term in Eq. (4-42) may be safely neglected resulting in substantial reduction in computational resources with no noticeable loss in robustness.

TABLE 4-1

Specification of the Global Degrees of Freedom For Element, ie.

	Global Deformation	Degree of Freedom
Left-hand node of element, ie:	V	s_{8ie-7}
	R_Z	s_{8ie-6}
	W	s_{8ie-5}
	R_Y	s_{8ie-4}
	R_X	s_{8ie-3}
	U	s_{8ie-2}
Mid-node of element, ie:	q_{10}	s_{8ie-1}
	q_{13}	s_{8ie}
Right-hand node of element, ie:	V	s_{8ie+1}
	R_Z	s_{8ie+2}
	W	s_{8ie+3}
	R_Y	s_{8ie+4}
	R_X	s_{8ie+5}
	U	s_{8ie+6}

5. IMPLEMENTATION OF DESIGN OPTIMIZATION

5.1 Outline of the Optimization Solution Method

The fundamental procedural elements involved in optimizing the rotor design in EHPIC/HERO are outlined in Fig. 5-1. The initialization routine specifies the objective function, the design variables and the optimization method to be employed. The subsequent optimization process is iterative and involves sequential evaluation of local objective function and constraint derivatives, pre-processing this information into suitable input to the optimization algorithm, implementing the improved design, and re-converging the wake analysis in EHPIC/HERO. The basic routines that carry out these procedures are also indicated in Fig. 5-1. This section describes each of these operations and their computational implementations.

5.1.1 Optimization algorithms

It is appropriate to begin with a description of the optimization algorithm since the input required to specify the minimization problem dictates the information that must be supplied by other routines. Thus, the set of computer code modifications and additions that have been effected in EHPIC/HERO to carry out the optimization process depend fundamentally on the core optimization algorithms employed. Conversely however, for problems of this scale, the computational cost involved in providing this information will limit our choice of practical optimization methods. Therefore, the selection of a suitable optimization scheme is itself an attempt to optimize the fundamental trade-off between the rate of convergence to an optimal design over a series of iteration steps and the amount of computation required per iteration.

In general, the constrained optimization problem may be posed:

Minimize $J(\underline{X})$ subject to the constraints

$$\begin{array}{lll} g_j(\underline{X}) \le 0 & , & j=1,\ldots,m_i \\ g_k(\underline{X}) = 0 & , & k=m_i+1,\ldots,m_e \\ l_i \le x_i \le u_i & , & i=1,\ldots,n \end{array} \tag{5-1}$$

where $\underline{X}$ is the state vector of order n, J is the objective function to be minimized by appropriate choice of $\underline{X}$, the g_j and g_k are the m_i inequality and m_e equality constraints, and l_i and u_i define lower and upper bounds for the corresponding design variable, x_i. In the context of rotor design optimization in hover, the complete state variable vector, $\underline{X} = \{ \underline{x}_c, \underline{\gamma}, \underline{s}, \underline{d} \}^T$ where $\underline{x}_c$ and $\underline{\gamma}$ are the wake collocation point locations and blade quadrilateral bound circulations used in the EHPIC/HERO analysis, $\underline{s}$, are the structural deflections, and the vector, $\underline{d}$, constitutes the set of design variables such as blade twist, sweep, and anhedral.

In practice, for the performance objective functions considered here, structural deformations, $\underline{s}$, are eliminated prior to posing the optimization task. Instead, effects due to structural deformation are implicitly accounted for when evaluating the derivatives for the design vector, $\underline{d}$. Candidate objective functions, $J(\underline{X})$, include the power arising from induced drag or profile drag, thrust, the Figure of Merit, or a combination of these. Examples of imposed constraints include such requirements as maintaining constant

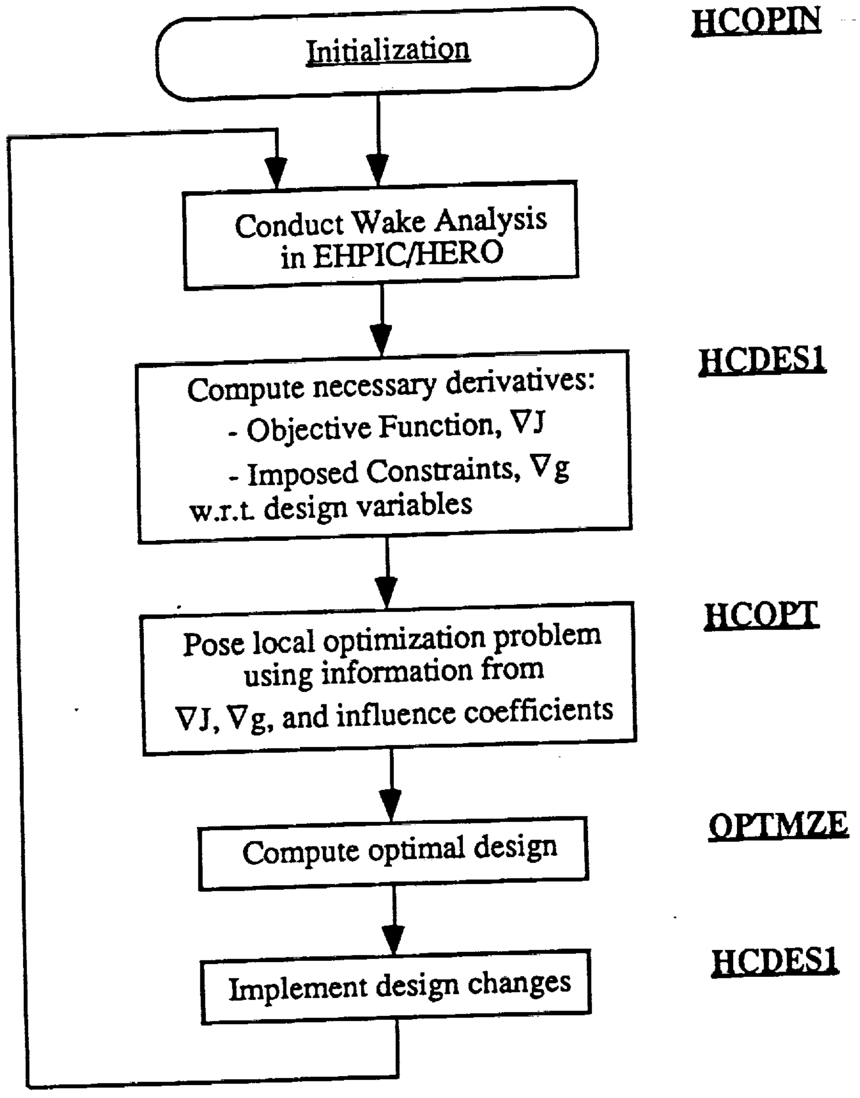

Figure 5-1. Flow chart of overall optimization process and the main subroutines involved.

thrust or remaining below a specified total power ceiling. Note that the equations used in the wake calculation are used to form equality constraints, g_k, relating the $\underline{x}_c$, $\underline{y}$ and $\underline{d}$ [see Eq. (5-26)]. As described below, these equality constraints can be either used directly as input into the optimization routine or else employed to eliminate the $\underline{x}_c$, $\underline{y}$. The latter is more efficient, but one forfeits the ability to impose constraints on the perturbations in $\underline{x}_c$ and $\underline{y}$.

In general, the functions, J and g_i are nonlinear. Furthermore, analytical expressions for these functions in terms of $\underline{X}$ are usually unavailable and their evaluation is carried out in a post-processing phase after the hover solution has converged. Thus, although $J(\underline{X})$ and $g(\underline{X})$ can be obtained given $\underline{X}$ the derivatives of these functions are typically available only by numerical differencing. We observe that the influence coefficients employed in the wake analysis are basically finite difference approximations to the first derivatives of collocation cross-flow velocities, $\underline{q}$, and downwash velocities, $\underline{w}$, w.r.t. $\underline{x}_c$, and $\underline{y}$. The approximation of the first derivatives of these quantities w.r.t. to the design parameters, $\underline{d}$, exacts a computational cost comparable to that of obtaining the other influence coefficients and is judged acceptable. Thus, an optimization technique that uses first order information is highly desirable since much of the necessary data is already available from the wake analysis, and the remaining information can be determined with the same order of computational cost as incurred in one wake analysis iteration. Zeroth order techniques using only the evaluated $J(\underline{X})$ and $g_i(\underline{X})$ are wasteful of the first order available information and require excessive iterations to converge. Second order methods are judged prohibitive as a result of excessive computational cost involved in evaluating the second order derivatives, $\left.\frac{\partial^2 J}{\partial X^2}\right|_{\underline{X}=\underline{X}^*}$ and $\left.\frac{\partial^2 g_i}{\partial X^2}\right|_{\underline{X}=\underline{X}^*}$.

5.1.2 Review of the Phase I optimization scheme

The first version of the wake analysis with optimization capability employed a sequential linear programming (SLP) technique as the core optimization technique (References 51, 52). As described in Reference 4, the nonlinear, $J(\underline{X})$ and $g(\underline{X})$ are linearized about the current design and wake solution,

$$J(\underline{X}) \approx J(\underline{X}^*) + \nabla J(\underline{X}^*)\,\Delta\underline{X} \tag{5-2}$$

where the constraint

$$0 = g_k(\underline{X}) \approx g_k(\underline{X}^*) + \nabla g_k(\underline{X}^*)\,\Delta\underline{X} \tag{5-3}$$

is imposed. In Reference 4, $J(\underline{X})$ was equated with the total power required by the blade, and the set of equality constraints, $g_i(\underline{X})$, is composed of a thrust constraint to maintain constant thrust. The set of equations used in the wake solution and extended to account for design variable perturbations. The twist gradient over each blade segment constituted the design vector. The state vector, $\underline{X}^*$, denotes the current design and converged wake description, and $\Delta\underline{X}$ perturbations about that solution. Specifically, the posed problem was to minimize the power expressed as,

$$P \approx P(\underline{X}^{*}) + \left\{P_{x}, P_{\gamma}\right\}\begin{Bmatrix}\Delta \underline{x}_{c} \\ \Delta \underline{\gamma}\end{Bmatrix} + \left\{P_{d}\right\}\left\{\Delta \underline{d}\right\} \tag{5-4}$$

subject to constant thrust,

$$0 = T - T_{0} \approx T(\underline{X}^{*}) - T_{0} + \left\{T_{x}, T_{\gamma}\right\}\begin{Bmatrix}\Delta \underline{x}_{c} \\ \Delta \underline{\gamma}\end{Bmatrix} + \left\{T_{d}\right\}\left\{\Delta \underline{d}\right\} \tag{5-5}$$

the wake constraints,

$$\begin{Bmatrix}0 \\ 0\end{Bmatrix} = \begin{Bmatrix}\underline{q} \\ \underline{w}\end{Bmatrix} \approx \begin{bmatrix}Q_{qx} & Q_{q\gamma} \\ Q_{wx} & Q_{w\gamma}\end{bmatrix}\begin{Bmatrix}\Delta \underline{x}_{c} \\ \Delta \underline{\gamma}\end{Bmatrix} + \begin{bmatrix}Q_{qd} \\ Q_{wd}\end{bmatrix}\left\{\Delta \underline{d}\right\} \tag{5-6}$$

and move limits, $l_i \le \Delta x_i \le u_i$, where,

$$P_{x} = \frac{\partial P}{\partial \underline{x}_{c}} \; ; \; P_{\gamma} = \frac{\partial P}{\partial \underline{\gamma}} \; ; \; P_{d} = \frac{\partial P}{\partial \underline{d}} \tag{5-7a}$$

$$T_{x} = \frac{\partial T}{\partial \underline{x}_{c}} \; ; \; T_{\gamma} = \frac{\partial T}{\partial \underline{\gamma}} \; ; \; T_{d} = \frac{\partial T}{\partial \underline{d}} \tag{5-7b}$$

$$Q_{qd} = \left[\frac{\partial q_{i}}{\partial d_{j}}\right] \; ; \; Q_{wd} = \left[\frac{\partial w_{i}}{\partial d_{j}}\right] \tag{5-7c}$$

and the entries of submatrices Q_{qx}, $Q_{q\gamma}$, Q_{wx}, and, $Q_{w\gamma}$ are identically the influence coefficients employed in the EHPIC/HERO analysis. Thus the additional computational load involved computation of derivatives w.r.t. to the design and the thrust and power derivatives. The wake constraints ensure that, to a linear approximation, the cross-flow and downwash velocities remain zero under the design perturbations. Eqs. (5-1) were solved using a simplex linear programming routine (Reference 52). The state is then updated using the computed $\Delta \underline{X}$ and the EHPIC/HERO analysis reconverged. The process continues sequentially until no substantial improvement in $J(\underline{X})$ is obtained.

The original SLP algorithm made efficient use of the first order information at hand and proved sufficient in improving the blade twist distribution for power reduction at constant thrust. Nonetheless, certain improvements to the algorithm were desirable. Chief among these were: a more efficient implementation of the upper and lower limit constraints which originally were entered as 2n inequality constraints (n being the order of the state vector, $\underline{X}$); a means of converging to minima that lie off the imposed constraints; improved numerical conditioning of the simplex tableau; and ways of reducing the tableau array size. Hence, an integral task of this effort has been evaluating alternate optimization algorithms and addressing ways to improve the efficiency of the algorithm.

5.1.3 Selection of optimization algorithms for Phase II

As explained above, our examination of optimization algorithms has been limited to those requiring at most first order information. The available techniques may be broadly categorized into constrained and unconstrained minimization methods. The former approach deals with the imposed constraints directly, whereas the latter augments the objective function with a penalty function which basically penalizes violation of the imposed constraints. More stringent constraints can be emphasized by varying the weighting parameters in the penalty function. The transformed problem is then solved using an unconstrained optimization method. Unfortunately, the unconstrained techniques tend to suffer from numerical ill-conditioning related to the penalty function weightings. Furthermore, it is difficult to judge a priori which of the constraints are of greater importance in the problem and how to quantify the weighting terms to appropriately enforce a given constraint. Finally, computational experience in structural optimization problems indicates that such schemes frequently converge much more slowly when compared to the direct methods (References 51, 53).

Therefore, we focused on the constrained optimization methods. The candidates considered were an extension of SLP with move limit reduction near the optimum, the method of feasible directions, and sequential quadratic programming (SQP) (Reference 51). It was decided to implement SQP for the following reasons:

(1) It tends to exhibit superior convergence properties. This is due to the iterative generation of a Hessian matrix, which is essentially a positive definite approximation to $\left.\frac{\partial^2 J}{\partial \underline{X}^2}\right|_{\underline{X}=\underline{X}^*}$. As detailed below, the matrix can be generated using only first order derivatives. Qualitatively, it embodies information from previous steps to estimate the curvature, or second order properties, in the vicinity of the optimum. It is this 'memory' of previous iterations which gives SQP methods an advantage over other techniques (SLP, method of feasible directions) using only the local first order data and which originally engendered a closer look at SQP methods.

(2) The presence of a positive definite quadratic term in the objective function enhances convergence near minima that do not lie on the constraint boundaries. It is well known that the solution to a linear programming problem lies at the intersection of exactly n non-degenerate constraints. Thus, if the true nonlinear minimum does not lie at such an intersection the linear programming solutions will dither between the imposed move limits, l_i and u_i. In practice, the move limits are reduced when proximity to the minimum is detected so that one effectively 'shrinks' the feasible domain down to the optimum design. This procedure is time consuming and is circumvented in SQP methods by virtue of using a quadratic objective function.

(3) The SQP problem is solved by using a modified version of the simplex algorithm. As described below, solving a quadratic programming problem amounts to finding a feasible solution to the Kuhn-Tucker conditions which can be cast as a linear programming problem with additional logical constraints in the selection of variables leaving and entering the active set (i.e. the set of variables that away from its bounds, l_i and u_i.) Thus, the core simplex routines employed by SLP and SQP methods share a strong commonalty and in fact, the same simplex algorithm is used by both methods in the optimization code developed here.

One drawback of the SQP approach is increased array dimension of the simplex tableau. Whereas the tableau for the modified SLP scheme developed here is of order (m by n) where m is the number of imposed constraints, the SQP solution process requires an array of order (m+n by m+2n). Since the number of wake related equality constraints is n, then m=n and the SQP method has six times the memory requirements of the SLP method used to solve the same problem. The number of floating point operations increases accordingly. Furthermore, away from the optimum, the SLP and SQP algorithms tend to advance at the same rate. This is due to the fact that away from the optimum the design change per optimization step is limited primarily by the imposed move limits. The linear approximation to the objective function dominates the quadratic terms and the design changes obtained per iteration tend to be identical using either SLP or SQP. The picture is different in the neighborhood of the minimum where many of the first order derivatives tend to zero, so that the quadratic term in the SQP formulation becomes important and accelerates convergence to the final design. Accordingly, it has been found to be desirable to retain both the SLP and SQP techniques, using SLP initially and then continuing with SQP when proximity to the optimum is ascertained. The similarity of the underlying simplex procedure used in both SLP and SQP solution procedures has thus proven to be a distinct advantage.

In the following sections, the linear programming (LP) and quadratic programming (QP) problems are posed, and the solution to the QP problem stated and its relation to the LP problem established. The construction of quadratic term in the SQP approach is then described and finally some aspects of the common simplex routine detailed.

5.2 Statement of the SLP and SQP Problems

The nonlinear optimization problem posed in Eqs. (5-1) is repeated:

Minimize $J(\underline{X})$ subject to the constraints

$$\begin{aligned} g_j(\underline{X}) &\leq 0 \quad , && j=1,\ldots,m_i \\ g_k(\underline{X}) &= 0 \quad , && k=m_i+1,\ldots,m_e \\ l_i \leq x_i &\leq u_i \quad , && i=1,\ldots,n \end{aligned} \tag{5-8}$$

The solution at iteration step, q, is known, $\underline{X}^q$, and the problem is to determine a change in this solution which results in a reduction in $J(\underline{X})$. In the iteration limit, convergence to a local minimum is expected. The LP problem to be solved each iteration step is:

Minimize, $J(\underline{X}^q) + \nabla J(\underline{X}^q)\,\Delta\underline{X}$ subject to

$$\begin{aligned} & g_j(\underline{X}^q) + \nabla g_j(\underline{X}^q)\,\Delta\underline{X} \leq 0 \quad , && j=1,\ldots,m_i \\ & g_k(\underline{X}^q) + \nabla g_k(\underline{X}^q)\,\Delta\underline{X} = 0 \quad , && k=m_i+1,\ldots,m_e \\ & \Delta l_i \leq \Delta x_i \leq \Delta u_i \quad , && i=1,\ldots,n \end{aligned} \tag{5-9}$$

The upper and lower bounds incorporate move limit requirements:

$$\Delta l_i = \text{Max.} \; \{ -\Delta x_i^{max} \; , \; l_i - x_i^q \} \tag{5-10a}$$

$$\Delta u_i = \text{Min.} \; \{ \Delta x_i^{max} \; , \; u_i - x_i^q \} \tag{5-10b}$$

where Δx_i^{max} is the maximum change in x_i allowed per iteration step. The QP problem is identical to the LP problem except that the objective function is augmented by a quadratic term to:

$$J(\underline{X}^q) + \nabla J(\underline{X}^q)\,\Delta\underline{X} + \frac{1}{2}\Delta\underline{X}^T[B]\,\Delta\underline{X} \tag{5-11}$$

where matrix, [B], is a positive definite approximation to the Hessian of the objective function and local constraints and is generated iteratively from successive evaluations of the first order derivatives as described in Section 5.2.2.

The LP problem at each iteration of the SLP method is solved using the simplex technique described in Appendix A. In the SQP case, the sequence of QP problems is solved finding feasible solutions to the Kuhn-Tucker equations as described below.

5.2.1 Kuhn-Tucker conditions

The solution to the QP problem is stated in terms of the well-known Kuhn-Tucker conditions (Reference 51) as follows. The full nonlinear conditions for an extremum are thereby stated by first defining a Lagrangian,

$$L(\underline{X}) = J(\underline{X}) + \sum_{i}^{n}\mu_{1i}(l_i - X_i) + \sum_{i}^{n}\mu_{2i}(X_i - u_i) + \sum_{i=1}^{mi+me} \lambda_i\, g_i(\underline{X}) \tag{5-12}$$

then in addition the imposed constraints,

$$\nabla L(\underline{X}^*) = \frac{\partial L}{\partial \underline{X}^*} = \underline{0} \tag{5-13a}$$

$$\mu_{1i}^*\left(X_i^* - l_i\right) = 0 \;;\; \mu_{2i}^*\left(u_i - X_i^*\right) = 0 \;;\; \mu_{1i}^*, \mu_{2i}^* \geq 0 \tag{5-13b}$$

$$\lambda_j^*\, g_j\left(\underline{X}^*\right) = 0 \;;\; \lambda_j^* \geq 0 \quad (j=1,\ldots,m_i) \tag{5-13c}$$

$$\lambda_k^* \quad \text{unbounded} \quad (k=m_i+1,\ldots,m_i+m_e) \tag{5-13d}$$

where the superscript, $(\bullet)^*$, denotes evaluation at the optimum point. The new parameters, $\underline{\mu}_1$, $\underline{\mu}_2$ and, $\underline{\lambda}$ are Lagrange multipliers that correspond to the lower and upper bound constraints and the imposed constraint equations respectively. The first of these equations define an extremum while the remaining conditions restrict the allowable values for the Lagrange multipliers. Specifically, for inequality constraints, the associated Lagrange multiplier can only be non-zero if the constraint is active. This implicitly states that when a given inequality constraint is active then the gradients of the cost function and constraint point in opposite directions so that the design cannot be further improved without violating the local constraints.

For the SQP problem posed in terms of design perturbations, in addition to satisfying the imposed constraints, the optimum $\Delta\underline{X}$ satisfies:

$$\nabla J(\underline{X}^q) + [B]\Delta\underline{X} - \underline{\mu}_1 + \underline{\mu}_2 + \sum_{i=1}^{mi+me} \lambda_i \nabla g_i(\underline{X}^q) = \underline{0} \quad (5\text{-}14a)$$

with

$$\mu_{1i}(\Delta x_i - \Delta l_i) = 0 \; ; \; \mu_{2i}(\Delta u_i - \Delta x_i) = 0 \; ; \; \mu_{1i}, \mu_{2i} \geq 0 \quad (i=1,\ldots,n) \quad (5\text{-}14b)$$

$$\lambda_j \left[g_j(\underline{X}^q) + \nabla g_j(\underline{X}^q)\Delta\underline{X} \right] = 0 \; ; \; \lambda_j \geq 0 \quad (j=1,\ldots,m_i) \quad (5\text{-}14c)$$

$$\lambda_k \text{ unbounded} \quad (k=m_i+1,\ldots,m_e) \quad (5\text{-}14d)$$

In the above, the first n equations are merely linear equality constraints which are directly accommodated in the simplex formulation. Likewise, the positivity requirements upon the components of μ_1, μ_2 and, λ_j are naturally dealt with in the LP framework. The imposed linearized constraints, g_i, are of course already handled by the simplex algorithm. Therefore, the only modifications required to solve the QP problem utilizing the simplex algorithm are those related to the *nonlinear* constraints in Eqs. (5-14b,c). Fortunately, these conditions can be implemented entirely by logical restrictions upon the variables allowed to enter and leave the basic set during a pivot operation. Specifically, in the simplex formulation the inequality constraints, are converted to equality constraints by the use of slack variables, s_j:

$$g_j(\underline{X}^q) + \nabla g_j(\underline{X}^q)\Delta\underline{X} \leq 0 \quad (5\text{-}15a)$$

$$g_j(\underline{X}^q) + \nabla g_j(\underline{X}^q)\Delta\underline{X} - s_j = 0 \; , \; s_j \geq 0 \quad (5\text{-}15b)$$

Thus the related Lagrange variable, λ_j, can only enter the basic set if s_j is at its bound, $s_j=0$, implying that the corresponding constraint is active. Equivalently, only one of s_j and λ_j can be in the basic set at a given time. Since membership of a given variable in the basic set is a logical attribute, the nonlinear constraints embodied in the Kuhn-Tucker conditions are implemented simply by conducting a series of membership tests upon the candidate pivot elements.

The problem solved by the QP algorithm is an approximation to the original nonlinear optimization task posed in Eqs. (5-8). Thus in the spirit of iterative methods for solving nonlinear problems by local linearization, the solution, $\Delta\underline{X}$, obtained is used to update the current design, the functional and constraints and their first order derivatives re-evaluated about the new state, and a new QP problem formulated about that point. Although it is difficult to derive conditions for convergence in the general case, the sequential process is expected to converge to the nonlinear optimum, especially if the functional is convex in the vicinity of the optimum.

An extension to the SQP procedure described is to employ the state vector update, $\Delta\underline{X}$, as a search direction and perform a 1-D minimization or equivalently determining an optimal step length along this direction. The theoretical advantages of conducting a 1-D search along the optimal direction include more accurate update of the Hessian matrix approximation. Also, theoretical proofs of superlinear convergence of the SQP scheme assume that 1-D optimization is executed. Unfortunately, at least two additional functional evaluations (calls to EHPIC/HERO), are necessary to determine an approximate 1-D minimum using a quadratic polynomial fit. This cost was found to be unnecessarily expensive since the rate of convergence to an optimum was not significantly improved. We believe this to be due to violation of constraints that can occur when the optimal step length differs from unity. It was also observed that the 1-D functional which is constructed from the cost function and active constraints is sensitive to round-off error and constraint violation and occasionally leads to unreasonable step lengths which must be limited. Furthermore, as noted earlier, when the design change is limited primarily by the imposed move-limits, the progression of the solution toward the optimum is fairly constant whether employing SLP, SQP or SQP with 1-D minimization. Hence, the SQP algorithm employed here is executed using unity step length.

5.2.2 Hessian matrix update formula

The Hessian matrix approximation, B, is updated at each optimization step, q, according to the Broydon-Fletcher-Shanno-Goldfarb update formula (References 51, 54, 55). Given the current approximation, B^q, the updating proceeds as follows: First rescale B^q as,

$$B^* = \kappa B^q \quad , \quad \kappa = \frac{p^T w^q}{p^T B^q p} \tag{5-16}$$

then update,

$$B^{q+1} = B^* - \frac{B^* p\, p^T B^*}{p^T B^* p} + \frac{r\, r^T}{p^T r} \tag{5-17a}$$

where,

$$p \equiv \underline{X}^q - \underline{X}^{q-1} = \Delta \underline{X}^{q-1} \tag{5-17b}$$

$$r \equiv \Theta w^q + (1-\Theta) B^* p \tag{5-17c}$$

$$w^q = \nabla_X L\left(\underline{X}^q, \underline{\lambda}^{q-1}\right) - \nabla_X L\left(\underline{X}^{q-1}, \underline{\lambda}^{q-1}\right) \tag{5-17d}$$

$$L = J(\underline{X}) + \sum_{i \in I_h} \lambda_i\, g_i(\underline{X}) \tag{5-17e}$$

and

$$\Theta = \begin{cases} 1 & \text{if } \; p^T r \geq 0.2 p^T B^* p \\ \dfrac{0.8\, p^T B^* p}{p^T B^* p - p^T r} & \text{if } \; p^T r < 0.2 p^T B^* p \end{cases} \tag{5-17f}$$

Here, I_h is the set of holonomic constraints as explained in the next sub-section. The matrix, B^q, is first scaled by the factor κ as recommended by Luenberger (Reference 56). For a quadratic programming problem where the true Hessian of the Lagrangian function at the optimum is H, then defining κ in this manner guarantees that the range of eigenvalues of BH^{-1} spans unity at each iteration. Furthermore, the condition number of (BH^{-1}) will be non-decreasing which is desirable from a numerical standpoint. In theory, the specification of q above ensures that if B is initially positive definite then it remains so after the updating procedure. However, this is not necessarily true in the presence of round-off error. Specifically, the last term in Eq. (5-17a) is always positive semi-definite. However, numerical differencing between the first two terms can introduce sufficient error to render B^{q+1} non-positive definite. Hence, the expression is modified slightly by adding small positive terms to the diagonal elements of B:

$$B^{q+1} \leftarrow B^{q+1} + \frac{0.01}{p^T B^* p}\left[\mathrm{diag}\left\{y_i^2\right\}\right] \quad , \quad y = B^* p \tag{5-18}$$

The entries of this additive diagonal matrix are identical to the diagonal components of the second term on the R.H.S. of Eq. (5-17a) scaled by a factor of 0.01. The manner in which information of the cost function and constraint derivatives from preceding optimization steps is implicitly incorporated into B^q is apparent from the definition of w^q. During the course of the optimization, round-off error and higher order contributions from the constraints and cost function derivatives are also accumulated in B. Thus, periodic resetting of the B to a scaled identity matrix is recommended and is done in the code every 2n-2 optimization steps (resetting B every n steps can occasionally slow convergence) and also when convergence to the optimum is detected.

The preceding construct for the matrix B guarantees that the generated matrices B^q remain positive definite throughout the optimization provided that the initial matrix, $B^0 > 0$. This is true regardless of whether the true nonlinear cost function, J, contains maxima or saddle points. Under certain assumptions on the convexity of the objective function and constraints (References 54, 55) it is proven that superlinear convergence results when using this update formula. The sequence, B^q, need not converge to the actual Hessian of the Lagrangian at the solution. Instead, the projection of B^q unto the tangent vector space generated by the linearized acting constraints converges to the corresponding projection of the true Hessian. Or symbolically, if the optimum solution is denoted by ($\underline{X}^*, \underline{\mu}^*, \underline{\lambda}^*$) then

$$\lim_{q \to \infty} Z^T\left[\nabla_{XX} L\left(\underline{X}^*, \underline{\mu}^*, \underline{\lambda}^*\right) - B^q\right] Z = 0 \tag{5-19}$$

where, the Lagrangian is defined in Eq. (5-12), and Z is any vector lying in the space generated by the *active* constraints:

$$\nabla \underline{g}_j(\underline{X}) \ , \ j \in j_A \quad \text{and} \quad \nabla \underline{g}_k(\underline{X}) \ , \ k = 1, \ldots, m_e \tag{5-20}$$

where the set of active inequality constraints, $j_A = \{j: \ g_j = 0 \ , \ j = 1, \ldots, m_i\}$.

5.2.3 Distinction between holonomic and non-holonomic constraints

The set of constraints, I_h, appearing in the summation of the constraints in Eq. (5-17e), is the subset of the complete set of constraints that are holonomic. The update formula for B^q assumes constraints of the form Eq. (5-8) which are functions of state, $\underline{X}$, and possibly other parameters which are fixed during the optimization process. These constraints may be thought of as global constraints in that they form well defined and fixed hypersurfaces in the state space. Constraints may also be stated in differential form which in the present context implies that the constraints are expressed in the form, $dg_j(\underline{X}, \Delta\underline{X}) \leq 0$ or $dg_k(\underline{X}, \Delta\underline{X}) = 0$ which may be regarded as local constraints imposed at a given optimization step but which may change between steps. When such constraints are integrable so that they can be expressed in the form $g_j(\underline{X}) \leq 0$ and $g_k(\underline{X}) = 0$ respectively then they are termed holonomic. When no such integrated form exists, they are classified as non-holonomic.

Examples of holonomic constraints applied to the hover optimization task include the specified upper and lower bounds on $\underline{X}$, limits on the nodal twist, or equality and inequality constraints on power and/or thrust. Examples of non-holonomic constraints include move-limit constraints, *changes* in nodal twist, and, most significantly here, the equality constraints derived from the wake analysis. The wake equations are expressed in terms of the changes in collocation point positions, $\Delta\underline{x}_c$ and bound circulations, $\Delta\underline{\gamma}$. These perturbations are determined in the optimization analysis and used to update $\underline{x}_c$ and $\underline{\gamma}$. However, during the subsequent EHPIC/HERO analysis where the wake is re-converged, $\underline{x}_c$ and $\underline{\gamma}$ will generally change. i.e., the values of $\underline{x}_c$ and $\underline{\gamma}$ differ between calls to the optimization process with the discrepancy being due to nonlinearities. Therefore, these constraints are not included in the update formulas. Similarly, the move limit related inequality constraints are not used for the Hessian matrix update. However, when the solution is sufficiently close to a 'hard' bound (upper or lower limit imposed on the variable) so that it forms one of the boundaries of the feasible region then the associated inequality constraint now is used in the update equation for B^q. Naturally, all of the constraints must be retained in the SQP optimization in order to define the feasible region.

5.2.4 Extensions to SLP

The SLP algorithm utilizes the same simplex subroutines as the SQP scheme. Beyond the modifications made to the simplex algorithm itself, the chief modification that has been made from the Phase I algorithm is additional logic for the sizing of the move limit, Δx_i^{max}, associated with each x_i. The rationale is to retain constant size move limits as long as the design point is heading towards the optimum. If the optimum solution is fully constrained (i.e. lies at the intersection of a total of n linearly independent constraints) all is well since the LP solution will then coincide with the actual nonlinear solution. In general however, the optimum solution may not be fully constrained and when one is sufficiently near the optimum such that the optimal design point lies within the feasible region, the sequence of points obtained via SLP from there on oscillates about the optimum essentially bouncing between the move limits defined for the design variables. Thus one has obtained the optimum solution only to within the resolution defined by the Δx_i^{max} and to increase the accuracy of this solution the Δx_i^{max} must then be reduced. This is easily done if one is able to ascertain when the optimum lies within the feasible region surrounding the current design point. This is accomplished by keeping track of the design changes. Specifically, the two most recent design points are stored and if all of the design variables are observed to remain within the region defined by $\underline{X} \pm \Delta\underline{X}^{max}$ then the move limits are reduced. i.e., if $\left| x_i^q - x_i^{q-2} \right| < \Delta x_i^{max}$, $\forall i$, then set $\Delta x_i^{max} \leftarrow 0.55\ \Delta x_i^{max}$.

5.3 Application to Rotor Design Optimization

The implementation of the sequential optimization techniques outlined above, amounts to specifying a design vector, $\underline{d}$, together with the desired cost function, J, constraints, g_i, and their derivatives as input to the optimization algorithm. The design vector, $\underline{d}$, is determined by the user in the optimization input file and consist of the parameters that specify the undeformed blade geometry. These presently include sweep distribution, twist distribution, anhedral distribution, chord distribution, and collective. The coding for blade radius and cutout optimization is also in place but their use as design parameters is not recommended at present. The equations used in the EHPIC/HERO wake analysis form a set of equality constraints in the optimization analysis. In many cases, the equality constraints associated with the wake equations can be solved directly to eliminate some of the variables thereby greatly reducing the dimensions of the optimization tableau. These topics together with the objective functions and constraints that may be applied are examined in the following sections.

5.3.1 Description of available objective functions

The user is offered a selection of objective functions to be minimized. In the present version these are restricted to thrust, induced power, profile power, or combinations of these. Objective functions associated with structural properties can also be formulated to minimize maximum stresses or deflections. However, structural optimization has not been included as an option for several reasons. First, the focus of this effort has been upon the aerodynamic aspects of the hover problem and the purpose of including a structural modeling capability is to improve hover prediction for real rotors. To that end, a structural model that predicts the blade deflections with an accuracy that is consistent with the amount of detail contained in the geometry specifications, is adequate. Hence, for example, the number of finite elements is commensurate with the number of blade segments. This also allows a concise structural specification file where the major blade stiffness and mass properties are characterized in terms of area integrals. Finally, the model can be constructed very efficiently which is advantageous when determining the design related derivatives in the optimization analysis since the stiffness matrix and nodal forces must be recomputed for each design perturbation in order to account for deformation effects (see Chapter 4). Second, it is judged that a serious approach to the task of structural optimization requires a more detailed structural model in order to obtain accurate estimates of the blade stresses. This requires specification of skin thickness, and other localized geometry information rather than the integrated cross-section parameters used in EHPIC/HERO. Finally, the structural optimization task is constrained by other considerations not directly relevant to the hover problem. Notably, the modal frequencies and blade dynamic response in forward flight are expected to be more significant in guiding structural optimization.

Therefore, we have sought to furnish a series of objective functions which represent integrated aerodynamic performance parameters deemed to be of most interest to potential users. At present the fundamental parameters are the thrust, T, induced power, P_i, and profile power, P_p. The user selects the objective function by specifying the input parameter KOBJ(1) as follows (see Reference 12):

KOBJ(1)	Operation Performed
1, 11	Minimize Total Power, $P_T = P_p + P_i$
2, 12	Maximize Thrust, T

3	Maximize Figure of Merit, $\sqrt{2}\,C_T^{3/2}\,/\,2C_Q$.
4	Maximize Propulsive Efficiency, C_T/C_Q.
20	Multi-objective minimization of both thrust and total power
30	Multi-objective optimization of combination of thrust and induced and profile power contributions.

where $C_T=T/(\rho\pi\Omega^2R^4)$ and $C_Q=(P_i+P_p)/(\rho\pi\Omega^2R^5)$. The cost function combinations for KOBJ(1)≥20 are specified below. It suffices here to note that these involve combinations of T, P_i, and P_p. Then it follows that all options for KOBJ(1) are constructed from one or more of the functions, T, P_i, and P_p, which must be supplied in the EHPIC/HERO analysis along with the first order derivatives which are calculated by finite differencing.

Except for options KOBJ(1)=3,4, the objective functions appear to exhibit weak curvature so that the design tends to progress indefinitely along a path of steepest descent. This is similar to the problem encountered in linear programming procedures where the objective function is linear and unless suitably constrained, can return optimal designs with infinite values. It is clear, for example in a power optimization calculation, that unless a lower bound upon thrust is imposed, the design will move in a direction that reduced thrust along with the power leading to zero or negative thrust levels. To properly pose the optimizations, each option of KOBJ(1) also implicitly adds constraints:

KOBJ(1)	Applied Constraint(s)
1	$T = T_{spec}$
2	$P_T = (P_T)_{spec}$
3,4	None
11	$T \geq T_{spec}$
12	$P_T \leq (P_T)_{spec}$
20	$T \geq T_{spec}$ and $P_T \leq (P_T)_{spec}$
30	$T \geq T_{spec}$, $P_i \leq (P_i)_{spec}$, and $P_p \leq (P_p)_{spec}$

where $(\bullet)_{spec}$ is a specified level (default levels correspond to the initial design).

5.3.2 Choice of multi-objective functions

A multi-objective design task is generally approached by constructing a global objective function from the single objective criteria. The simplest form is simply a linear combination of the constituent cost functions and utilize this as the cost function, J, in the same optimization procedure employed in the single objective case. A preferable approach is to combine the single objective functions in a possibly nonlinear fashion so that the resulting global cost function represents a physically meaningful entity. Examples of this are the options KOBJ(1)=3, 4 where the thrust and power are combined nonlinearly to form the figure of merit and propulsive efficiency. Often, however, such convenient combinations are not obvious, particularly in multi-disciplinary optimization. Therefore, unless or until global optimization cost parameters are available, the linear combination of single objective functions is arguably most useful due to ease of implementation and tractability, and since sensitivity analyses which help gauge relative trade-offs between the various constituent cost can be straightforwardly conducted for this combination.

If the single objective cost functions are denoted by J_i then the composite cost function,

$$J_G = \sum_i w_i J_i \tag{5-21}$$

where the w_i are weighting parameters that are intended to reflect the degree of importance attached to minimizing the constituent, J_i. The specific forms for the multi-objective options of KOBJ(1) are:

KOBJ(1)=20:

$$J_G = w_1 \frac{T_{max} - T}{T_{max} - T_{min}} + w_2 \frac{P_T - (P_T)_{min}}{(P_T)_{max} - (P_T)_{min}} \tag{5-22}$$

KOBJ(1)=30:

$$J_G = w_1 \frac{T_{max} - T}{T_{max} - T_{min}} + w_2 \frac{P_i - (P_i)_{min}}{(P_i)_{max} - (P_i)_{min}} + w_3 \frac{P_p - (P_p)_{min}}{(P_p)_{max} - (P_p)_{min}} \tag{5-23}$$

where T= thrust, P_T=total power, P_i=induced power and P_p=profile power. The $(\bullet)_{min}$ and $(\bullet)_{max}$ values are either specified by the user or set to default values in EHPIC/HERO. Their purpose is to scale the dimensional quantities so that the J_i have roughly equal influence upon the overall J_G. Ideally, if the w_i were all equal, then the J_i would also be equal in the globally optimal design. In practice best guesses to these ranges are usually made. One alternative (Reference 57) is to perform the single objective function minimizations separately. For each design thus obtained, $\underline{d}_k$ say, EHPIC/HERO may be used to evaluate $T(\underline{d}_k)$, $P_i(\underline{d}_k)$, and $P_p(\underline{d}_k)$. Then $T_{max} = \max_k\{T(\underline{d}_k)\}$, and similarly for T_{min}, $(P_i)_{max}$ etc.

An important consideration is the selection of the w_i. This is a non-trivial task with the goal of choosing values for w_i that leads to an overall qualitatively 'best' design. It often happens that one of the J_i dominates and the optimal design is similar to the corresponding single objective case. A more serious effect is that usually some of the J_i are 'sacrificed' in order to allow decrease in some other J_i so that a net decrease in J_G is attained. Problems arise if the change in the numerical magnitude of J_i is small in comparison to the other J_i, but that this change represents an unacceptable increase of that cost. Essentially, this reiterates the desirability of a global cost function which is derived from physical considerations (e.g. figure of merit; propulsive efficiency) since it is otherwise not clear what J_G is intended to represent. Hence it is assumed that this issue has been carefully considered by the user who is required to specify the w_i in the input file.

One additional safeguard is supplied however which prevents the individual costs from exceeding specified upper bounds. Thus the following inequality constraints are enforced for,

KOBJ(1)=20:

$$J_1 = \frac{T_{max} - T}{T_{max} - T_{min}} \leq 1 \qquad J_2 = \frac{P_T - (P_T)_{min}}{(P_T)_{max} - (P_T)_{min}} \leq 1 \tag{5-24}$$

KOBJ(1)=30:

$$J_1 = \frac{T_{max} - T}{T_{max} - T_{min}} \leq 1 \qquad J_2 = \frac{P_i - (P_i)_{min}}{(P_i)_{max} - (P_i)_{min}} \leq 1$$

$$J_3 = \frac{P_p - (P_p)_{min}}{(P_p)_{max} - (P_p)_{min}} \leq 1 \tag{5-25}$$

In fuzzy optimization terminology, the J_i may now be regarded as membership functions. The combination of the normalization terms and the limiting effected in the preceding equations implies that the $J_i \in [0,1]$. It is assumed here that by suitable choice of $(\cdot)_{max}$ and $(\cdot)_{min}$ the individual $J_i \geq 0$. Thus the individual cost functions are placed on an equal footing with the other imposed constraints. This guards against the 'sacrifice' behavior mentioned above and tends to produce qualitatively better designs that give overall improvement in at least some of the J_i while ensuring that the others do not become unacceptably large.

5.3.3 Incorporation of the wake constraints

The equality constraints upon linearized normal/binormal velocities and the blade quadrilateral downwash velocities are directly available from the EHPIC/HERO analysis and are expressed as,

$$\begin{Bmatrix} \Delta \underline{q} \\ \Delta \underline{w} \end{Bmatrix} = \begin{Bmatrix} \underline{0} \\ \underline{0} \end{Bmatrix} = \begin{bmatrix} Q_{qx} & Q_{q\gamma} & Q_{qd} \\ Q_{wx} & Q_{w\gamma} & Q_{wd} \end{bmatrix} \begin{Bmatrix} \Delta \underline{x}_c \\ \Delta \underline{\gamma} \\ \Delta \underline{d} \end{Bmatrix} \tag{5-26}$$

These constraints play two roles in the optimization analysis. First, when enforced, they guarantee that to within a linear approximation, the post-optimization design maintains zero downwash and collocation cross-velocities as required for the converged wake solution. In practice, the inherent nonlinearities require that the wake solution be reconverged and the post optimization design solution provides a very good first guess to the converged state. Second, these constraints serve to linearly couple the design perturbation with the wake changes so that the total influence of a given design variable upon the constraints and cost is accounted for. In EHPIC/HERO, the design related influence coefficients are effectively partial derivatives with the collocation points and blade circulations held fixed. Thus, for example, the thrust coefficient, T_d, for design variable, d_i, is computed by perturbing the blade geometry corresponding to d_i and then forming the finite difference of the thrust. Thus,

$$T_d = \left.\frac{\partial T}{\partial \underline{d}}\right| (\underline{x}_c, \underline{\gamma}\,\text{fixed}) \tag{5-27}$$

To determine the physical change in thrust that occurs when $\underline{d}$ is perturbed, the total derivative must be evaluated implying that the changes in the wake, $\Delta\underline{x}_c$, and bound circulations, $\Delta\underline{\gamma}$, must be taken into account. Thus,

$$\frac{dT}{d\underline{d}} = \frac{\partial T}{\partial \underline{x}_c}\Delta\underline{x}_c + \frac{\partial T}{\partial \underline{\gamma}}\Delta\underline{\gamma} + \frac{\partial T}{\partial \underline{d}}\Delta\underline{d} \tag{5-28a}$$

or,

$$\frac{dT}{d\underline{d}} = T_x\,\Delta\underline{x}_c + T\gamma\Delta\underline{\gamma} + T_d\,\Delta\underline{d} \tag{5-28b}$$

The wake constraints can now be used to solve for the wake position and bound circulation perturbations that take place for perturbation $\Delta\underline{d}$:

$$\begin{Bmatrix} \Delta\underline{x} \\ \Delta\underline{\gamma} \end{Bmatrix} = -\begin{bmatrix} Q_{qx} & Q_{q\gamma} \\ Q_{wx} & Q_{w\gamma} \end{bmatrix}^{-1} \begin{bmatrix} Q_{qd} \\ Q_{wd} \end{bmatrix} \Delta\underline{d} \tag{5-29}$$

so that the physical thrust change due to $\Delta\underline{d}$ is,

$$\Delta T = \left(T_d - \begin{Bmatrix} T_x & T_\gamma \end{Bmatrix} \begin{bmatrix} Q_{qx} & Q_{q\gamma} \\ Q_{wx} & Q_{w\gamma} \end{bmatrix}^{-1} \begin{Bmatrix} Q_{qd} \\ Q_{wd} \end{Bmatrix} \right) \Delta\underline{d} \tag{5-30}$$

This is extremely important since in general the second term in (•) of the preceding expression dominates implying that the chief contributions are due to the related wake and bound circulation changes. In fact, it is the matrix partition, Q_{wg}, which accounts for most of the contribution to ΔT. This has been observed to be generally true of aerodynamic parameters other than thrust (e.g., power).

The set of linear equality constraints, Eq. (5-26), can either be entered into the optimization analysis directly in forming the constraint set, g, or else used to eliminate the variables $\Delta\underline{x}_c$ and $\Delta\underline{\gamma}$ via Eq. (5-29) in a pre-processing step prior to the optimization routine. The advantage of the latter approach is a drastic reduction in the dimension of the simplex tableau since when Eq. (5-26) is entered directly in the optimization routine, it consumes most of the tableau. The drawback is that move limits can no longer be imposed upon $\Delta\underline{x}_c$ and $\Delta\underline{\gamma}$ and so the move limits imposed upon the design variables may need to be reduced to ensure that the subsequent wake analysis reconverges. Reduced move limits imply slower progress toward the final design.

The EHPIC/HERO optimization parameter, KOPT, allows the use to select between these options:

KOPT=1 -	Use the full wake equations to define equality constraints in the optimization routine;
KOPT=2 -	Use the full wake equations to eliminate $\Delta\underline{x}_c$ and $\Delta\underline{\gamma}$ and update the design variable related influence coefficients (e.g., T_d, etc.)
KOPT=3 -	Same as KOPT=1 except that only the downwash equations are retained and Q_{wx} is assumed zero. Thus the constraints corresponding to the wake analysis reduce to:

$$\underline{0} = \begin{bmatrix} Q_{w\gamma} & Q_{wd} \end{bmatrix} \begin{Bmatrix} \Delta\underline{\gamma} \\ \Delta\underline{d} \end{Bmatrix}$$

KOPT=4 - Use the reduced equations of KOPT=3 to solve for $\Delta\underline{\gamma}$. Then,

$$\Delta\underline{x}_c = \underline{0}$$

and $$\Delta\underline{\gamma} = -[Q_{w\gamma}]^{-1}[Q_{wd}]\,\Delta\underline{d}$$

The particular option to use will depend on the specific blade configuration and wake analysis used. Increasing KOPT results in fewer computations but tends to be less robust, particularly for analysis involving a large number of wake points.

5.3.4 Incorporation of structural deformations

The constraints equations, Eqs. (5-26), and the objective function definitions assume that those influence coefficients identified with the design perturbations, $\Delta\underline{d}$, take into account any structural deformation effects. When structural deformation is present, one distinguishes between the undeformed geometry which is defined by the design variables, and the deformed geometry used in the wake analysis. This is most important when determining the various derivatives with respect to the design variables (e.g., Q_{wd}, T_d, etc.) by the finite differencing technique. If we denote here by $\underline{d}_0$ any variable used to specify the undeformed geometry and by $\underline{d}_s$, its value in the deformed case, then is it not generally true that perturbing d_0 leads to an identical perturbation in $\underline{d}_s$. i.e., in general, $\Delta\underline{d}_0 \neq \Delta\underline{d}_s$ due to change and reorientation of the deformation vector. Furthermore, a perturbation in a single component of $\underline{d}_0$ alters the deformed geometry of the complete blade. Take, for example, the undeformed sweep of a given segment iseg, UNDSWP(iseg). Perturbing UNDSWP will reorient the force due to blade rotation, alter the stiffness matrix which has major contributions from rotational stiffening, and consequently change the deformation state and the deformed geometry for the whole blade. Note also, that even if the actual aerodynamic loading were to remain constant the reorientation of the blade results in a different nodal force vector and hence deformation state. The difference, $\Delta\underline{d}_0 - \Delta\underline{d}_s$, naturally depends upon the material blade stiffness. However, this difference can lead to significant changes in some of the derivatives w.r.t. to design, $(\bullet)_d$. This is especially true of the twist gradient, where the tip twist change can be twice that due to the rigid body perturbation alone for typical blades, thus causing readjustments in these $(\bullet)_d$ on the same order as $(\bullet)_d$ itself. This corresponds to the classical theory of torsional divergence in aeroelasticity.

In principle, the state vector can be expanded to include changes in the deformation state, so that the equality constraints are augmented to:

$$\begin{Bmatrix} \Delta\underline{q} \\ \Delta\underline{w} \\ \Delta\underline{f} \end{Bmatrix} = \begin{Bmatrix} \underline{0} \\ \underline{0} \\ \underline{0} \end{Bmatrix} = \begin{bmatrix} Q_{qx} & Q_{q\gamma} & Q_{qs} & Q_{qd} \\ Q_{wx} & Q_{w\gamma} & Q_{ws} & Q_{wd} \\ Q_{fx} & Q_{f\gamma} & K & Q_{fd} \end{bmatrix} \begin{Bmatrix} \Delta\underline{x}_c \\ \Delta\underline{\gamma} \\ \Delta\underline{s} \\ \Delta\underline{d} \end{Bmatrix} \qquad (5\text{-}31)$$

Here, the residual $\Delta\underline{f} = \underline{f} - K\underline{s}$, and the new influence matrix partitions, Q_{qs}, Q_{ws}, Q_{fx}, $Q_{f\gamma}$, and Q_{fd} represent the change in the quantity corresponding to the first subscript due to perturbations in the state associated with the second. This approach was originally implemented during this effort. However, as mentioned in Section 4.6, the calculation of the new influence matrix partitions is rather lengthy and cumbersome and was eventually dropped in favor of the approach below.

Rather than conduct a linearized analysis involving the structural deformation changes, it proves far more efficient to perturb the undeformed design component, recompute the structural properties and loading, update the deformed geometry, and then calculate the various aerodynamic derivatives (Q_{qd}, T_d, etc.) based upon this geometry. The computation required to conduct the complete structural analysis and update the deformed geometry is a small fraction of that entailed in computing the wake related influence coefficients. Thus, in essence we define:

$$(\bullet)_{\underline{d}} = \left(\frac{\partial(\bullet)}{\partial \underline{d}} \right)_{\underline{x}_c, \underline{\gamma}} \tag{5-32}$$

so that $\underline{x}_c$ and $\underline{\gamma}$ are held constant, but $\underline{s}$ is allowed to vary. Fortunately, this is a situation where the actual nonlinear analysis proves more efficient than the linear approximation without loss of robustness in the computation.

In order to calculate the new deformation, the aerodynamic loading must be known, but this is not available until the deformed geometry is available. In theory, a time consuming series of sub-iterations is required where the deformation and loading are updated until convergence is attained. In the present implementation, the deformation is computed only once for a given design perturbation using the aerodynamic forces of the unperturbed design. This is justified in light of the fact that most of the change in structural deformation will be due to reorientation of the segment axes and corresponding changes in the local to global transformations matrices used in obtaining the stiffness matrix and nodal forces. Furthermore, this is consistent with the linear approximations used elsewhere in deriving the first order derivatives.

5.3.5 Twist constraints

The dominant design variable in most optimization computations is the twist gradient, TWG(iseg), over each segment, iseg. The total twist at the outboard end of iseg,

$$\mathrm{TWR}(\mathrm{iseg}+1) = \sum_{\mathrm{jseg}=1}^{\mathrm{iseg}} \mathrm{TWG}(\mathrm{jseg}) * \mathrm{SL}(\mathrm{jseg}) \tag{5-33}$$

where SL(jseg) is the segment length. Since TWR is an accumulative function of the TWG variables lying inboard it is possible that excessive changes in TWR occur, particularly as one approaches the tip, rendering the linearization assumption invalid, or destabilizing the subsequent wake analysis. In order to prevent such changes inequality constraints are adjoined to the optimization analysis limiting the twist change according to:

$$\Delta\mathrm{TWR}(\mathrm{iseg}+1) = \sum_{\mathrm{jseg} \in I_d}^{\mathrm{iseg}} \Delta\mathrm{TWG}(\mathrm{jseg}) * \mathrm{SL}(\mathrm{jseg}) \le 0.3^\circ \tag{5-34a}$$

$$\Delta \mathrm{TWR}(\mathrm{iseg}+1) = \sum_{\mathrm{jseg} \in I_d}^{\mathrm{iseg}} \Delta \mathrm{TWG}(\mathrm{jseg}) * \mathrm{SL}(\mathrm{jseg}) \geq -0.3^\circ \qquad (5\text{-}34b)$$

where iseg ranges from 1,...,nseg and belongs the set of segments, $I_d = \{\mathrm{iseg}: \mathrm{TWG}(\mathrm{iseg}) \in d_i\}$. i.e., if some of the TWG variables are held fixed, such as when only the outboard segments are allowed to vary in the analysis, then those fixed variables are skipped in the above summations.

5.3.6 User supplied constraints

Preliminary coding designed to incorporated user defined constraints has been developed (but not yet tested). It takes the form of a subroutine which allows the user to define inequality constraints and equality constraints as functions of the design variables, d_i. The intended goal is to permit the incorporation of constraints derived via external analyses such as other forward flight studies or structural dynamics considerations. It is assumed that the functional dependence of these constraints upon the d_i can at least be approximated, say by polynomial curve fitting, so that the constraints and their first derivatives can be defined based upon the information supplied to the subroutine. In principle, cost functions could also be user defined and used to augment one of the KOBJ(1) options. Instead, the anticipated manner of incorporating alternative cost functions will be limited to constructing inequality constraints such as those in Eqs. (5-24) and (5-25). This follows from an assumption that accurate evaluation of these external cost functions is better accomplished using independent models, but that their inclusion in a EHPIC/HERO optimization might be desirable to prevent designs yielding unacceptable values for these cost functions.

5.3.7 Summary of optimization formulation

The general optimization problem that may be formulated within EHPIC/HERO is summarized:

$$\text{Minimize} \left\{ \text{Cost} = J + J_x \Delta \underline{x} + J_\gamma \Delta \underline{\gamma} + J_d \Delta \underline{d} \right\}$$

subject to:

$$\underline{0} \geq \underline{g}_i + Q_{ix} \Delta \underline{x} + Q_{i\gamma} \Delta \underline{\gamma} + Q_{id} \Delta \underline{d}$$

$$\left\{ \begin{array}{c} \Delta \underline{q} \\ \Delta \underline{w} \\ \left\{ \underline{g}_e \right\}_{\mathrm{spec}} - \underline{g}_e \end{array} \right\} = \left\{ \begin{array}{c} \underline{0} \\ \underline{0} \\ \underline{0} \end{array} \right\} = \begin{bmatrix} Q_{qx} & Q_{q\gamma} & Q_{qd} \\ Q_{wx} & Q_{w\gamma} & Q_{wd} \\ Q_{ex} & Q_{e\gamma} & Q_{ed} \end{bmatrix} \left\{ \begin{array}{c} \Delta \underline{x}_c \\ \Delta \underline{\gamma} \\ \Delta \underline{d} \end{array} \right\}$$

$$l_i \leq x_i \leq u_i\,, \qquad i=1,\ldots,n \qquad (5\text{-}35)$$

The subscripts $(\bullet)_i$ and $(\bullet)_e$ refer to inequality constraints and equality constraints (beyond those associated with the wake) respectively. These include constraints upon the twist, Eq. (5-34), and any constraints input by the user.

If the user sets KOPT≥3, then one solves for $\{\Delta\underline{x}_c\ \Delta\underline{\gamma}\}$:

$$\begin{Bmatrix}\Delta\underline{x}\\ \Delta\underline{\gamma}\end{Bmatrix} = -\begin{bmatrix}Q_{qx} & Q_{q\gamma}\\ Q_{wx} & Q_{w\gamma}\end{bmatrix}^{-1}\begin{bmatrix}Q_{qd}\\ Q_{wd}\end{bmatrix}\Delta\underline{d} \tag{5-36}$$

using Gaussian elimination. The optimization task is transformed by substituting $\{\Delta\underline{x}_c\ \Delta\underline{\gamma}\}$ back into the remaining equations:

$$\text{Minimize } \{\ \text{Cost} = J + J_d^{*}\ \Delta\underline{d}\}$$

subject to:

$$\begin{gathered}\underline{0} \geq Q_i + Q_{id}^{*}\ \Delta\underline{d}\\ \begin{Bmatrix}(\underline{g}_e)_{spec} - \underline{g}_e\\ T_{spec} - T\end{Bmatrix} = \begin{Bmatrix}\underline{0}\\ 0\end{Bmatrix} = \begin{bmatrix}Q_{ed}^{*}\\ T_d^{*}\end{bmatrix}\Delta\underline{d}\\ l_i \leq \Delta d_i \leq u_i \quad ,\ i=1,\ldots,\text{NDES}\end{gathered} \tag{5-37}$$

where:

$$\begin{Bmatrix}J_d^{*}\\ Q_{id}^{*}\\ Q_{ed}^{*}\\ T_d^{*}\end{Bmatrix} = \begin{Bmatrix}J_d\\ Q_{id}\\ Q_{ed}\\ T_d\end{Bmatrix} - \begin{bmatrix}J_x & J_\gamma\\ Q_{ix} & Q_{i\gamma}\\ Q_{ex} & Q_{e\gamma}\\ T_x & T_\gamma\end{bmatrix}\begin{bmatrix}Q_{qx} & Q_{q\gamma}\\ Q_{wx} & Q_{w\gamma}\end{bmatrix}^{-1}\begin{bmatrix}Q_{qd}\\ Q_{wd}\end{bmatrix} \tag{5-38}$$

5.4 Numerical Considerations

For certain options of KOPT, the simplex algorithm and BFSG update procedure can involve large arrays containing several hundred rows and columns. For problems of this size, numerical accuracy considerations become an important issue. Some of the steps taken in this regard are summarized in Section 5.4.1. Another consequence of such large problems is the increase in the computational time required to both compute the constraint derivatives and to perform the pivoting operations in the simplex scheme. Thus, various options that allow some of these computations to be skipped have been explored and are presented in Section 5.4.2. Finally, convergence tests are given in Section 5.4.3.

5.4.1 Treatment of round-off error

An important consideration in implementing the SLP and SQP algorithms is the presence of round-off error. This is particularly true of larger problems involving several hundred constraints (e.g., incorporation of the equality constraints corresponding to the equations in the EHPIC/HERO code relating the wake point positions, velocities, etc.). Several steps were taken in order to attenuate or else accommodate the effects of round-off error. Prior to the optimization analysis, the simplex tableau is preconditioned by rescaling all entries so as to be of comparable magnitude. First, for each row the entry with the maximum absolute value is found and the row divided by that entry. The same is then repeated for each columns. The latter operation is tantamount to rescaling the state variables, x_j, and is used in determining corresponding scaling factors. Thus, denoting the simplex tableau entries by a_{ij}, the scaling operations proceed as:

$$a_{ij} \leftarrow \frac{a_{ij}}{r_i} \quad , \quad r_i = \max_j \left\{ \mid a_{ij} \mid \right\} \quad , \quad i=1,\ldots,nrow \qquad \text{(5-39a)}$$

$$a_{ij} \leftarrow \frac{a_{ij}}{c_j} \quad , \quad c_j = \max_i \left\{ \mid a_{ij} \mid \right\} \quad , \quad j=1,\ldots,ncol \qquad \text{(5-39b)}$$

where for linear programming,

$$nrow = m+1 \quad ; \quad ncol=n+1 \qquad \text{(5-40a)}$$

and for quadratic programming,

$$nrow= m+n+1 \quad ; \quad ncol=2n+m+1 \qquad \text{(5-40b)}$$

The factor, $1/c_j$, is a representative scale for variable, x_j, and is utilized elsewhere in the optimization algorithm when conducting comparison operations and convergence tests.

The use of double precision for the complete tableau has the undesirable consequence of a four-fold increase in memory requirements. Therefore the use of double precision is restricted to only certain key variables and parameters used in the accumulative summing operations. In particular, double precision is employed for the auxiliary cost and reduced cost coefficients used in finding a feasible solution and, for quadratic programming problems, in satisfying the Kuhn-Tucker. Finally, consideration of round-off error and tableau dimension is made when specifying the tolerance and convergence parameters used in the optimization algorithm.

5.4.2 Efficiency improvement options

The additional computation that must be performed for optimization is categorized into 1) calculation of the influence coefficients pertaining to the design variables, and 2) execution of the SLP or SQP routine to determine the improved design. In many cases, the various influence coefficients change slowly with the design. Furthermore, unless the design is near-optimal, the design changes at each optimization step are the same, i.e., $\Delta \underline{X} / \| \Delta \underline{X} \|$ is constant. These fortuitous properties can be put to good use in diminishing the computational cost. By taking larger steps in design space between optimization calculations and design related influence coefficient evaluation, the total number of operations is substantially reduced, with an accompanying trade-off of a possible lessening in robustness. Rather than effecting the full design change immediately after $\Delta \underline{X}$ has been determined, this design change is implemented over a series of fractional steps. The wake analysis is reconverged during each fractional steps. This improves the robustness of the overall computation since the linearity assumptions implicit in the iterative solution in the wake analysis are more likely to be valid over one fractional step than over the full design change. To this end, the user supplies the input parameters, KWIKN and NFRAC, where NFRAC is the number of fractional steps and KWIKN has the following meanings:

KWIKN=0 - No modification of the optimization procedure. The influence coefficients and the optimization calculation are executed every time the wake analysis is re-converged.

KWIKN=1 - The influence coefficients pertaining to the design variables are updated once every NFRAC steps, but the optimization routine is executed every time the EHPIC/HERO wake analysis has reconverged.

KWIKN=2 - After every NFRAC steps, the influence coefficients corresponding to the design variables are re-evaluated. The move-limits are expanded:

$$\Delta x_i^{max} \leftarrow \text{NFRAC} * \Delta x_i^{max}$$

and the optimal design change, $\Delta \underline{X}$, computed. The design change is then implemented over the next NFRAC steps as:

1) k=1
2) $\underline{X}_k \leftarrow \underline{X}_{k-1} + \frac{1}{\text{NFRAC}} \Delta \underline{X}$
3) Reconverge wake analysis
4) k=k+1
5) If $k \leq$ NFRAC go to step 2

The simplex tableau is stored in the form suggested by Künzi (Reference 57) which affords a m by m reduction in tableau size for the LP case and (m+n) by (m+n) reduction in the QP case. An by n block can be eliminated in the QP situation by recognizing that the tableau coefficients for the Lagrange multiplier vectors, μ_1 and μ_2, are identical except for sign. This is due to the twin observations that: 1) the initial tableau entries corresponding to μ_1 and μ_2 are simply $[-I_n]$ and $[I_n]$ respectively so that the above relationship holds at the start of the simplex manipulations; and 2) the pivoting operations basically consist of row manipulations where each entry in a row is operated upon in the same manner. Thus rows may be multiplied by the same scalar, and scalar multiples of a row may be added to another. It thus follows that columns that are multiples of each other retain that property subsequent to the pivot operations and that furthermore, the constant of proportionality remains unchanged.

5.4.3 Storage requirements

For SQP optimization, storage space on the order of (2n+m) by (n+m) is needed where n is the total no. of variables under consideration (including in addition to the vector of design variables, the vector of bound circulation perturbations and normal/binormal wake point perturbations unless these are explicitly eliminated via Eq. (5-36); and m is the total no. of equality and inequality constraints imposed upon the problem (not including upper and lower bounds imposed upon the variables). The required storage arises from the fact that there is a total of 3n+m variables comprised of the n state variables, x_i, 2n Lagrange multipliers, μ_{1i} and μ_{2i}, associated with each of the lower and upper bounds of x_i, and m Lagrange multipliers, λ_j, associated with the imposed constraints, g_j; and m+n constraints including the m original imposed constraints and the additional n Kuhn-Tucker constraints. The simplex tableau columns corresponding to μ_{1i}

and μ_{2i} differ only in sign and so only one of the columns must be stored (see Appendix A). This reduces the tableau column size from (3n+m) to (2n+m).

The SLP approach requires storage space on the order of n by m. Both the SLP and SQP schemes implicitly enforce the upper and lower bounds on x_i as explained in Appendix A. Thus elimination of the 2n constraints required during the Phase I effort to enforce these bounds are no longer necessary.

5.4.4 Convergence criteria

The selection of suitable convergence tolerances has proved to be a non-trivial task in the multi-dimensional optimizations considered here. The different scales for the design variables (and the $\underline{x}_c$ and $\underline{y}$) are determined in the EHPIC/HERO code and taken into account in convergence tests. However, the chief obstacle in deriving generally applicable convergence tests is due to the large disparities in gradients and curvatures for different cost functions and designs. For example, the thrust is typically one or two orders of magnitude more sensitive to changes in the twist gradient than to sweep perturbations. Thus it can happen that the twist distribution has essentially converged to the optimal design, while the sweep distribution is still undergoing significant modification. A test based upon changes in cost per step might cause premature termination of the optimization since the changes in thrust level are 'small' in comparison to the changes that occurred while the twist distribution was still changing significantly. Thus consideration of the local gradients should be factored into the convergence tests. Other elements that complicate the definition of an appropriate convergence criterion include the possibility of inaccurate approximations to the Hessian matrix, [B], in SQP (can be countered by resetting [B] near a prospective minimum), possible discontinuities in some of the first order derivatives which can arise in implementing a stall model, and, importantly, round-off error.

The following 'classical' convergence tests are available in EHPIC/HERO and are based upon the user supplied tolerance parameter, TOL. The optimization terminates if any of these tests are satisfied. If the user deems the optimization to have terminated prematurely, then TOL may be reduced and the restart option of EHPIC/HERO invoked.

a) $| J^q - J^{q-1} | < \mathrm{TOL} * \mathrm{Min.} \{ | J^0 | , R \}$, for 3 successive optimization steps

b) $| J^q - J^{q-1} | < \mathrm{TOL} * \mathrm{Min.} \{ | J^q | , R \}$, for 3 successive optimization steps

c) $\max_i . \left\{ \frac{\left| x_i^q - x_i^{q-1} \right|}{SC(i)} \right\} \leq \mathrm{TOL}$

d) $\max_i . \left\{ \frac{\Delta x_i^{\max}}{SC(i)} \right\} \leq \mathrm{TOL}$ (for SLP optimization only)

e) $q > q_{\max}$

Here, J^q is the objective (or cost) function at optimization step q, SC(i) is a representative scale computed in EHPIC/HERO for the design variable under consideration, x_i^q is the value of the i-th design variable at optimization step, q, Δx_i^{max} is the move limit for the i-th design variable and is initialized to DSDMAX at q=0, q_{max} is the maximum allowable number of iterations, and the parameter, R, is an estimate of the reduction in cost that can be achieved for the given move limits, DSDMAX(i), and is computed from

$$R = 0.2 * \sum_i \frac{\partial J^0}{\partial x_i} * \mathrm{DSDMAX(i)} \qquad (5\text{-}41)$$

As explained in section 5.2.4, when employing SLP the move limits, Δx_i^{max}, are reduced when proximity to the optimum is detected. This process continues until criterion d) is satisfied.

6. RESULTS OF SAMPLE PROBLEMS: ROTOR PERFORMANCE

6.1 Previous Validation Work

As noted in the discussion above, meaningful design optimization requires that the methods used to model rotor performance produce accurate results. Extensive performance correlation studies were carried out during the development of the original EHPIC Mod 0.0 code (Ref. 9), and additional studies were executed by NASA personnel (Ref. 6) as well as by users of the EHPIC (Mod 1.0) version (Ref. 7). These correlation studies involved tests of many different rotor configurations, including two-, three-, four-, five- and six-bladed helicopter main rotors, three tiltrotor configurations, and several tail rotors. A wide range of designs were examined including tapered planforms, swept planforms, twisted planforms and combinations of each. Nonlinear as well as linear twist schedules were investigated including the very high twist levels characteristic of tiltrotor blades. Several rotors in ground effect have also been studied (Ref. 10, 11). Finally, recent studies (Ref. 60) of more limited scope have shown that EHPIC compares quite favorably and in some respects improves upon the performance results obtained using much more CPU-intensive CFD analyses.

These studies have concluded that the EHPIC code produces very good performance prediction across a broad range of rotor designs. As with any numerical analysis, the results obtained are sensitive to certain key input parameters. However, the results described in Reference 7 were particularly encouraging on this point, in that calculations carried out over several very different rotor systems produced consistently good correlation for a fixed set of inputs - i.e., no use of numerical "dials" was necessary to obtain good results in particular cases. One of the objectives of the present study was to ensure that the changes implemented during the development of the HERO analysis produced the same consistently good performance correlation as its parent EHPIC code. Some changes in the results were unavoidable given the necessity of restructuring the code to adapt to the requirements of carrying out performance optimization. Also, as previously discussed, several improvements in the aerodynamic model have been implemented to eliminate particular limitations of the baseline analysis. The correlation studies that follow are intended to illustrate the fundamental consistency of the optimization hover performance model with the original EHPIC code as well as to highlight the improvements made.

In each of the calculations below, the EHPIC and EHPIC/HERO performance computations used the same number of trailing filaments, extent of free and prescribed wake, vortex lattice discretization, and core modeling. To the extent that the results of the two analyses differ, the differences are analyzed in each particular case. Unless otherwise specified, standard atmospheric conditions are assumed corresponding to a speed of sound of 340 m/s (1117 fps) and atmospheric density of 1.205 kg/m^3 (.002378 slugs/ft^3). Since NASA is currently operating the Mod 1.0 variant of EHPIC, comparisons of HERO and EHPIC here are made with the 1.0 version.

6.1.1 NASA/NACA test rotors

A data set from an NACA rotor tested in the 1950's provides a simple configuration with which to start the present correlation study. The first test rotor examined was that described in Reference 61, which described integrated performance results on a two-bladed rotor with a radius of 8.17 m. (26.8 ft.) and a constant chord of 0.58 m. (1.91 ft.). The blades featured 8 degrees of linear twist and were tested at tip Mach numbers of 0.28 and 0.66. An NACA 0012 airfoil section was used across the full span of the blade. The wake model here used six filaments trailing from the rotor blade. Since the test was conducted on a whirl stand elevated 1.5R above the ground, the ground plane model was invoked to correct for the effect of the image system of vortices. The blade model used 30 vortex quadrilaterals along the span and one chordwise.

Figures 6-1 and 6-2 show the correlation achieved for both tip Mach number cases. The correlation is good across most of the range tested, though some differences start to appear at high thrust. Similar results were obtained with the original EHPIC code, as described in Reference 9. It is instructive to compare the details of the results obtained with EHPIC Mod 1.0 against those obtained with EHPIC/HERO since some modifications have been made to the basic performance model. For simplicity, a case with $M_{tip} = 0.28$ is chosen. Figure 6-3 shows the results of the integrated power and thrust results for runs using EHPIC Mod 1.0 and EHPIC/HERO over a range of collectives. The predictions of the two codes are very close, but some small differences do appear to be present.

Further details are provided by a close examination of a single case. For a root collective pitch angle of 14 degrees , the following integrated performance results were obtained:

	EHPIC/HERO	EHPIC Mod 1.0
C_T	0.003239	0.003261
C_{Qi}	0.0001449	0.0001429
C_{Qp}	0.00004454	0.0004446
C_Q	0.0001895	0.0001875

These results indicate the typical size of differences in performance predicted by EHPIC/HERO and EHPIC Mod 1.0. The profile power calculation yields essentially identical results, as would be expected given that the same airfoil drag characteristics were read in, though in a different format in the new code. Differences in the thrust and induced power are larger, and are attributable primarily to shifting the vortex filament release points to the trailing edge as described in Section 2.3.1. This change was necessary for the implementation of the high-resolution wake roll-up calculation described in Section 3. Figure 6-4 shows the distributed thrust, induced power, and total power for the two calculations. Most of the differences between the two calculations appear in the tip region, while the computed loading inboard of roughly 0.85R is nearly identical.

6.1.2 CH-47B rotor

Performance tests for the CH-47B main rotor are described in Reference 62. The rotor has three blades, each with a constant chord of 0.64 m. (2.1 ft.) and a radius of 9.14 m. (30.0 ft.). The blades feature -9.14 degrees of linear twist and use a 23010-1.58 airfoil section. The data in Reference 62 was taken at rotor rotation rates of 230, 240, and 288 rpm. The case examined here is 240 rpm, corresponding to a tip speed of 229.6 m/sec (753 fps).

The wake model used six filaments trailing from the span, with roughly 2.5 turns of free wake followed by an additional 1.5 turns of prescribed wake. Thirty vortex quadrilaterals were used across the span with one chordwise. The integrated performance predicted for this case is shown in Figure 6-5, indicating good agreement up to high

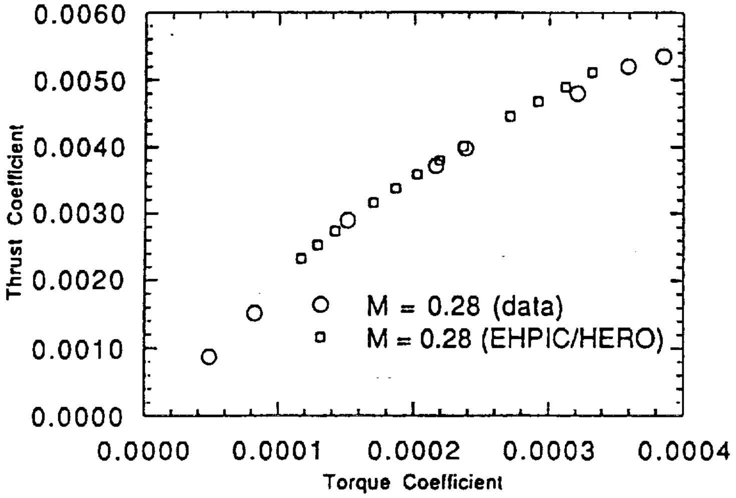

Figure 6-1. Predicted and measured performance of the two bladed NASA TN4357 rotor at $M_{TIP} = 0.28$.

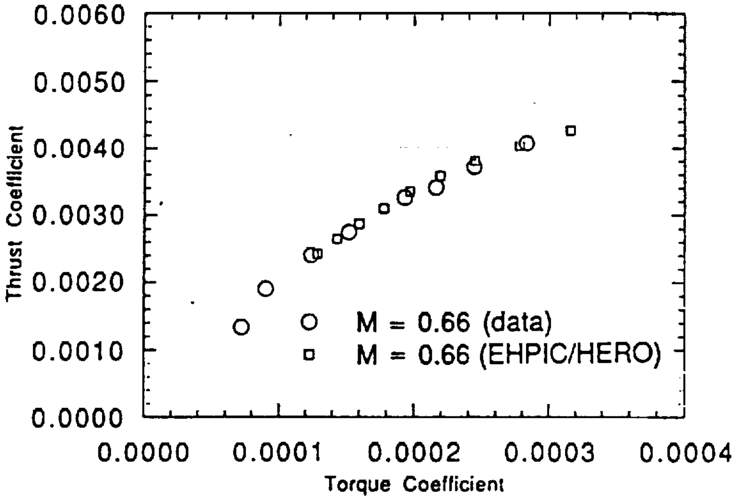

Figure 6-2. Predicted and measured performance of the two bladed NASA TN4357 rotor at $M_{TIP} = 0.66$.

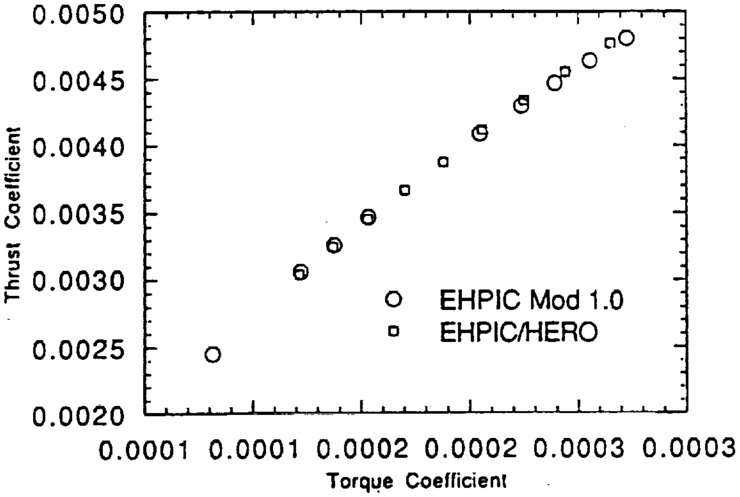

Figure 6-3. Comparison of predicted performance using the EHPIC Mod 1.0 and EHPIC/HERO codes for the NASA TN4357 rotor.

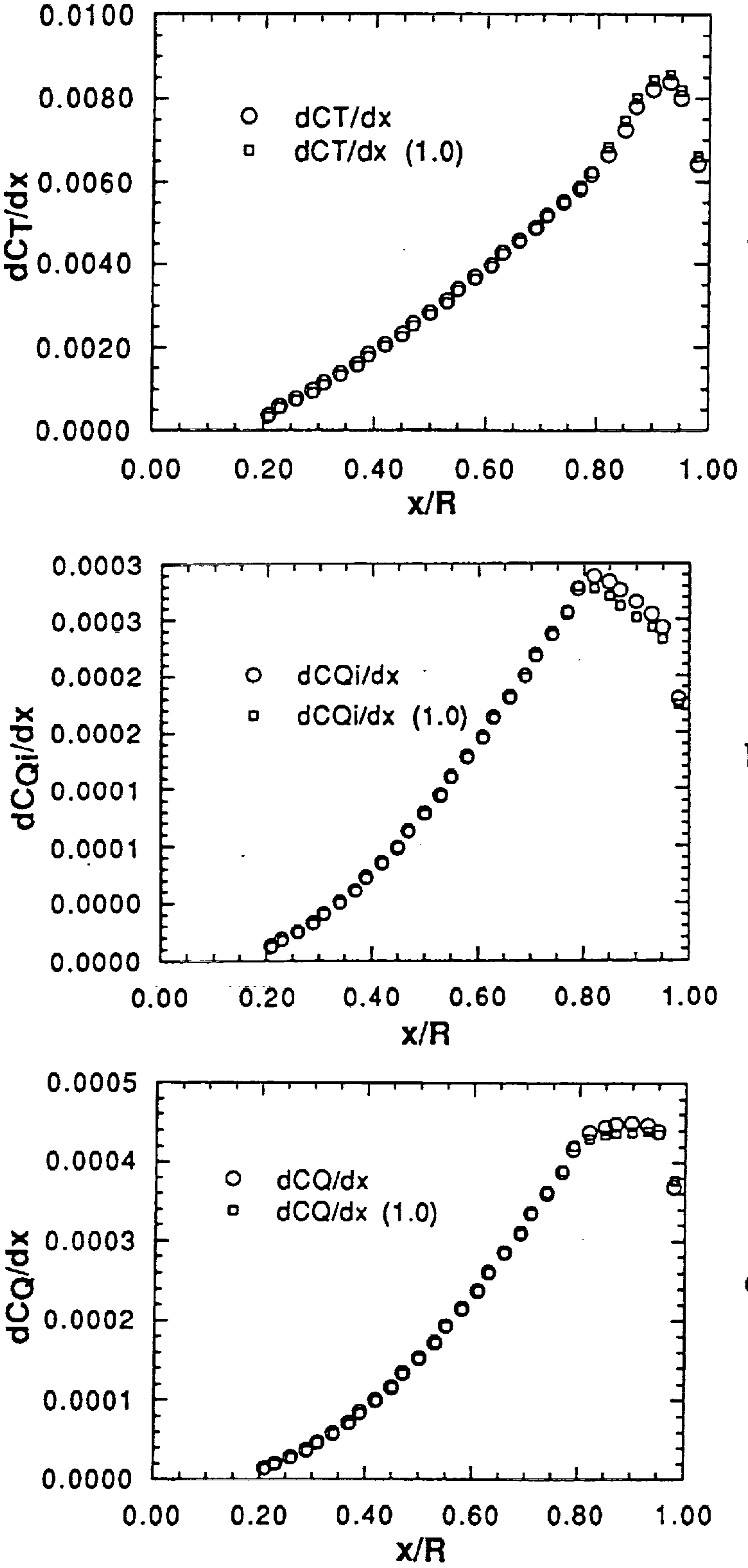

a) dC_T/dx

b) dC_{Qi}/dx

c) dC_Q/dx

Figure 6-4. Predicted distributed loading for the NASA TN4357 rotor.

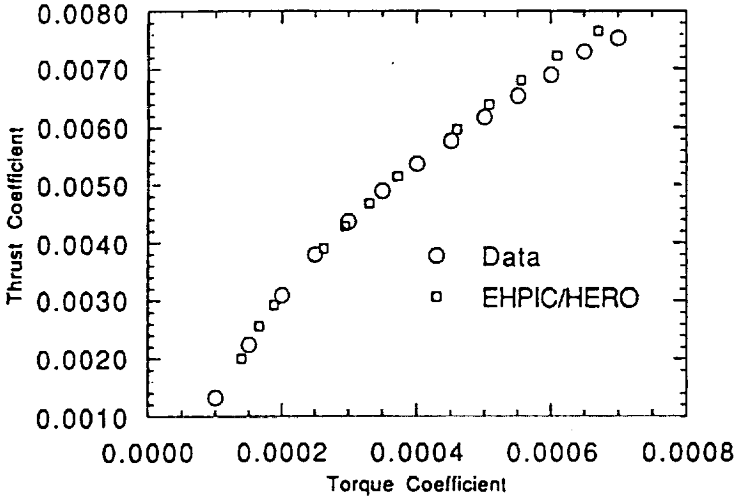

Figure 6-5. Predicted and measured performance for the CH-47B main rotor.

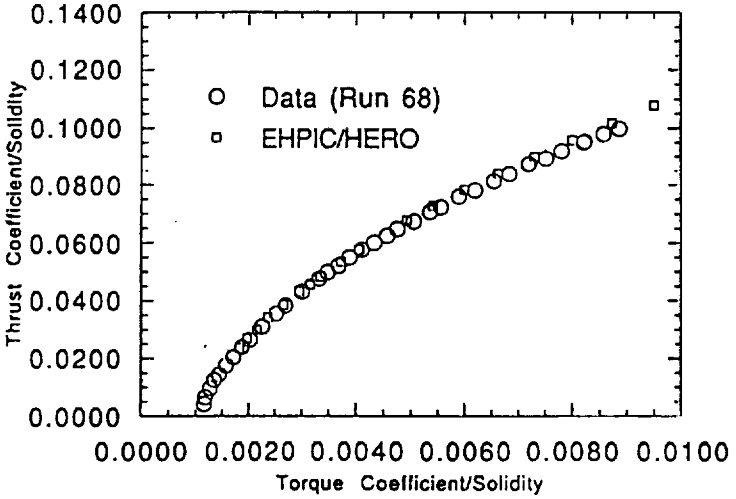

Figure 6-6. Predicted and measured performance for the UH-60A model rotor.

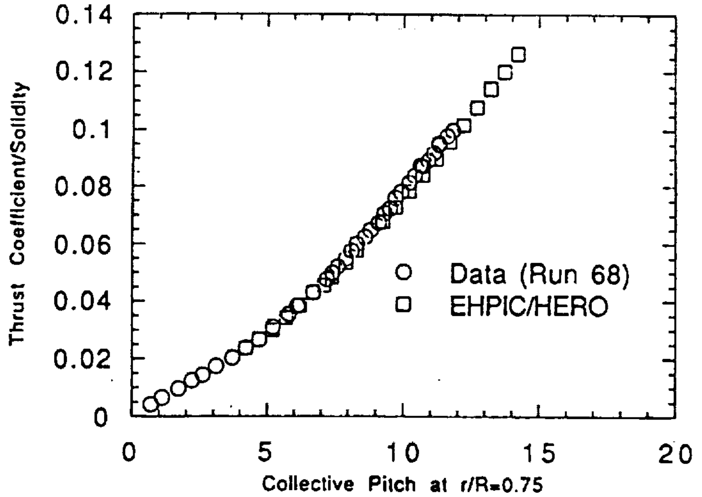

Figure 6-7. Predicted and measured thrust for the UH-60A model rotor.

thrust levels with some deviation beyond that point. The performance predictions are similar to those obtained with EHPIC Mod 0.0 in Reference 9.

6.1.3 UH-60A rotor

Recently acquired data on an extensively instrumented UH-60A model rotor has provided a wealth of potentially useful correlation information for study using EHPIC/HERO. References 63-65 that describe this test were acquired only shortly before the end of this effort, and analysis and interpretation of the results is still ongoing. However, certain major results of the computational studies done to date are available and are presented here.

The model tests described in References 63-65 involved a 8.86 m. (9.4 ft.) diameter, Mach scaled model of the four-bladed UH-60A main rotor. The model featured a chord of .092 m. (0.304 ft.), and was operated at a range of tip Mach numbers between 0.55 and 0.70. This planform features 20 degrees of sweep starting at the 92% radial station, as well as a distinctive and highly nonlinear twist distribution that includes a twist 'bucket' over roughly the outer 10% of the blade span (the UH-60 twist distribution is discussed further in Section 7). The particular case considered here is at tip Mach number 0.65. The blade uses an SC1095 airfoil across the entire span, except for the 'droop nose' SC1095R8 airfoil between 0.47R and 0.82R. The computational model uses 45 equally spaced quadrilaterals spanwise and one chordwise. Six free filaments are used, with one capturing the wake of the tip region and five used to model the inboard sheet.

Figure 6-6 shows the prediction of integrated loading for Run 68 of Reference 63. The power prediction is close over most of the range surveyed, though with some underprediction of the power at higher thrusts. The prediction of thrust as a function of collective pitch is likewise close, as shown in Figure 6-7. At high thrust levels, EHPIC/HERO tends to slightly overpredict the actual thrust.

The tests described in References 63-65 involve some runs at very high thrust coefficient, so it was judged a suitable test case for the static stall model discussed in Section 2. However, the range of thrust coefficients tested did not in fact pass the $c_{l_{max}}$ level for the airfoil tables tested, as indicated in Figure 6-8. The computations do show that the qualitative behavior of the present model is reasonable, predicting a drop-off in thrust growth with collective (Figure 6-8) along with a rapid increase in power required (Figures 6-9 and 6-10) once the stall model is activated. (The primary purpose of the stall model is to limit performance at twist angles above the section stall angle during the optimization process. Most current planform designs operate far below the stall regime so the stall model will not affect comparisons with test results.)

As noted above, References 63-65 contain a wide range of experimental measurements suitable for further correlation studies, though the recent (early 1992) release of the data has precluded detailed consideration here. In particular, Reference 65 documents measured structural deflections that could be of considerable value in validating the structural deflection model described in Section 4. It is anticipated that future validation efforts will include such correlations, as well as studies of the spanwise loading and wake geometry data contained therein.

6.1.4 XV-15 rotor

As noted in the wake geometry calculations in Section 3, the XV-15 rotor is a three bladed configuration with a radius of 3.81 m. (12.5 ft.) and a constant chord of

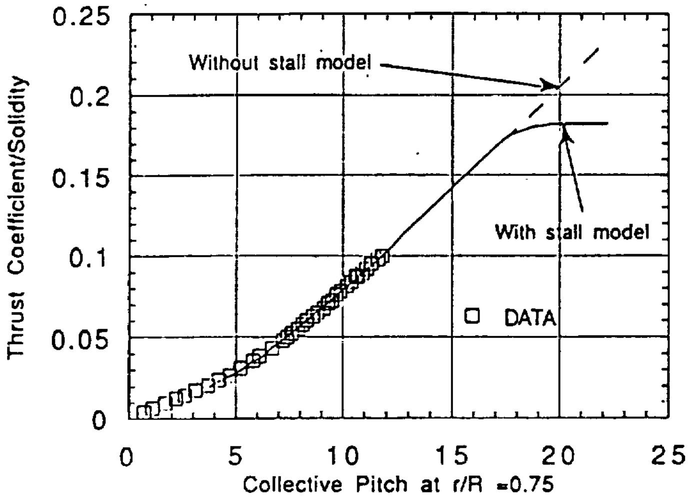

Figure 6-8. Rotor thrust predictions versus collective with and without stall model (UH-60A model rotor).

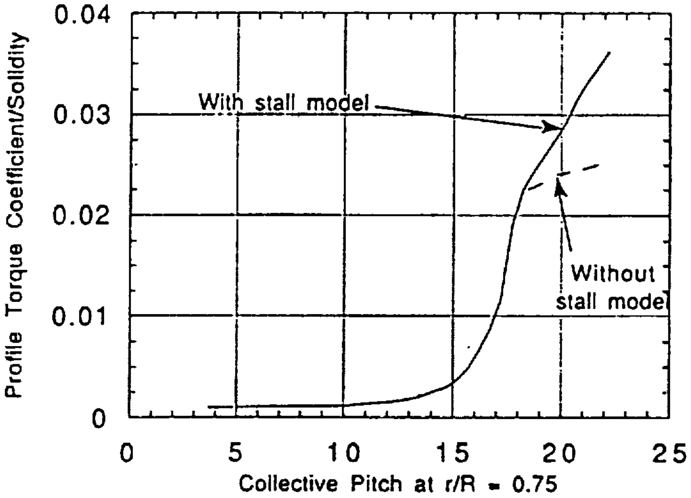

Figure 6-9. Rotor profile torque predictions versus collective with and without stall model (UH-60A model rotor).

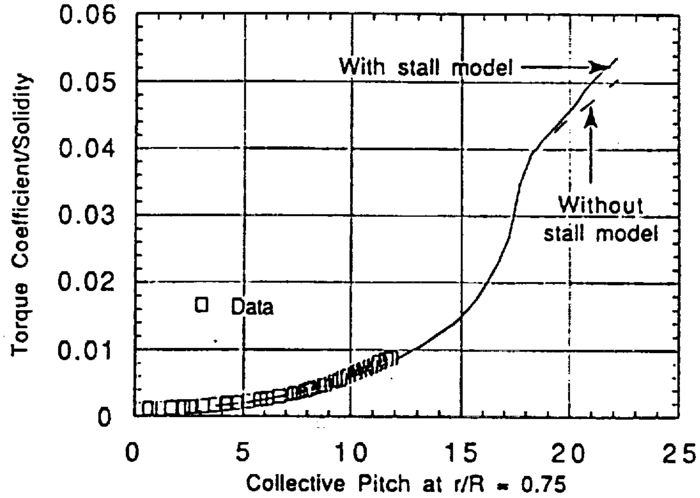

Figure 6-10. Total rotor torque predictions versus collective with and without stall model (UH-60A model rotor).

0.354 m. (1.16 ft.). The twist distribution features a nonlinear twist distribution with a total washout of approximately forty degrees across the span. Each blade uses five NACA 64-class airfoils across the span. The tip Mach number for the cases studied here was 0.69, and the measured performance is drawn from Reference 45. The same blade model with 45 vortex quadrilaterals spanwise and 1 chordwise used in Section 3 was used here, though the present calculations employ eight equally spaced filaments to obtain good resolution of the spanwise distribution of induced velocity.

Figure 6-11 shows the correlation achieved across the moderate to high thrust range of most practical interest. The calculations are compared to two different runs from Reference 45 that bracket most of the range of data taken in the test. The correlation is good across the range examined, though there is some tendency to underpredict the power at low thrust levels.

6.1.5 V-22 rotor

Reference 27 discusses performance measurements taken on a 0.658-scale V-22 rotor. Like the XV-15, the V-22 is a three-bladed rotor with a large, nonlinear washout across the span, with a total of approximately 40 degrees of twist across the span. The scaled V-22 rotor has the same radius as the XV-15 but also features a tapered planform, with the chord ramping down from 0.58 m. (1.9 ft.) at the root to 0.405 m. (1.33 ft.) at the tip. The tip Mach number for these tests was 0.68, corresponding to a tip speed of 231.7 m/sec (759.7 ft/sec) at standard conditions. The wake and blade model were identical to those used for the XV-15 case. The results obtained here were likewise similar; Figure 6-12 shows the correlation of integrated performance, again indicating good general agreement, though with some errors appearing at both the low and high end of the range examined.

6.2 Performance in Axial Flight

Only limited measured performance data is presently available for proprotors in high speed axial flight. One of the designs of high current interest in this area is the V-22 rotor, whose performance is discussed in Reference 66. Felker describes the following closed-form semi-empirical expression for integrated rotor power that has been quite successful in capturing on-design propulsive efficiency for the V-22 (Ref. 67).

$$C_Q = C_{Q_P} + \mu C_T + \frac{C_T^2}{2\mu}$$

$$C_{Q_P} = f_c C_{Q_0}\left[\left(1+\frac{5}{2}\mu^2\right)\sqrt{1+\mu^2} + \frac{3}{2}\mu^4 \ln\left(\frac{1+\sqrt{1+\mu^2}}{\mu}\right)\right]$$

where f_c is an empirically-derived compressibility adjustment factor for the profile drag:

$$f_c = \left\{\begin{array}{c} 1, \text{ if } M_{.75} \leq 0.63, \text{ otherwise} \\ 1 + 42.51\,(M_{.75} - 0.63) + 3476\,(M_{.75} - 0.63)^4 \end{array}\right\}$$

$$M_{.75} = M_\alpha \sqrt{1 + \frac{9}{16\mu^2}}$$

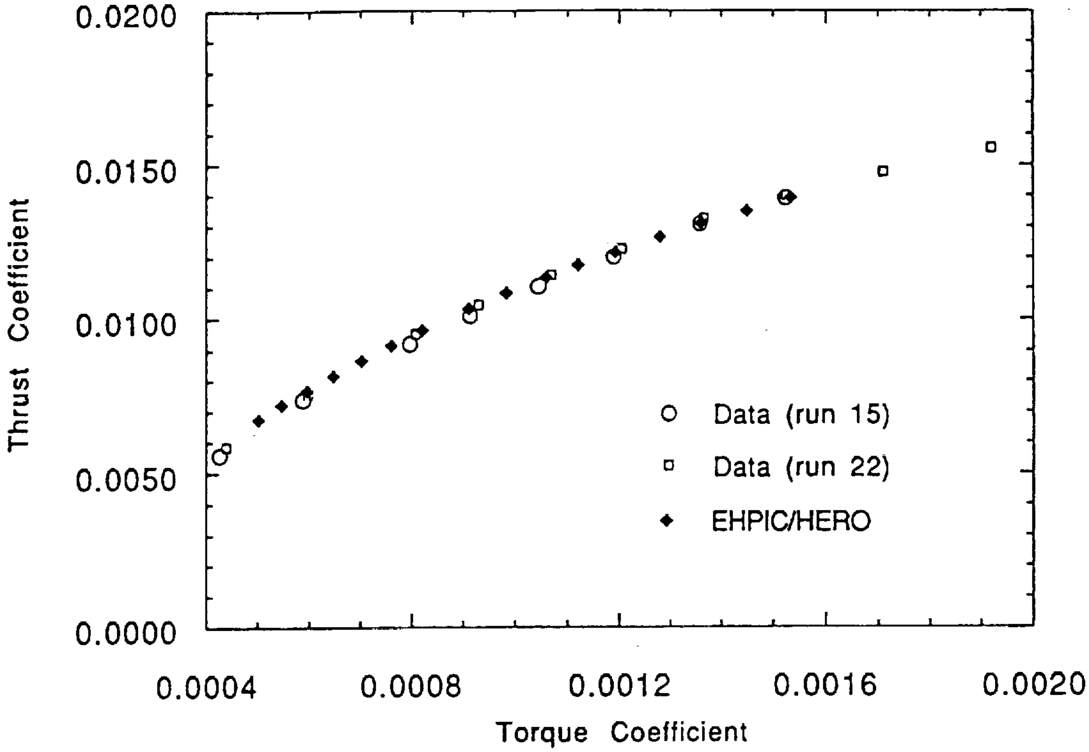

Figure 6-11. Predicted and measured performance for the XV-15 rotor.

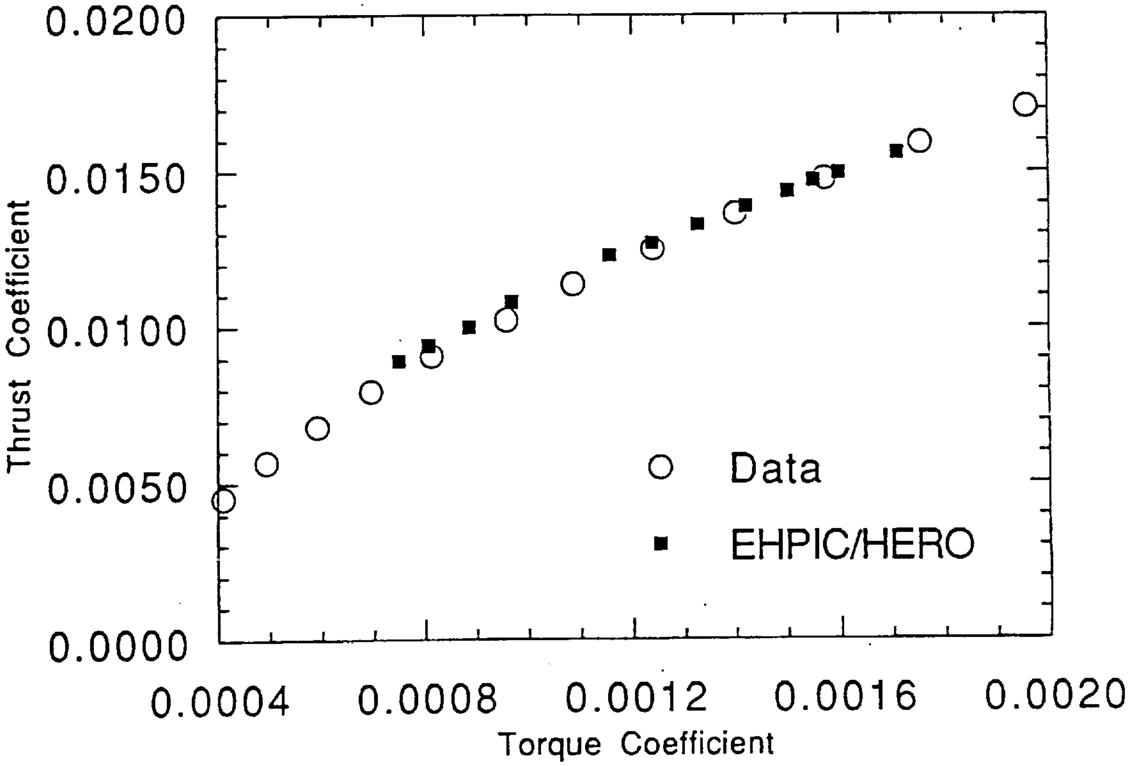

Figure 6-12. Predicted and measured performance for the 0.658-scale V-22 rotor.

In order to test the capability of EHPIC/HERO to successfully analyze rotors in high speed axial flight this formula was used in place of directly measured performance. Curves of rotor propulsive efficiency $\mu C_T/C_p$ as a function of thrust coefficient were made for two flight conditions: first, $\mu = 0.34$ and $M_{hel} = 0.62$ and, second, $\mu = 0.67$ and $M_{hel} = 0.59$.

Since rotor wake effects are very weak in high speed axial flight, very simple wake models are appropriate for these flight conditions. In this case, five free filaments with one turn of free wake were used, though the filaments are quickly convected downstream, behaving essentially as a kinematic wake. With thirty vortex quadrilaterals across the span, good resolution of spanwise loading could be expected. The integrated performance results shown in Figures 6-13 and 6-14 indicate that the major features of rotor performance are in fact being captured. For the moderate speed case shown in Figure 6-13, the prediction accuracy is good across most of the range, while for the high speed case shown in Figure 6-14, a consistent underprediction of propulsive efficiency is apparent. The presence of such a constant decrement suggests inadequacies in the profile power calculation, possibly in the high Mach number section data for the airfoils used on the rotor.

Figure 6-15 shows a comparison between predicted and measured performance for the V-22 rotor in low speed axial flight. A small range of EHPIC/HERO results are shown at three advance ratios, $\mu = .0236$, .0313, and .0381. Only one test data point was available at each of these advance ratios. EHPIC/HERO shows good agreement at the two lower values but begins to over-predict the torque at $\mu = .0381$. Further test data will have to be obtained in order to determine whether this trend occurs with increasing advance ratio or increasing thrust.

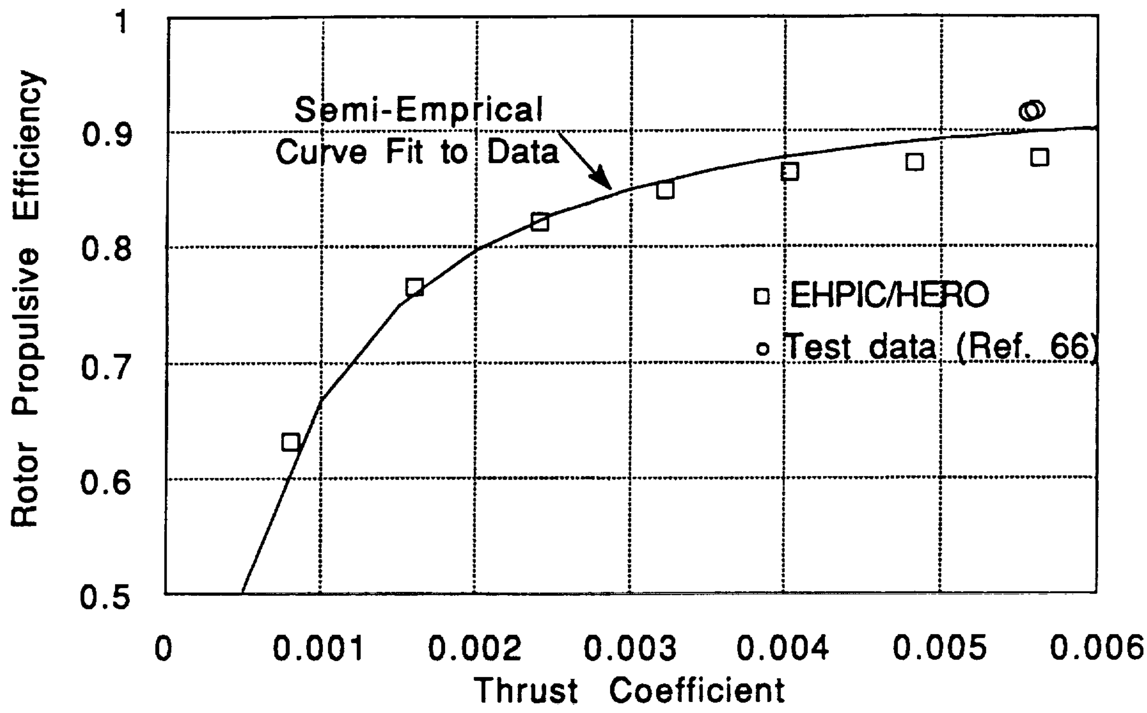

Figure 6-13. EHPIC/HERO prediction of V-22 propulsive efficiency in high speed axial flight: advance ratio 0.34, $M_{hel} = 0.62$.

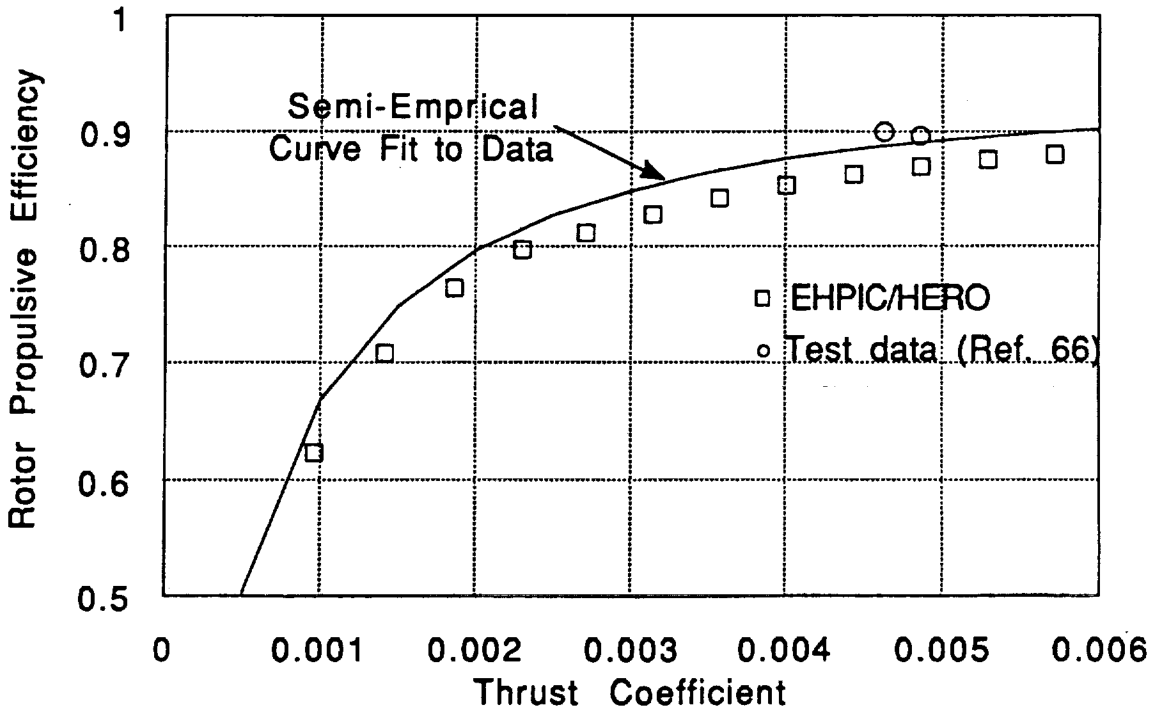

Figure 6-14. EHPIC/HERO prediction of V-22 propulsive efficiency in high speed axial flight: advance ratio 0.67, $M_{hel} = 0.59$.

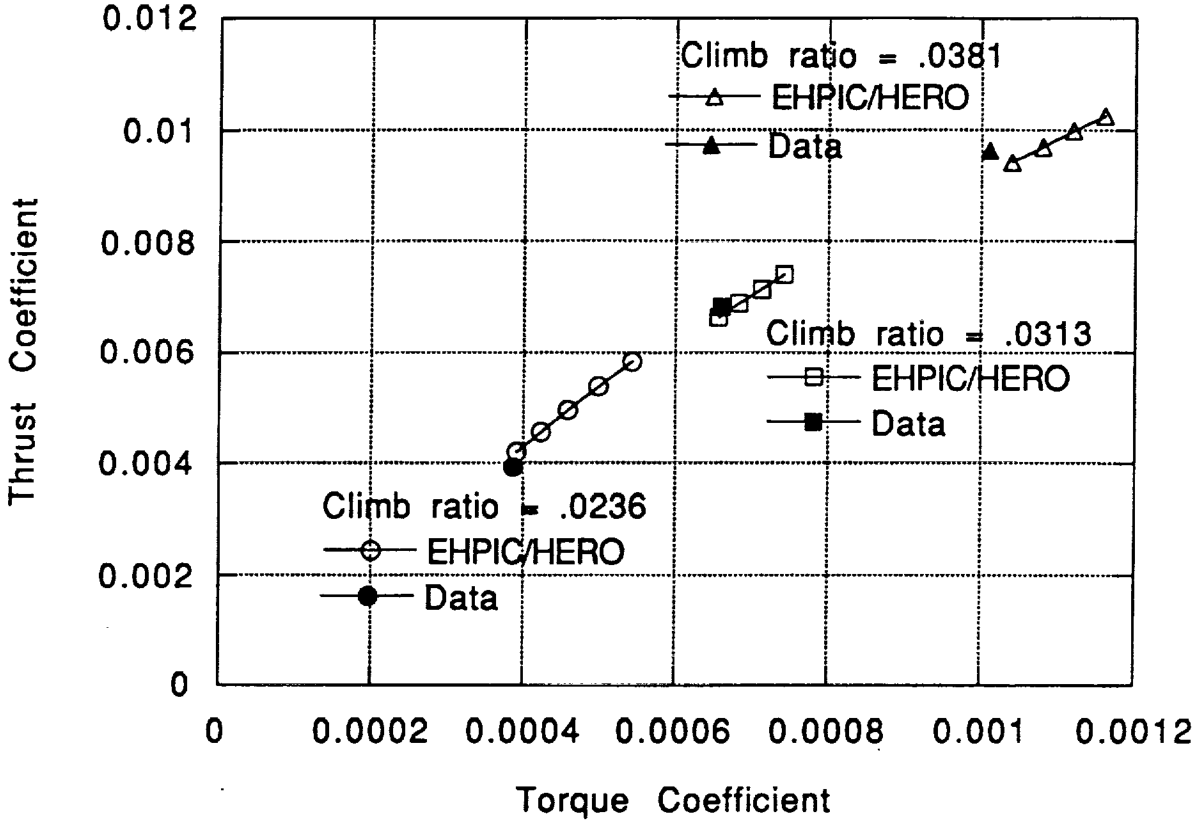

Figure 6-15. Predicted and measured performance for the V-22 rotor in low speed axial flight: advance ratios ($V_{climb}/\Omega R$) of .0236, .0313 and .0381 and $M_{hel} \approx 0.57$.

7. RESULTS OF SAMPLE PROBLEMS: DESIGN OPTIMIZATION

This section presents results that illustrate the application of the EHPIC/HERO code in optimization calculations for rotors in hover and axial flight. The initial focus of interest is on the problem of power minimization at a given rotor thrust for rotors in hover. This is the rotary-wing analog to the classical fixed-wing drag minimization problem that still commands attention today. The power minimization problem is likewise critical in rotorcraft design because of its importance in sizing the powerplant to satisfy payload requirements. Here, we analyze several representative configurations to both illustrate the capabilities of the present formulation and to gain insight into promising general design strategies.

As noted in Section 5, EHPIC/HERO has the ability to define a variety of objective functions besides total rotor power. Gross thrust, hover Figure of Merit, axial propulsive efficiency, and individual components of total power (i.e., induced and profile) may be selected, as may weighted combinations of these quantities. We will show results of selected problems executed using some of these alternative objective functions for hovering rotors, including thrust maximization for a fixed power.

EHPIC/HERO is also suited to the analysis of rotors in axial flight, as discussed in Section 6. The design requirements of rotors in high speed axial flight (e.g., tiltrotors in cruise) are distinct from those of rotors in hover. The influence of the wake is much reduced, so much so that uniform inflow approximations can often be used with some success, as the discussion of performance results in Section 6 indicates. However, even though the free wake feature of the present analysis is not as important as in hover, the lifting surface/vortex lattice aerodynamic model in EHPIC/HERO can be used to good effect here, since the design evolution of proprotors often calls for swept and variable chord planforms. The performance results for axial flight calculations to date have been promising, and it is anticipated that application of the design optimization process to rotors in high speed axial flight will yield informative results.

Finally, it should be noted that the purpose of these demonstration calculations was not to comprehensively exercise the extensive set of design optimization options within EHPIC/HERO. The design evolution in particular cases is a function of the constraints imposed, the algorithms selected, and to some extent of the numerical resolution of the blade and the wake that is compatible with the user's computational constraints. The immediate objective here is to present calculations that illustrate some of the major capabilities of the present analysis. As will be discussed, certain broad trends were observed in the calculations performed to date that appear to represent generally desirable design strategies for rotor blades, while other cases provoke as many questions as they answer.

7.1 Sample Calculations in Hover: Rotor Power Minimization at Constant Thrust

7.1.1 Conventional low-twist helicopter designs

Demonstration calculations of performance optimization were carried out on a planform similar to the UH-60A model rotor analyzed in Section 6, but without the tip sweep and twist 'bucket' characteristic of that blade (Figure 7-1). The resulting blade was straight and untapered, with a radius of 4.68 ft. and a constant chord of 0.303 ft. The resulting twist distribution yields a -16 deg. twist rate across the blade radius. An initial

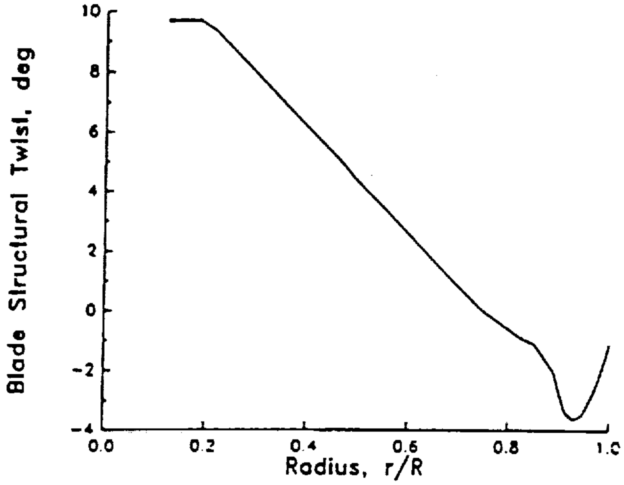

Figure 7-1. Twist distribution of the UH-60A model rotor blade.

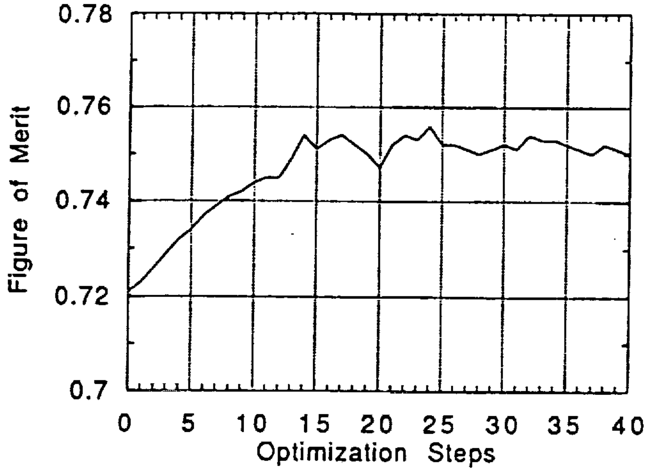

Figure 7-2. Figure of merit history during design optimization of a four-bladed UH-60A-class rotor: twist and tip sweep.

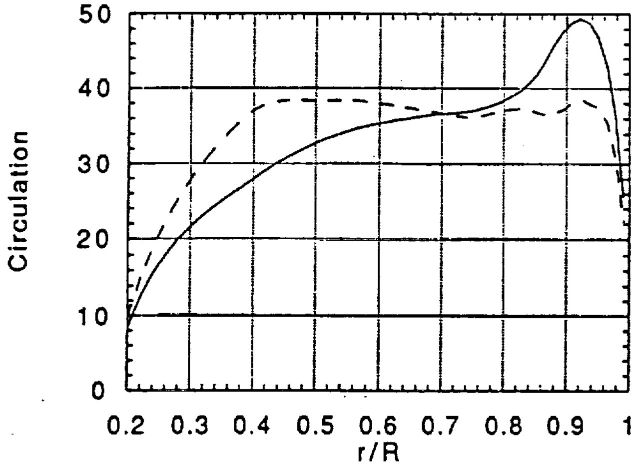

Figure 7-3. Initial (solid) and final (dashed) bound circulation distributions for the twist/tip sweep optimization.

condition with thrust coefficient of 0.00664 was selected, which corresponds to C_T/σ of 0.0805 and a Figure of Merit of 0.721.

The same wake configuration used in the performance studies of the UH-60A model blade in Section 6 was used here. The blade was discretized into ten unequal segments, ranging in width from 0.125R to 0.025R, with the smaller elements concentrated near the tip to capture the expected rapid design gradients in that region. Unless otherwise noted in the text below, the sequential linear programming (SLP) option was used, and all blades were considered rigid (no structural deformation allowed). As described previously, while the structural model has been validated through the use of idealized calculations and comparisons with analytical results, a calibration against measured blade deflection has not yet been performed.

Several different combinations of design variables were selected for investigation. These were: twist and tip sweep; twist and tip anhedral; and twist and variable chord. In each case, the twist was constrained to have twist changes between -8.5 and +1.5 degrees on each segment. This 10 degree range was judged to give ample latitude for potentially interesting design trends to appear without producing unrealistic configurations.

Twist and tip sweep: In this case, the outer 7% of the blade was allowed to sweep up to +/-30 deg. The results of this case are summarized in Figures 7-2 to 7-4. Figure 7-2 shows the history of the evolution of the hover Figure of Merit during the calculation, as it rises to roughly 0.75 from its initial value of 0.721. Though the calculation dithers considerably around the plateau, the bulk of the improvement comes in the first fifteen design optimization steps, during which time the tip sweep angle ramps up monotonically from zero to the upper bound of 30 deg. The twist distribution undergoes dramatic evolution during this period also, as shown in Figure 7-4. The distribution begins to develop the twist bucket near the tip originally built in to the UH-60A. Some tendency to increased twist over the inboard part of the blade is also observed. The overall tendency of the evolution of the bound circulation distribution, though, is to flatten out the peak in circulation seen near the tip and to produce a much more uniform distribution (Fig. 7-3). As will be seen, this trend is evident in a wide variety of the cases studied to date.

Twist and tip anhedral: This case produces results in many respects qualitatively similar to the previous exercise. The same discretization of the blade was used, with ten segments of decreasing span being used. Here the outer 17% of the blade was allowed to deflect in anhedral, with the deflection limited to +/-15 deg. Again the twist distribution was allowed to vary across the full span. Figure 7-5 shows the history of the Figure of Merit as a function of number of optimization steps. Once again, a rapid rise is observed during which the anhedral angle (tip droop) ramps rapidly to its prescribed limit. The relatively large fluctuations observed in the Figure of Merit in steps 10-15 are due to adjustments in the strength and position of the wake. These changes settle down to a relatively stable plateau after steps 15-20. The predicted twist distribution associated with the drooped tip is shown in Figure 7-7, showing a smaller twist bucket near the tip, though again with larger twist angles toward the root. The resulting bound circulation distribution at the termination of the calculation contains an anomalous trough that appeared to be diminishing as the calculation plateaued around step 40 (Figure 7-6).

Twist and chord: Here, both the chord and the twist distribution were allowed to vary. The chord was constrained to stay at its baseline value of 0.305 ft. over the inner

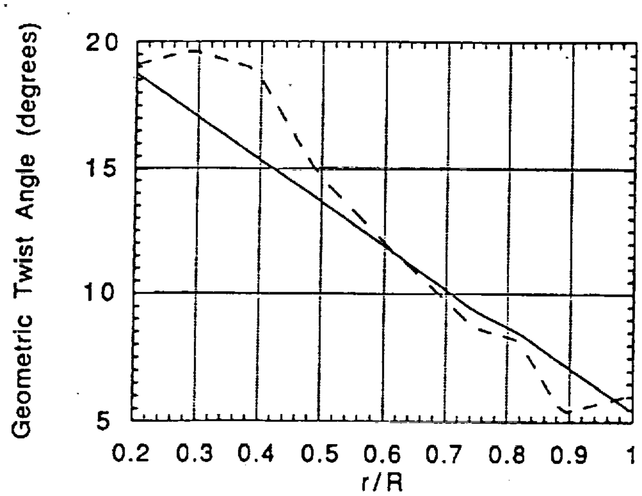

Figure 7-4. Initial (solid) and final (dashed) geometric twist distributions for the twist/tip sweep optimization.

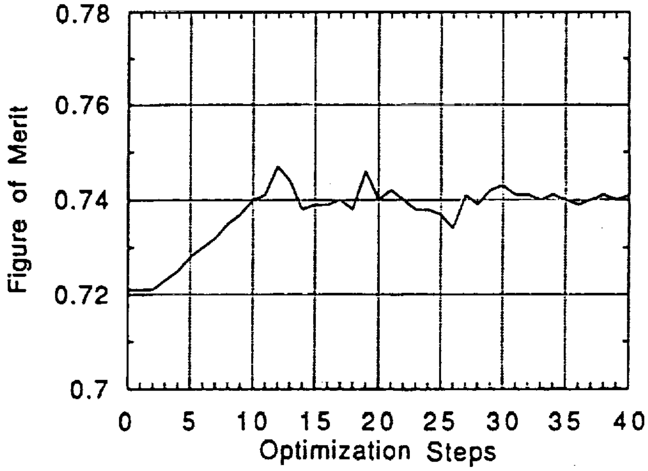

Figure 7-5. Figure of merit history during design optimization of a four-bladed UH-60A-class rotor: twist and tip droop (anhedral).

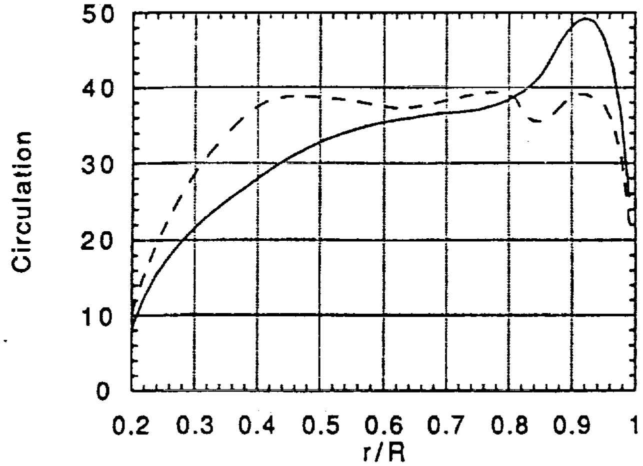

Figure 7-6. Initial (solid) and final (dashed) bound circulation distributions for the twist/tip anhedral optimization.

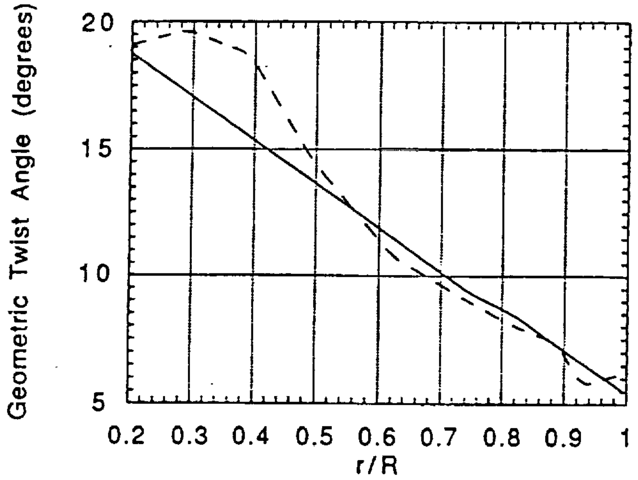

Figure 7-7. Initial (solid) and final (dashed) geometric twist distributions for the twist/tip anhedral optimization.

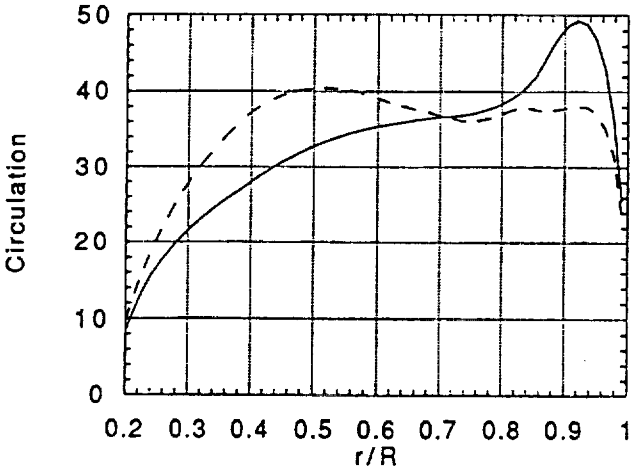

Figure 7-8. Initial (solid) and final (dashed) bound circulation distributions for the twist/chord optimization.

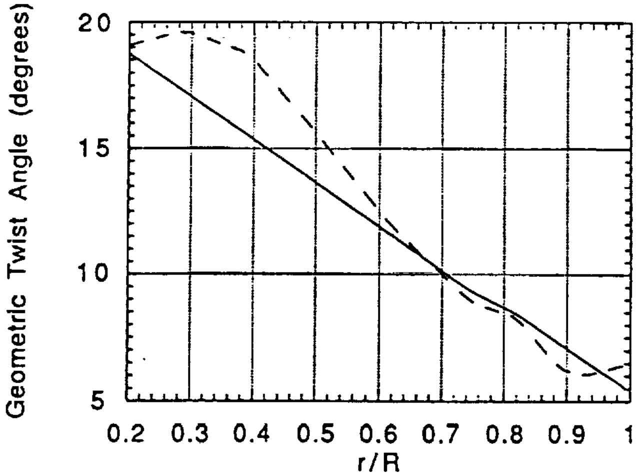

Figure 7-9. Initial (solid) and final (dashed) geometric twist distributions for the twist/chord optimization.

40% of the span, while outboard of this point increases of up to 33% over the baseline were allowed; the minimum permissible chord in this region was set at 0.1 ft., or one third of the baseline. In this case, the Figure of Merit increased from the baseline value to just under 0.77 in thirty steps after which point the performance leveled off. The chord distribution tapered gradually down to 0.18 ft. from the end of the fixed-chord segment, while chords as large or larger than the baseline appeared in the immediate vicinity of the tip. Figure 7-9 shows the twist distribution obtained for this case, which is similar to the other two cases just discussed. The tendency to a constant circulation distribution is shared with the previous calculations. Further investigation will be required to determine if the increased chord at the planform tip is a consequence of the lattice discretization used or if it represents a physically meaningful event.

These calculations indicate that representative baseline configurations can achieve substantial performance increments of 3-4 points in Figure of Merit without excessive or radical design departures. What is of more interest than the particular numerical results achieved is the appearance of two trends in the design evolution: the tendency to smoother, flatter bound circulation distributions and the appearance of features resembling the twist bucket shown in Figure 7-1 near the tip. Some indications of the desirability of flatter circulation distributions were present in the sample cases studied in Reference 4, and the trend is reasonable in light of classical studies of the advantages of uniform downwash fields. A flat circulation distribution minimizes the strength of the wake circulation and hence, in general, minimizes the induced power caused by wake downwash on the blade.

The appearance of the twist bucket, though found empirically desirable by the designers of the UH-60, is not a feature that emerges naturally from simple performance analysis. It is noteworthy that the trend toward this particular design feature is driven largely by the minimization of induced rather than profile power. Repeating the calculations shown above with the profile power artificially set to zero - while obviously leading to lower overall power - still yields twist distributions with the down-up distribution near the tip characteristic of the bucket in Figure 7-1. A likely interpretation is that the down-up twist distribution contributes to the leveling of the circulation distribution by dropping the load near the peak and increasing it at the blade tip. A similar phenomenon can be seen near the root.

7.1.2 Tiltrotor

The design optimization of a tiltrotor in hover presents a substantially different challenge from the computations just described for more conventional low-twist baseline designs. A representative case was examined to investigate possible design improvements in baseline tiltrotor designs. The case considered here for illustration is an XV-15 rotor with the same operating state and planform as those studied in Section 6. For this case, optimization of twist and tip sweep was considered. The twist changes were effectively unconstrained, while sweep was constrained to be zero except for the last 10% of the blade, which could adopt a sweep of +/-30 deg. The thrust coefficient of the base case was 0.0127, while the Figure of Merit was 0.789.

The evolution of the Figure of Merit is shown in Figure 7-10. The history is notably uneven, but levels off around 0.815, corresponding to roughly a 3% power reduction at constant thrust. The unevenness in the advance of the Figure of Merit is attributable in part to oscillations in the tip sweep angle as it ramps up from zero to 30 degrees at step 30. The total performance increment for this case is relatively modest, but this is not surprising if the initial and final bound circulation distributions are considered (Figure 7-11). The initial bound circulation distribution here was already relatively

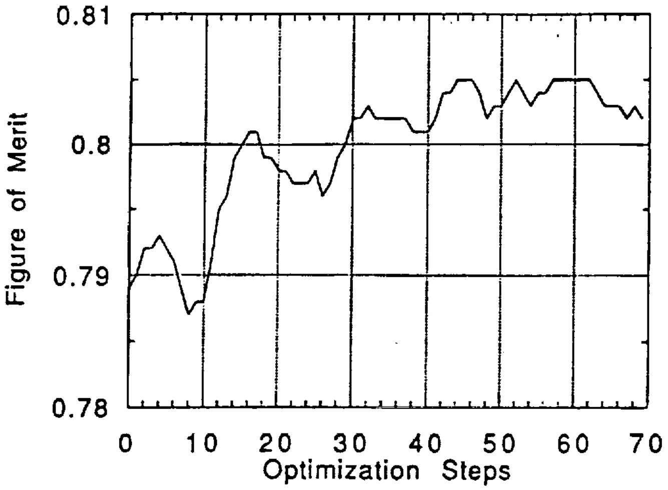

Figure 7-10. Figure of merit during design optimization of an XV-15 tiltrotor.

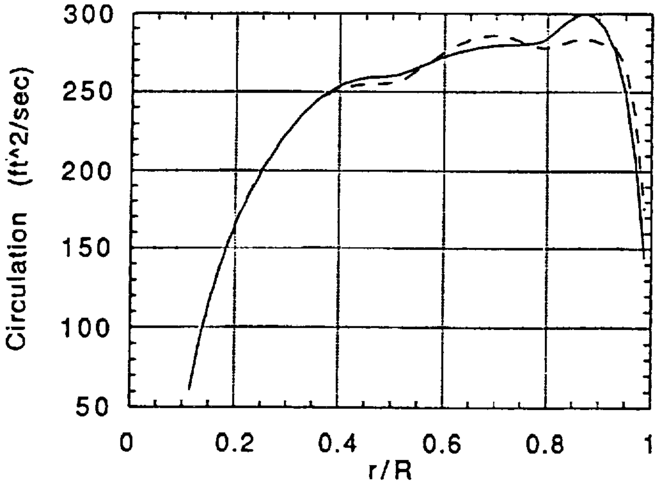

Figure 7-11. Initial (solid) and final (dashed) bound circulation distributions for the XV-15 power minimization.

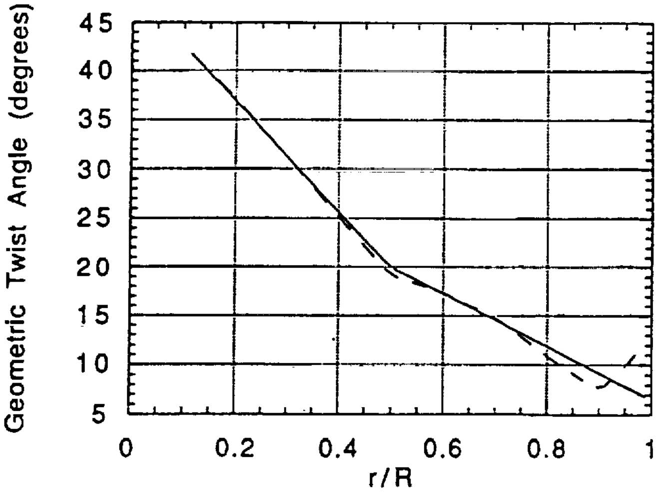

Figure 7-12. Initial (solid) and final (dashed) geometric twist distributions for the XV-15 power minimization.

uniform and left little latitude for subsequent modifications. It is noteworthy, though, that the principal change made by the analysis is the introduction of an up-twist near the blade tip (Figure 7-12). This feature is qualitatively similar to that found in the calculations in Section 7.1. Its appearance in a configuration radically different from the low-twist, four-bladed design just discussed suggests that the introduction of this type of twist distribution may be a generically desirable design feature for a wide variety of rotors.

7.2 Alternate Objective Functions

All of the cases considered to this point have been power minimizations at constant thrust. Many other types of performance optimization problems are of practical interest, and a wide range of objective functions can be accommodated, as discussed in Section 5. A sample calculation was undertaken to demonstrate this capability; the problem involves thrust maximization at constant power, corresponding conceptually to the task of maximizing payload for a given power plant. The base case used here was the same UH-60A-class rotor studied in Section 7.1.

Starting from the baseline thrust coefficient of 0.00664, the design was allowed to evolve with the same constraints imposed in the twist and tip sweep optimization described in Section 7.1. The resulting histories of thrust and Figure of Merit are shown in Figures 7-13 and 7-14. A thrust increase of roughly 2.9% is achieved, with a corresponding increase in Figure of Merit of approximately .038 as a consequence of the constant power constraint. The spanwise loading and geometric twist (Figures 7-15 and 7-16) for this 'thrust optimized' design are similar to the distributions obtained in the 'power optimized' design discussed above.

As described in Section 5, many other candidate objective functions can be accommodated within EHPIC/HERO, including weighted functions of thrust, power (and its induced and profile components), Figure of Merit, and propulsive efficiency ($\mu C_T/C_P$) for axial flight. The latter case is now considered.

7.3 Axial Flight: Tiltrotor/Proprotor Case

Existing and proposed tiltrotor designs call for blade designs that can operate efficiently at very high axial flow rates, typically as high as 450 fps. The discussion in Section 6 included predictions of the performance of a V-22 tiltrotor in two cruise conditions. Here, a study was undertaken to investigate the design trends when improved designs were sought for a representative high speed case.

Adopting a strategy analogous to that described for conventional rotors in Section 7.1.1, the baseline configuration selected was a nonspecific but representative tiltrotor planform, having characteristics similar to the 0.658-scale V-22 rotor and the XV-15 rotor studied in Section 6. The design featured a three-bladed 3.81 m. (12.5 ft.) radius rotor with a constant chord of 0.457 m. (1.5 ft.) yielding a solidity of 0.088 and -40 degrees of washout, assumed to be linearly distributed from the root to the tip. Given the selected operating condition of 112.5 m/sec (369 ft/sec or 219 kts), the advance ratio was 0.67 and the helical tip Mach number was 0.59. Each blade uses five NACA 64-class airfoils across the span as in the XV-15 case discussed previously in Section 6.1.4.

The blade was initialized with 30 constant-width vortex quadrilaterals across the span and one chordwise. Because of the dominance of free stream convection, a relatively coarse wake model with a single turn of free wake on five free filaments is

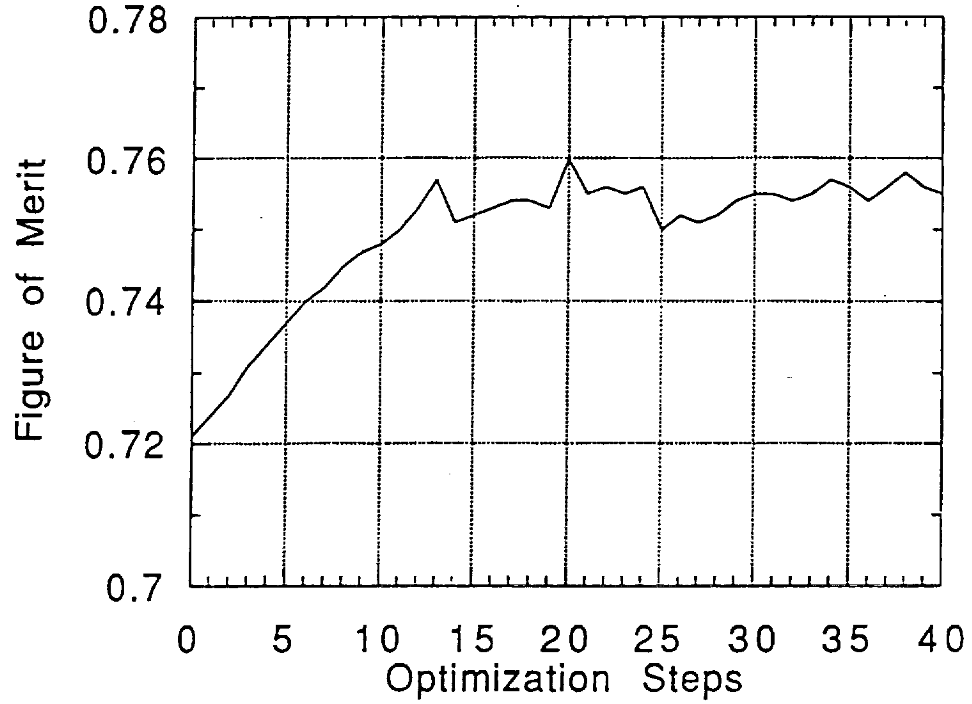

Figure 7-13. Figure of merit history during design optimization of a UH-60A-class four bladed rotor: thrust maximization using twist and sweep.

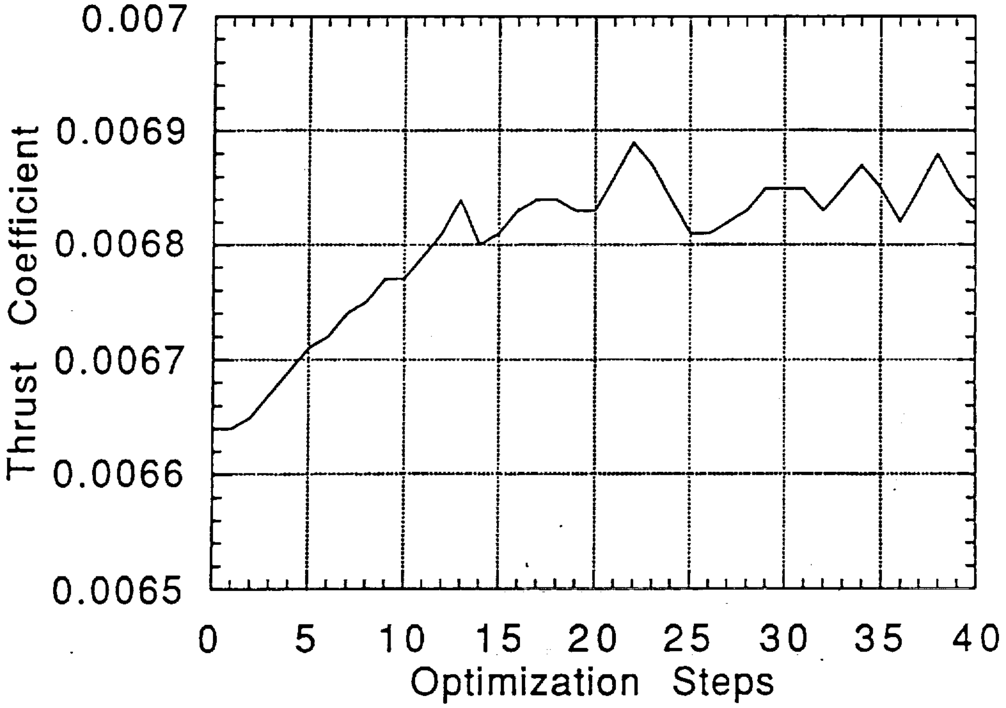

Figure 7-14. Thrust coefficient history during design optimization of a UH-60A-class four bladed rotor: thrust maximization using twist and sweep.

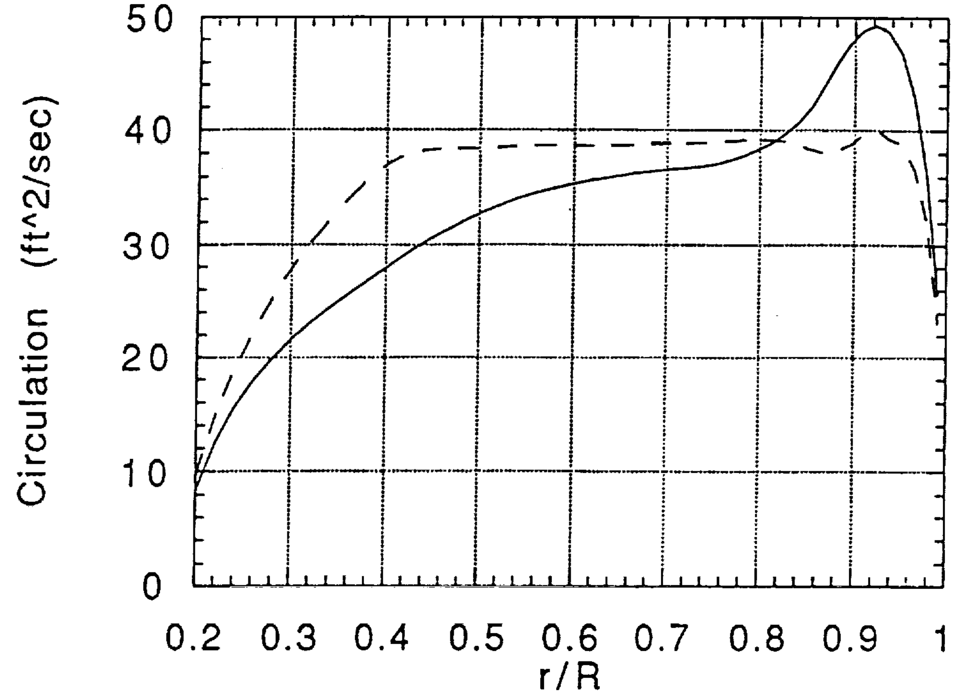

Figure 7-15. Initial (solid) and final (dashed) bound circulation for the thrust maximization calculation.

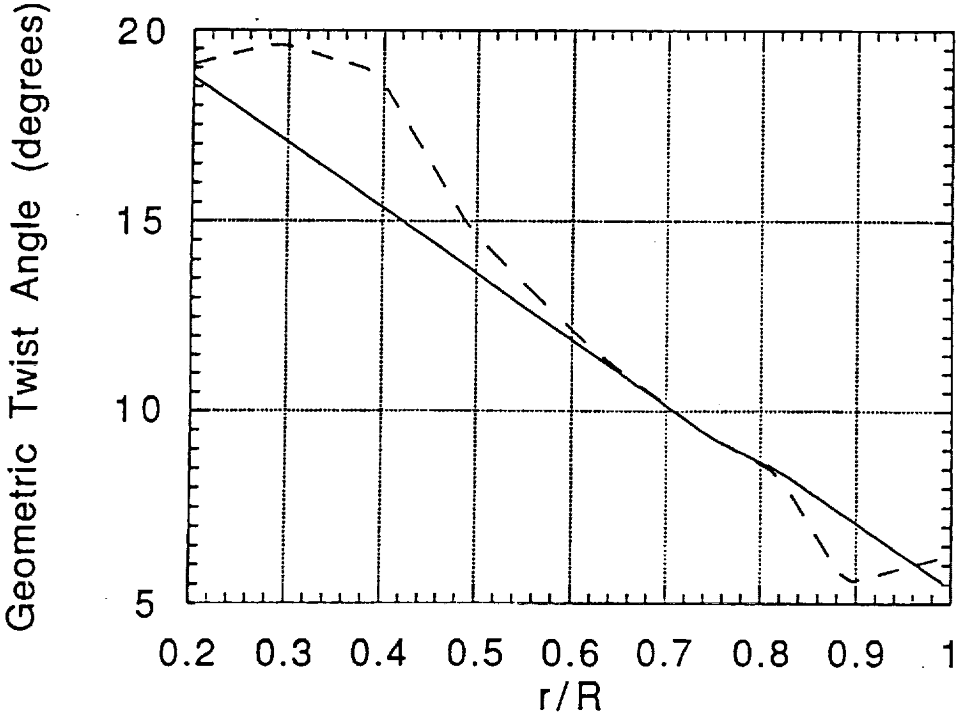

Figure 7-16. Initial (solid) and final (dashed) geometric twist distributions for the thrust maximization calculation.

adequate. The span was discretized into ten segments outboard of the cutout, each spanning 0.09R and having -4.0 degrees of washout.

The calculation was set up to maximize the propulsive efficiency at a constant thrust coefficient of 0.0085, representing a relatively heavily loaded case. All of the major design variables were allowed to participate in the optimization, including twist, chord, sweep, and anhedral. The twist was again constrained to have a maximum delta of between -8.5 and +1.5 across the segment. Chord was constrained not to decrease over the first 0.37R of the blade, but was allowed to taper down to 50% of the baseline chord outboard of this. Sweep and anhedral angles were kept at 0 degrees inboard of 0.46R and limited to +/-30 degrees outboard of this. The blades were assumed rigid, with no structural deformation included.

The improvement in propulsive efficiency over 70 optimization steps is shown in Figure 7-17, indicating that the propulsive efficiency has leveled off at roughly 0.933, representing an increment of 0.023 over the baseline value. The bound circulation distribution shown in Figure 7-18 indicates that the familiar trend to a more uniform load distribution holds here as well. The geometric twist results (Figure 7-19) show relatively modest changes, though the up-twist near the tip characteristic of the hover results does not appear.

The baseline and modified planforms are shown in Figures 7-20 and 7-21 respectively. Sweep, anhedral and chord distributions are shown in Figures 7-22 through 7-24. The axial flight case exhibits trends similar to those observed in the previous cases. The sweep and chord distributions adjust in a manner that flattens out the circulation distribution as much as possible which reduces the induced torque. This is best seen by the shape of the optimized chord distribution which is actually an inverted image of the circulation distribution. Though the sweep back will afford a small reduction in profile torque due to compressibility effects, the primary effect for rotorcraft appears to be the reduction of induced torque caused by reducing the circulation at the high speed tip. The outboard anhedral also reduces induced torque, in part by pushing the tip vortex downward away from the blade. Even though this latter effect is lessened in axial flight, the optimization algorithm will still droop the tip if any increment in performance is to be gained. This fact is important to take into consideration when analyzing optimized planforms; large excursions in sweep and anhedral often have a smaller effect on performance than minor adjustments in the twist distribution. It is these design variables having the least influence that will often change the most.

7.4 Computation Time

Design optimization calculations are inherently computationally intensive since they inevitably involve repeated calls to the performance evaluation routines. As noted earlier in this report, the formulation of the original EHPIC code helps to reduce this burden since many of the influence coefficients needed to fill the tableau used to solve the optimization problem are computed as a matter of course in the performance evaluation. Nevertheless, the computational demands of EHPIC/HERO can become substantial as the number of design degrees of freedom are increased. The overall objective of the present effort in this respect was to ensure that EHPIC/HERO was no more CPU-intensive on 1992 computational hardware than was EHPIC Mod 0.0 on 1987 hardware. Since EHPIC has gained acceptance in the rotorcraft industry for routine aerodynamic calculations, this was judged to be a reasonable criterion by which to gauge the usefulness of EHPIC/HERO.

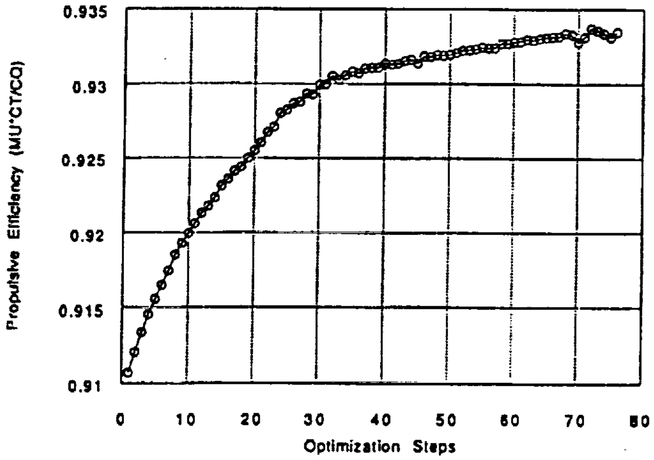

Figure 7-17. Evolution of propulsive efficiency during the design optimization of a tiltrotor in high speed axial flight.

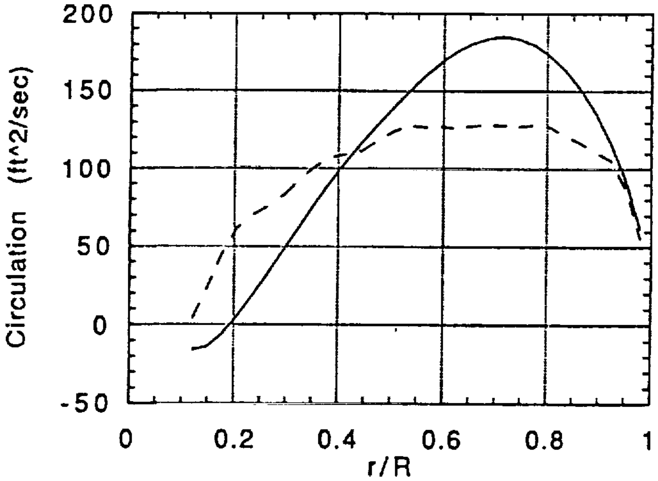

Figure 7-18. Initial (solid) and final (dashed) bound circulation for the tiltrotor propulsive efficiency calculation.

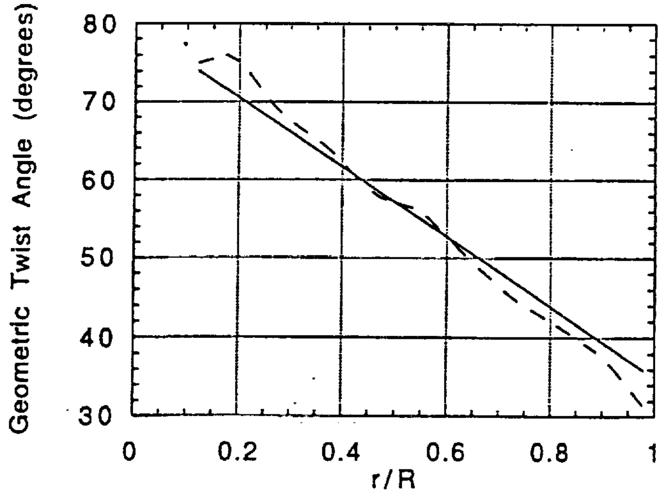

Figure 7-19. Initial (solid) and final (dashed) geometric twist distributions for the tiltrotor propulsive efficiency calculation.

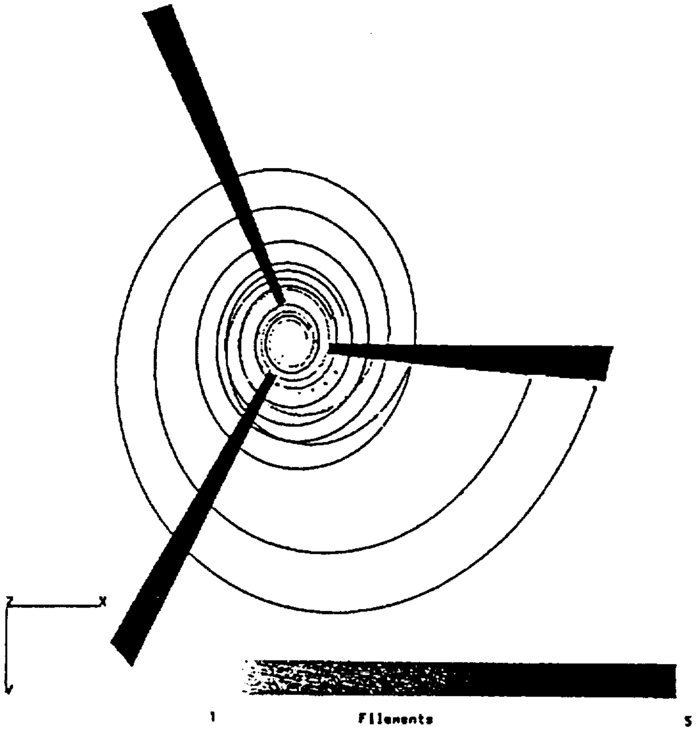

a) Baseline

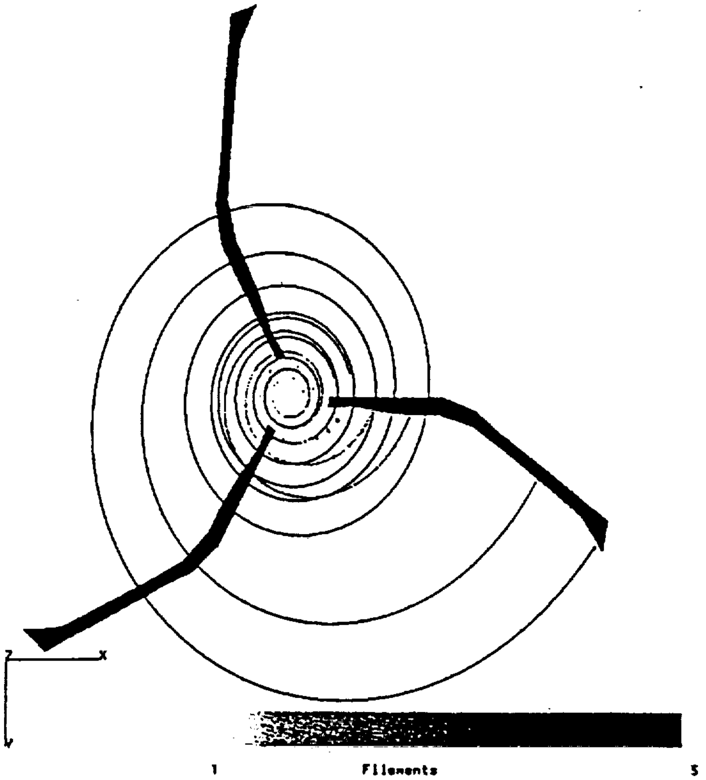

b) Final

Figure 7-20. Top view of rotor configurations for the tiltrotor propulsive efficiency maximization.

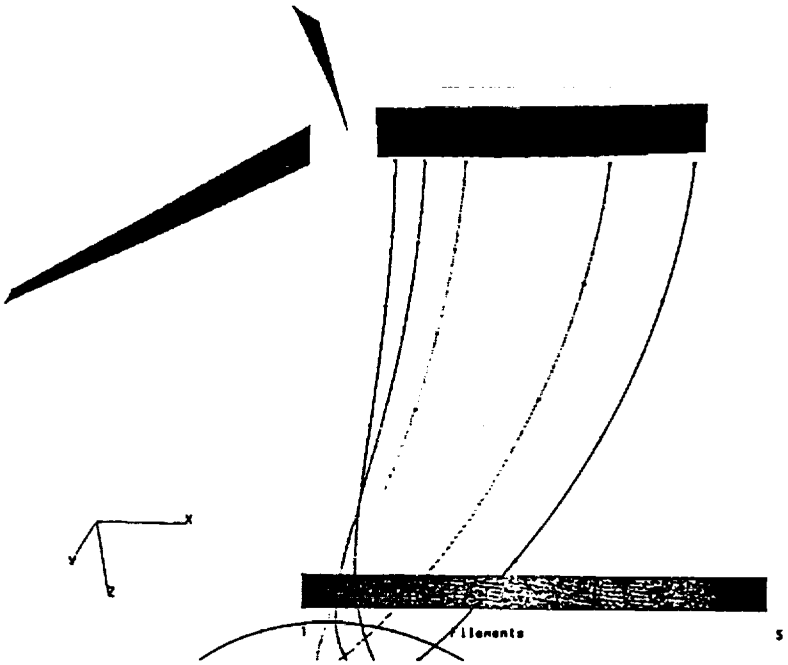

a) Baseline

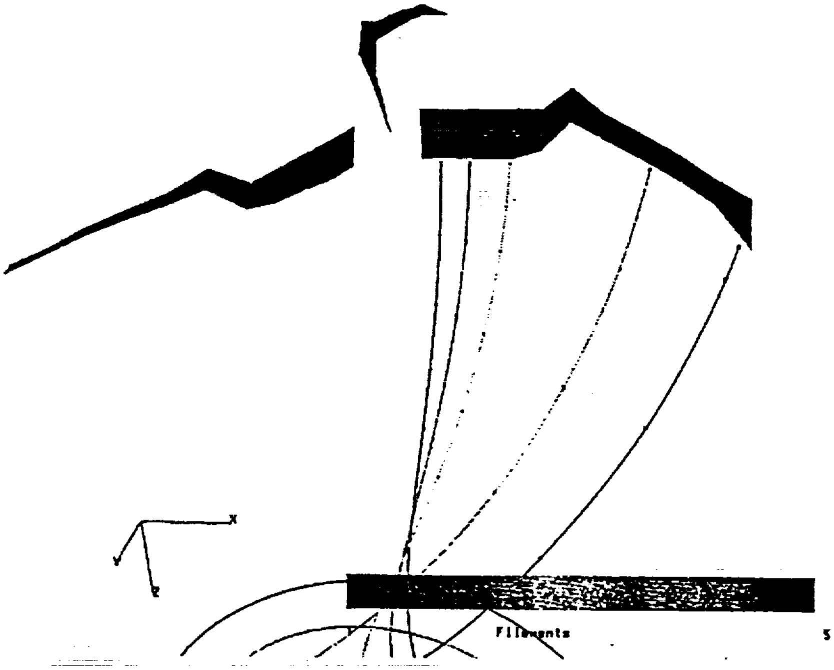

b) Final

Figure 7-21. Oblique view of rotor configurations for the tiltrotor propulsive efficiency maximization.

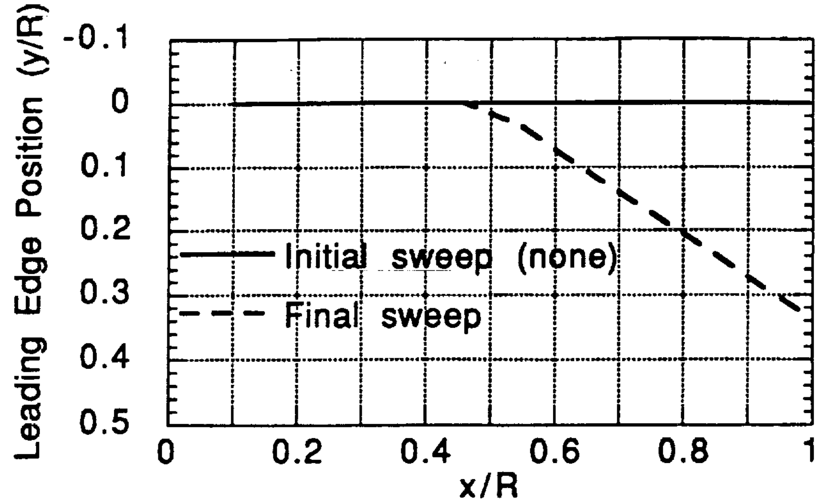

Figure 7-22. Sweep distribution optimization of a tiltrotor in high speed axial flight.

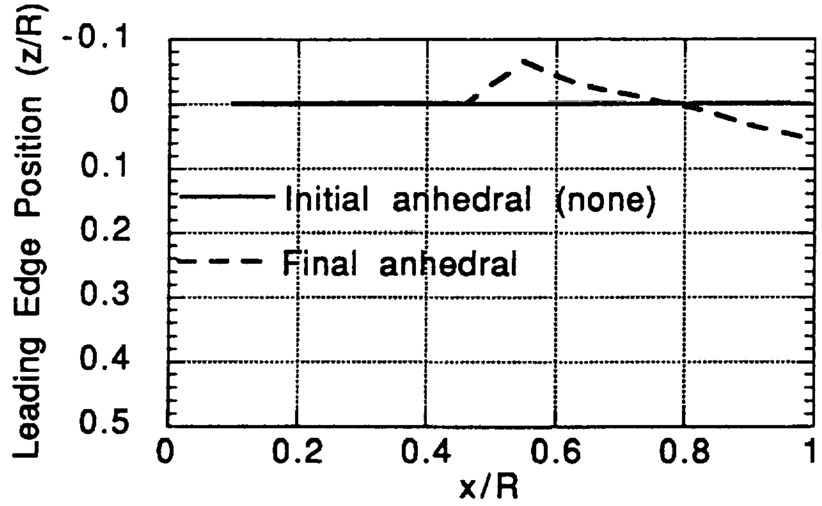

Figure 7-23. Anhedral distribution optimization of a tiltrotor in high speed axial flight.

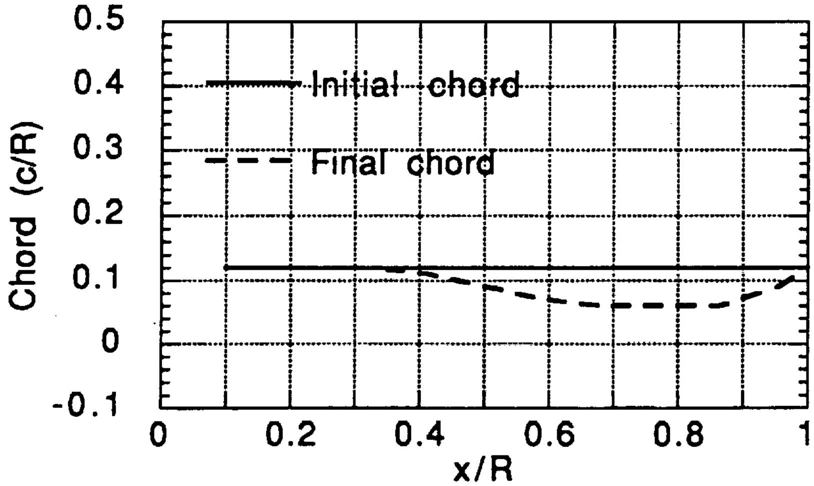

Figure 7-24. Chord distribution optimization of a tiltrotor in high speed axial flight.

This objective has been achieved. The sample calculations presented in this section typically run 6-10 CPU hours on an Iris 340 workstation. These run times are comparable to those required by complex EHPIC Mod 0.0 runs on the MicroVAX II that was originally used for EHPIC development during 1986 and 1987. Indeed, the present calculations were relatively conservative, in that they did not take full advantage of the options available to bypass updates of the optimization tableau. Each of the calculations shown in this section were run with KOPT=1, NFRAC=2, and KWIKN=2 (see Section 5 or Reference 12 for definitions of these parameters), and it is quite likely that additional speed-up could have been achieved with larger steps between updates. Even so, additional effort to improve computational efficiency would nonetheless be desirable.

8. SUMMARY

The primary purpose of this report has been to document the development and testing of the EHPIC/HERO rotor performance optimization code. EHPIC/HERO has been designed to retain the strengths of the original EHPIC free wake hover performance code while both extending its capabilities and adding wholly new features to compute structural deflection, high-resolution rotor wake flows, and, most importantly, optimized rotor designs for improved performance.

The major refinements to the basic hover model include the addition of a lift stall model, the inclusion of scan planes for induced velocity calculations, the expansion of previous table look-up routines to support structural deflection calculations, and the revision of blade/wake coupling to facilitate both optimization and high-resolution rotor wake computations. The new stall model produces the correct qualitative trends for highly loaded rotors. The results of sample calculations of time-averaged induced velocities using the new scan plane capability have likewise been promising. Implementation of a high-resolution tip wake calculation option has also been successful, and testing on representative rotor configurations has demonstrated the code's ability to capture the structure of the rolling-up wake from blades with shallow bound circulation gradients near the tip. Finally, the revised approach to coupling the blade and the wake described in Section 2 has proved to be robust, as was found in the long performance optimization runs - typically involving large changes in bound circulation - described in Section 6.

The formulation and implementation of a finite element model of the blade structure has been described. The present model uses 14-d.o.f beam/rod elements to compute bending, torsional, axial, and in-plane deflection due to blade rotation and static aerodynamic loading. Test calculations on idealized model problems have been successful and correlation with measured deflections is awaiting full analysis of recently acquired data on the UH-60A model rotor hover tests.

A combined linear programming/quadratic programming (LP/QP) approach to design optimization has been formulated and implemented. The optimization analysis accommodates all of the major planform variables as well as objective functions involving combinations of thrust, power (and its components), propulsive efficiency, or hover Figure of Merit. User-imposed constraints can be imposed on these variables in addition to performance targets based on the selected objective functions. Sequential linear programming (SLP) is the basic mode of operation of the analysis, though an SQP option exists to find optimal solutions that exist away from the constraint boundaries. Limited updating of the tableau may be invoked to reduce CPU requirements in cases where the design evolution is well-behaved.

A limited correlation study on helicopter rotors and tiltrotors in hover and axial flight has demonstrated that good accuracy can be achieved in integrated performance prediction using the EHPIC/HERO code. Demonstration calculations of the performance optimizer have also been carried out, using twist, chord, sweep, and anhedral in various combinations as design variables. In the cases examined, the optimum design obtained was a strong function of the constraints selected for that particular case (a well established feature of design optimization in general). The motivation for the constraint choices was to exercise the major features of the code in cases of practical interest; no claim is made as to the comprehensiveness of the tests undertaken here. However, two broad, interrelated trends have been identified that appear to constitute generally desirable design strategies. One of these is a manifestation of a generally well-understood feature of hover performance analysis: uniform distributions of bound circulation contribute to the minimization of rotor power for a given thrust. A qualitatively similar principle appears to be at work in both the hover thrust maximization problems studied and the sample calculations in high speed axial flight.

The second result is related to the first. Results from a wide variety of cases suggest that the addition of the 'down-up' twist or 'twist bucket' implemented on the UH-60A main rotor is a generally advantageous feature of blade design. The trend to this type of feature emerged in hovering rotor cases for combinations of twist with chord, sweep, and anhedral and for both low-twist, four-bladed rotors and high-twist, three-bladed tiltrotors. Preliminary calculations indicate this design feature evolves in power minimization problems even in cases where profile drag is excluded, suggesting that it is driven by the sensitivity of induced power to the wake-induced velocity field and the imperative to produce more uniform circulation distributions. Additional computational studies will be carried out to confirm this observation and to identify analogous strategies for other design variables.

The results and computational experience of work to date on this analysis have also pointed out the need for additional effort in a variety of areas. The full exploitation of preliminary work on inclusion of models of vortex/tip loading using ANM would aid the resolution of vortex-induced loading. Further reductions in CPU time can be realized by exploiting existing simplifications available in the present optimization analysis. The optimized designs obtained with rigid blade analyses should be repeated with structural deflection in place to examine the effect on the solutions obtained to date. The preliminary work done on including constraints on the design from forward flight conditions should be extended to enhance the realism of the hover-optimized designs. Finally, extensions to include airfoil, blade thickness effects, and structural tailoring in the design optimization should be considered to supplement the already substantial capabilities of EHPIC/HERO.

APPENDIX A

DESCRIPTION OF THE SIMPLEX ALGORITHM

A brief summary of some of the features in the present implementation of the simplex algorithm is given here. Familiarity with the fundamental terminology and steps in an LP algorithm is presumed. For a review of the basic method see References 52 and 56. We shall concern ourselves here primarily with the extensions required for implicit incorporation of upper and lower bounds upon the state variables, $\Delta\underline{X}$, and for solving QP problems. In the following, we refer to those components of $\underline{X}$ which are not at one of their specified bounds as basic variables. The remaining entries form the non-basic set.

The simplex algorithm employed here is a highly revised and extended version of the routine given in Reference 52. The routine seeks to solve the LP problem:

$$\text{Min } J = J^0 + c^T \Delta\underline{X} \tag{A-1a}$$

subject to the constraints:

$$g_j(\underline{X}) + \nabla g_j(\underline{X})\,\Delta\underline{X} \le 0 \quad \rightarrow \quad \begin{cases} \underline{b}_1 \ge [A_1]\,\Delta\underline{X} & , g_j(\underline{X}) \le 0 \\ \underline{b}_2 \ge [A_2]\,\Delta\underline{X} & , g_j(\underline{X}) > 0 \end{cases} \tag{A-1b}$$

$$g_k(\underline{X}) + \nabla g_k(\underline{X})\,\Delta\underline{X} = 0 \quad \rightarrow \quad \underline{b}_3 = [A_3]\,\Delta\underline{X} \tag{A-1c}$$

$$\Delta X_i \ge 0 \tag{A-1d}$$

where

$$\underline{b}_1 = -\{\, g_j(\underline{X}) \,\} \;;\; \underline{b}_2 = \{\, g_j(\underline{X}) \,\} \;;\; \underline{b}_3 = \{\, g_k(\underline{X}) * \text{sign}\{g_k(\underline{X})\}) \,\} \tag{A-1e}$$

and the matrices,

$$[A_1] = \nabla g_j(\underline{X}) \;;\; [A_2] = -\nabla g_j(\underline{X}) \;;\; [A_3] = -\nabla g_k(\underline{X}) * \text{sign}\{\nabla g_k(\underline{X})\} \tag{A-1f}$$

The $\underline{b}_i$ are defined so as to have all entries ≥ 0. The optimal solution is attained in two stages. In the first stage a feasible solution $\Delta\underline{X}$ satisfying the imposed constraints is obtained by the introduction of slack variables and the construction of an auxiliary cost function. At the end of this stage, the actual optimization process is performed and $\Delta\underline{X}$ varied via a sequence of pivot operations so that during each operation the cost is reduced. The process continues until no further reduction in cost is possible and thus returns with the optimal vector, $\Delta\underline{X}$.

A.1 Slack Variables and Determination of a Feasible Solution

The standard linear programming problem is posed in terms of a set of *equality* constraints and the requirement that all $\Delta x_i \ge 0$. Thus the inequality constraints are transformed into equality constraints by the introduction of slack variables, $\underline{s}_1$ and $\underline{s}_2$:

$$\underline{b}_1 = [A_1]\,\Delta\underline{X} + \underline{s}_1 \;;\; \underline{b}_2 = [A_2]\,\Delta\underline{X} - \underline{s}_2 \tag{A-2a}$$

$$\underline{s}_1, \underline{s}_2 \geq 0 \qquad \text{(A-2b)}$$

Observe that the first constraint, $\underline{b}_1 = [A_1]\,\Delta\underline{X} + \underline{s}_1$, is easy to satisfy by setting, $\Delta\underline{X}=0$, and $\underline{s}_1=\underline{b}_1$. This is due to the positivity of the components of $\underline{b}_1$. This is not generally the case for the remaining inequalities associated with $\underline{b}_2$ and $\underline{b}_3$. Thus, in order to determine a feasible solution the constraint parameters, $\underline{z}_2$ and $\underline{z}_3$, are introduced to obtain the augmented set of constraints:

$$\underline{b}_1 = [A_1]\,\Delta\underline{X} + \underline{s}_1 \;\; ; \;\; \underline{b}_2 = [A_2]\,\Delta\underline{X} - \underline{s}_2 + \underline{z}_2 \;\; ; \;\; \underline{b}_3 = [A_3]\,\Delta\underline{X} + \underline{z}_3 \qquad \text{(A-3a)}$$

$$\Delta x_i \geq 0 \;\; ; \;\; \underline{s}_1, \underline{s}_2 \geq 0 \;\; ; \;\; \underline{z}_2, \underline{z}_3 \geq 0 \qquad \text{(A-3b)}$$

Specification of an initial solution to Eqs. (A-3) is now rendered trivial and is given by:

$$\Delta\underline{X}=0 \;\; ; \;\; \underline{s}_1=\underline{b}_1 \;\; ; \;\; \underline{s}_2=0 \;\; ; \;\; \underline{s}_3=0 \;\; ; \;\; \underline{z}_2=\underline{b}_2 \;\; ; \;\; \underline{z}_3=\underline{b}_3 \qquad \text{(A-4)}$$

Since the $\underline{b}_i \geq 0$, the $\underline{s}_i \geq 0$ and $\underline{z}_i \geq 0$. Furthermore, $\{\underline{s}_1, \underline{z}_2, \underline{z}_3\}$ forms the set of basic (non-zero) variables and $\{\Delta\underline{X}, \underline{s}_2, \underline{s}_3\}$ forms the set of non-basic variables. One now has a set of equality constraints, Eq. (A-3a), subject to conditions, Eq. (A-3b) which in conjunction with an appropriate linear cost function, define a linear programming problem. To obtain a feasible solution to the original problem, Eqs. (A-1), we must first remove the constraints variables, $\underline{z}_i$, i.e., conduct pivot operations aimed at reducing $\underline{z}_i=0$, or equivalently causing the $\underline{z}_i$ to leave the basic set. Thus, the appropriate cost function to be minimized is chosen as the sum of the components of $\underline{z}_2$ and $\underline{z}_3$:

$$f_z = \sum_{m2} z_{2i} + \sum_{m3} z_{3i} \qquad \text{(A-5)}$$

where m2 and m3 are the dimensions of the vectors $\underline{z}_2$ and $\underline{z}_3$ or equivalently the dimensions of b_2 and $\underline{b}_3$ respectively. The simplex machinery involving pivot selection and pivoting operations may now be applied to this minimization problem. If the minimizing solution subject to the constraints satisfies $\min\{f_z\}=0$ then this implies that the z_{2i} and z_{3i} are zero and the corresponding original constraints are satisfied. i.e., $\underline{b}_2 = [A_2]\,\Delta\underline{X} - \underline{s}_2$, and $\underline{b}_3 = [A_3]\,\Delta\underline{X}$. The simplex pivoting strategy guarantees that the other constraints involving b_1 and the positivity requirements upon the variables is maintained. If $\min\{f_z\}>0$, then one or more of the z_{2i} or z_{3i} are positive and cannot be reduced further implying that the corresponding constraint is not satisfied. The initial value of f_z

$$f_z = \sum_{m2} b_{2i} + \sum_{m3} b_{3i} \qquad \text{(A-6)}$$

so that the progress of the simplex algorithm may be monitored by tracking the value of f_z through the sequence of simplex iterations. The function, f_z, must be expressed in terms of the non-basic variables which is easily accomplished by referring to the associated constraints:

$$\underline{z}_2 = \underline{b}_2 - [A_2]\,\Delta\underline{X} + \underline{s}_2 \;\; ; \;\; \underline{z}_3 = \underline{b}_3 - [A_3]\,\Delta\underline{X} \qquad \text{(A-7)}$$

so that:

$$f_z = \sum_{m2} b_{2i} + \sum_{m3} b_{3i} - \left(\sum_{m2} [A_2] + \sum_{m3} [A_3] \right) \Delta \underline{X} + \sum_{m2} s_{2i} \qquad \text{(A-8)}$$

This is conveniently summarized in the form of a tableau:

Table A-1

	$\Delta \underline{X}$	$\underline{s}_2$	$\underline{s}_1$	$\underline{z}_2$	$\underline{z}_3$	Basic Variables
J^0	c^T					
$\underline{b}_1$	$[A_1]_i$	$[0]$	$[I_{m1}]$	$[0]$	$[0]$	$\underline{s}_1$
$\underline{b}_2$	$[A_2]_i$	$-[I_{m2}]$	$[0]$	$[I_{m2}]$	$[0]$	$\underline{z}_2$
$\underline{b}_3$	$[A_3]_i$	$[0]$	$[0]$	$[0]$	$[I_{m3}]$	$\underline{z}_3$
f_{z0}	$\sum_k^{m2} [A_2]_{ki} + \sum_k^{m3} [A_3]_{ki}$	$-\underline{e}_{m2}^T$	$\underline{0}^T$	$\underline{0}^T$	$\underline{0}^T$	

where, $$f_{z0} = \sum_{m2} b_{2i} + \sum_{m3} b_{3i} \qquad \text{(A-9)}$$

and $\underline{e}_m$ denotes the vector of dimension m with unit entries, and $[I_m]$ is the unit matrix of order m. The bottom row may be considered as an additional equality constraint as far as the simplex pivoting operations are concerned. The last three columns in the table correspond to the basic variables and form a unit matrix of dimension (m1+m2+m3). Since pivoting operations essentially permute the unit column vectors within the tableau it is only necessary to store the remaining tableau in computer memory and keep track of the basic and non-basic variables using index lists. Thus the last three columns are not actually stored in the array used in EHPIC/HERO, which leads to an m by m reduction in memory requirements with m being the total number of constraints. Furthermore, since the column vectors in the tableau for $\underline{s}_2$ are identical to those for $\underline{z}_2$ except for sign, and the pivoting operations affect both columns in the same way, an m by m_2 reduction in tableau space is effected by tracking these also with an index list, due consideration being made for sign. Procedurally, when a given component z_{2i} leaves the basic set (i.e. becomes zero), it is replaced by the associated s_{2i} variable, and the tableau modified by reversing the sign of the associated column vector. Thus, z_{2i} is eliminated from the set of variables under consideration. When a component z_{3i} leaves the basic set it becomes a non-basic variable identified with column, j, in the tableau. Since z_{3i} is not used in subsequent computations, the column is henceforth omitted from consideration as a pivot column.

A.2 Implementation of Upper and Lower Bounds

In the above discussion a lower bound was implicitly imposed upon the Δx_i by the positivity requirements, $\Delta x_i \geq 0$. This can easily be extended to any set of lower bounds, l_i, by simple linear transformation of the defining variables. To impose upper bounds upon $\Delta \underline{X}$ the pivoting strategy is modified following the procedures outlined by Luenberger, Reference 56. Whereas in the original algorithm, the variables are referred to their lower (zero) bounds, each variable can now also be referred relative to its upper bound, UBND(i). An integer array, IBND(i) is employed to indicate which bound the variable x_i is referred to. The pivot selection procedure is now as follows. The upper bound for each variable, x_i, is set by the user (design variables, $\underline{d}$) or elsewhere in the code ($\underline{x}_c$, $\underline{y}$). The upper bound for each of the $\underline{s}_1$, $\underline{s}_2$, $\underline{z}_2$, and $\underline{z}_3$ is arbitrarily set to a large number. The same is true of the Lagrange multipliers when conducting QP problems.

1) The non-basic variable to be pivoted, x_j, is determined. This is done in the same manner as in the single bounded case and is accomplished by searching the row corresponding to f_z (when finding a feasible solution) or J (when determining the optimal solution) and finding the column, j, with minimum entry. If this value is positive then no further improvement is possible. Otherwise we proceed with the step 2).

2) There are now three possible moves a) The non-basic variable, x_j, simply goes to its opposite bound; b) x_j enters the basic set by being pivoted with a basic variable, x_i, and x_i returns to its old bound (this is the usual pivoting procedure for the single bound case); c) same as b) except that the variable x_i is brought to its *opposite* bound. To determine both the action taken and for cases b) and c) which basic variable, x_i, is to be pivoted determine the minimum of:

a) UBND(i)

b) $\min\limits_{a_{ij}>0} a_{i0}/a_{ij}$

c) $\min\limits_{a_{ij}<0} \left(a_{i0} - \text{UBND}(i) \right)/a_{ij}$

where a_{ij} is the entry in the above table corresponding to constraint, i, and nonbasic variable, j, and a_{i0} is the leftmost column entry of constraint, i.

3) Depending upon the minimum value in step 2), execute the operations associated with a), b), or c). For details of the pivot operation see Reference 56 noting that this is implemented upon the compact storage scheme of Reference 58.

A.3 Extension to QP Problems

Each of the quadratic programming problems is solved by a modified version of the simplex algorithm. The Kuhn-Tucker conditions are simply linear equality conditions and if these are satisfied together with the original imposed constraints then one has the solution to the QP problem. However, the difficulty lies in meeting the criterion, Eq. (5-14b,c), which forms a nonlinear constraint. The solution approach follows that of Wolfe (Reference 59) and involves a two stage procedure as in the LP case. In the first stage a feasible solution satisfying the original constraints is derived in an entirely analogous manner as in LP. Starting with the feasible solution thus obtained, the additional Kuhn-Tucker equality constraints are then imposed and a new feasible solution satisfying the entire set of constraints is sought. The nonlinear condition, Eq. (5-14b,c), is implicitly satisfied by modifying the logic used in selecting the pivot element in the simplex pivoting process.

The Kuhn-Tucker criteria augment the original set of imposed constraints by n further equality constraints together with the orthogonality requirements upon pairs of Lagrange multipliers and constraints. The equality constraints fall directly into the LP capability of the simplex algorithm. It is the enforcement of orthogonality between certain pairs of variables necessitates modifications of the method. Recalling the Kuhn-Tucker conditions, Eqs. (5-14):

$$\underline{0} = \nabla J(\underline{X}) + [B]\,\Delta\underline{X} + \left[A_1^T \quad -A_2^T\right]\underline{\lambda}_j + [I_n]\left(\underline{\mu}_2 - \underline{\mu}_1\right) + \left[\overline{A}_3^T\right]\underline{\lambda}_k \qquad \text{(A-10a)}$$

$$\mu_{1i}\left(\Delta x_i - \Delta l_i\right) = 0 \;\; ; \;\; \mu_{2i}\left(\Delta u_i - \Delta x_i\right) = 0 \;\; ; \;\; \mu_{1i}, \mu_{2i} \geq 0 \;, \; (i=1,\ldots,n) \qquad \text{(A-10b)}$$

$$\lambda_j s_j = 0 \;\; ; \;\; \lambda_j \geq 0 \quad (j=1,\ldots,mi) \qquad \text{(A-10c)}$$

$$\underline{\lambda}_k \text{ unbounded} \quad (k=mi+1,\ldots,me) \qquad \text{(A-10d)}$$

where $\{s_j\}=\{\underline{s}_1, \underline{s}_2\}$ are the slack variables associated with the inequality constraints, and $\left[\overline{A}_3^T\right] = [\nabla g_k(\underline{X})]^T$ and is equivalent to $A_3{}^T$ except for the sign reordering defined by Eq. (A-1b). There are n new equality constraints and m+2n new Lagrange multiplier variables. The condition $\lambda_j s_j = 0$ is equivalent to the stipulation that λ_j can only enter basic set if s_j is zero implying that the corresponding inequality constraint is active (i.e., satisfied exactly).

The Lagrange multipliers associated with the imposed equality constraints is unbounded and so can be eliminated from the set of variables by solving for them directly using m_3 of the n Kuhn-Tucker equality constraints. The matrix, $\left[\overline{A}_3^T\right]$ is partitioned,

$$\left[\overline{A}_3^T\right] = \begin{bmatrix} \overline{A}_{m3}^T \\ \overline{A}_{n-m3}^T \end{bmatrix} \qquad \text{(A-11)}$$

where the rank of $\left[\overline{A}_{m3}^T\right]$ is m3. The rows of $\left[\overline{A}_{m3}^T\right]$ are chosen by searching for maximum pivots so that $\left[\overline{A}_{m3}^T\right]$ is well conditioned. Then,

$$\underline{\lambda}_k = -\left[\overline{A}_{m3}\right]^{-T}\left\{\nabla J(\underline{X}) + [B]\Delta\underline{X} + \left[A_1^T \quad -A_2^T\right]\underline{\lambda}_j + \left(\underline{\mu}_2 - \underline{\mu}_1\right)\right\}_{m3} \qquad \text{(A-12)}$$

where the subscript $(\bullet)_{m3}$ refers to the row partitions of the argument corresponding to those of $\left[\overline{A}_{m3}^T\right]$. These equations may now be dropped from the Kuhn-Tucker conditions. The remaining n-m3 Kuhn-Tucker equations are modified by substituting for $\underline{\lambda}_k$. The reduced set of n-m3 Kuhn-Tucker conditions then takes the form:

$$\underline{0} = -\underline{c} + [Q]\,\Delta\underline{X} + [R]\,\underline{\lambda}_j + T\,(\underline{\mu}_2 - \underline{\mu}_1) \qquad \text{(A-13a)}$$

$$c_i \geq 0 \qquad \text{(A-13b)}$$

together with the original orthogonality requirements, Eqs. (A-10b,c). The matrices [Q], [R], and [T] are obtained by substituting for $\underline{\lambda}_k$ in the remaining n-m3 rows of the original Kuhn-Tucker equations, Eq. (A-10a). The condition $c_i \geq 0$ is effected by reversing the sign of each entry in row i if necessary.

In the first stage, the additional vectors, $\underline{z}_2$ and $\underline{z}_3$, are temporarily introduced as before so that an initial feasible vector satisfying all augmented imposed constraints, Eq. (A-3), can be found. Similarly, the vector, $\underline{z}_{KT}$ is introduced so that the Kuhn-Tucker equality constraints become:

$$\underline{c} = [Q]\,\Delta\underline{X} + [R]\,\underline{\lambda}_j + T\,(\underline{\mu}_2 - \underline{\mu}_1) + \underline{z}_{KT} \qquad \text{(A-14a)}$$

$$\underline{z}_{KT} \geq \underline{0} \qquad \text{(A-14b)}$$

A feasible solution vector satisfying all constraints and the orthogonality requirements is obtained by simply setting all of the Lagrange multipliers to zero, $\underline{z}_{KT}=\underline{c}$, and initializing the remaining variables as in Eqs. (A-4). The resulting tableau reads:

Table A-2

	$\Delta\underline{X}$	$\underline{s}_2$	$\underline{\lambda}_j$	$\underline{\mu}_1$	$\underline{\mu}_2$	Basic Variables
$\underline{b}_1$	$[A_1]_i$	[0]	[0]	[0]	[0]	$\underline{s}_1$
$\underline{b}_2$	$[A_2]_i$	$-[I_{m2}]$	[0]	[0]	[0]	$\underline{z}_2$
$\underline{b}_3$	$[A_3]_i$	[0]	[0]	[0]	[0]	$\underline{z}_3$
$\underline{c}$	Q_i	[0]	[R]	[-T]	[T]	$\underline{z}_{KT}$
f_{z0}	$\sum_k^{m2}[A_2]_{ki} + \sum_k^{m3}[A_3]_{ki}$	$-\{e_{m2}\}$				

where the final row is formed in exactly the same manner as in the LP case. The last three blocks of the final row are not used in stage 1. During this first stage, the Lagrange multipliers remain at their lower bounds and are skipped when determining the pivot columns. Therefore, the orthogonality requirements imposed by the Kuhn-Tucker conditions is maintained. Note however, that the pivot operations basically add multiples of the pivot row to all of the other rows so that the matrix [Q] will be modified. The matrices [R] and [T] remain unaffected since all other entries in the associated column blocks are zero.

From the above table it is clear that the columns pertaining to μ_{1i} and μ_{2i} are identical except for the sign. Also, it is clear that it is impossible to have both μ_{1i} and μ_{2i} both belong in the basic set since that would imply that the associated x_i variable is simultaneously at its upper and lower bound. The row manipulations taking place in a pivoting operation modify the columns associated μ_{1i} affect μ_{2i} in identical manners. Thus it is not necessary to represent both variables in memory since knowledge of one of the columns implies the same for the other. In practice, an integer array is used to ascertain which of the variables, μ_{1i} or μ_{2i} is currently represented in the tableau. When a column pertaining to a μ_{1i} or μ_{2i} variable is considered during the pivot selection tests, it is examined twice, first with the unaltered column and then again with all entries in the column reversed in sign. Thus an n by n reduction in memory space is realized.

The second stage tackles the Kuhn-Tucker equality constraints. Specifically, a feasible solution satisfying these equality constraints is sought. In an analogous fashion to the construction of f_z in Eq. (A-8) which was used to obtain a feasible solution for the imposed constraints, an auxiliary linear cost function is created,

$$f_{KT} = \sum_{i=1}^{n-m3} \left(\underline{z}_{KT}\right)_i \tag{A-15}$$

As before, this is expressed in terms of the non-basic variables by substituting for the $\underline{z}_{KT}$. If one examines the tableau, Table A-1, and the expression for f_z in Eq. (A-8), it is seen that the constant term, f_{z0}, is simply the column sum of the left-most column with the summation range extending over those rows corresponding to the z_{2i} and z_{3i}. Similarly, the factor associated with a given non-basic variable, x_j, in the expression for f_z can be obtained simply by summing the entries in the column above it over the same summation range. Or,

$$\left(a_z\right)_j = \sum_{i=m1+1}^{m1+m2+m3} a_{ij} \qquad (j=0, n+m1) \tag{A-16}$$

where $\underline{a}_z$ is the row in the tableau associated with f_z, j=0 corresponds to the leftmost column, i=0 corresponds the row associated with J, and j=n+m1 corresponds to the righmost non-basic variable, in this case $(s_1)_{m1}$. The same procedure is carried out for the f_{KT} with the row entries being computed as a simple sum of the associated column entries. The range of summation now extends over the n-m3 rows identified with the transformed Kuhn-Tucker conditions (i.e., subsequent to the elimination of m3 rows when solving for the unbounded $\underline{\lambda}_k$). Furthermore, the column range, j, is extended to $n+m1+n+m_i$ so that these sums are also formed for the remaining $n+m_i$ Lagrange multipliers which at this point are still non-basic variables set to their initial zero values.

$$f_z = \sum_{m2} b_{2i} + \sum_{m3} b_{3i} - \left(\sum_{m2}[A_2] + \sum_{m3}[A_3]\right)\Delta\underline{X} + \sum_{m2} s_{2i} \tag{A-17}$$

At the end of the first stage, the tableau has the form:

Table A-3

	Non-basic entries of { $\Delta\underline{X}$, $\underline{s}_1$, $\underline{s}_2$ }	λ_i	μ_1	μ_2	Basic Variables
$\begin{Bmatrix} b_1^* \\ b_2^* \\ b_3^* \end{Bmatrix}$	$\begin{bmatrix} A_1^* \\ A_2^* \\ A_3^* \end{bmatrix}$	[0]	[0]	[0]	Basic entries of { $\Delta\underline{X}$, $\underline{s}_1$, $\underline{s}_2$ }
c^*	Q_i^*	R	-T	T	$\underline{z}_{KT}$

f_{KT0}	$\sum_{k=m+1}^{m+n-m3} Q^{*}_{kj}$	$\sum_{k=m+1}^{m+n-m3} R_{kj}$	$\sum_{k=m+1}^{m+n-m3} -T_{kj}$	$\sum_{k=m+1}^{m+n-m3} T_{kj}$	

where $(\bullet)^*$ denotes that the entries have been altered due to row manipulations during pivoting. Here, the scalar,

$$f_{KT0} = \sum_{k=m+1}^{m+n-m3} c_k^* \qquad \text{(A-18)}$$

The second stage then is concerned with minimizing f_{KT}. If the optimal value of $f_{KT}=0$, then by implication all the $z_{KT}=0$ thus verifying that a feasible solution to the complete problem of imposed constraints plus the Kuhn-Tucker conditions, or equivalently, the optimizing vector of the QP problem, has been found. This presumes that the orthogonality conditions, Eqs. (A-10b,c), are maintained throughout, and this must be explicitly enforced in the second phase. To this end, a battery of logical tests is conducted during selection of the pivot column. For each candidate column, the associated non-basic variable together with its set of conjugate variables (i.e. the second in the pair of variables that define the orthogonality requirement) is found. For any x_j the set of conjugate variables is μ_{1j} and μ_{2j}; for slack variable, s_{1j} or s_{2j}, the conjugate variable is the corresponding entry of λ_j; etc. The bookkeeping is somewhat involved due to the compact storage of the simplex tableau and the implicit incorporation of lower and upper bounds upon the variables, but in essence the associated conjugate variables are tested for membership in the basic set. If the membership structure is found to be incompatible with the orthogonality stipulations, Eqs. (A-10b,c), then that column is skipped. If no column can be found that both satisfies the orthogonality conditions and decreases the auxiliary cost, f_{KT}, then the possibility of a non-basic variable pivoting with one of its own conjugate variables is examined. For example, one could pivot the non-basic x_j component with its corresponding μ_{1j} assuming that μ_{1j} presently belongs to the basic set. Such situations arise rarely in practice, and pivot columns satisfying the orthogonality conditions are usually available.

REFERENCES

1. Landgrebe, A.J.: "An Analytical Method for Predicting Rotor Wake Geometry." Journal of the American Helicopter Society, Vol. 14, No. 4, October 1969.

2. Kocurek, J.D. and Tangler, J.L.: "A Prescribed Wake Lifting Surface Analysis." Journal of the American Helicopter Society, Vol. 22, No. 1, January 1977.

3. Egolf, T.A. and Landgrebe, A.J.: "Helicopter Wake Geometry and Its Influence in Forward Flight." NASA CR 3726, October 1983.

4. Quackenbush, T.R., Wachspress, D.A., Kaufman, A.E., and Bliss, D.B.: "Performance Optimization for Rotors in Hover and Axial Flight." Continuum Dynamics, Inc. Report No. 88-10, November 1988.

5. Quackenbush, T.R., Wachspress, D.A., and Kaufman, A.E.: "Optimization of Rotor Performance in Hover Using a Free Wake Analysis." Journal of Aircraft, Vol. 28, No. 3, March 1991. pp. 200-207.

6. Felker, F.F., Quackenbush, T.R., Bliss, D.B., and Light, J.L.: "Comparisons of Predicted and Measured Rotor Performance in Hover Using a New Free Wake Analysis." Proceedings of the 44th Annual Forum of the American Helicopter Society, June 1988.

7. Shanley, J.P., Moffitt, R.C., and Davis, S.J.: "Systematic Correlation of the EHPIC Hover Analysis." Proceedings of the 46th Annual Forum of the American Helicopter Society, May 1990.

8. Quackenbush, T.R., Bliss, D.B., and Wachspress, D.A.: "New Free-Wake Analysis of Rotorcraft Hover Performance Using Influence Coefficients." Journal of Aircraft, Vol. 26, No. 12, December 1989. pp. 1090-1097.

9. Quackenbush, T.R., Bliss, D.B., Wachspress, D.A., and Ong, C.C.: "Free Wake Analysis of Hover Performance Using a New Influence Coefficient Method." NASA CR 4309, July 1990.

10. Quackenbush, T.R. and Wachspress, D.A.: "Enhancements to a New Free Wake Hover Analysis." NASA CR 177523, April 1989.

11. Light, J.S.: "Tip Vortex Geometry of a Hovering Helicopter Rotor in Ground Effect." Proceedings of the 45th Annual Forum of the American Helicopter Society, May 1989. pp. 551-562.

12. Wachspress, D.A., Quackenbush, T.R., and Boschitsch, A.H.: "EHPIC/HERO (Mod 0.0) User's Manual." Continuum Dynamics, Inc. Technical Note No. 92-05, April 1992.

13. Miura, H.: "Applications of Numerical Optimization Methods to Helicopter Design Problems - A Survey." Vertica ,Vol. 9, No. 2, 1985. pp. 141-154.

14. Sobieszczanski-Sobieski, J.: "Sensitivity Analysis and Multidisciplinary Optimization for Aircraft Design: Recent Advances and Results." Journal of Aircraft, Vol. 27, No. 12, December 1990. pp. 993-1001.

15. Moffitt, R.C. and Bissell, J.R.: "Theory and Application of Optimum Airloads to Rotors in Hover and Forward Flight." Proceedings of the 38th Annual Forum of the American Helicopter Society, May 1982. pp. 1-12.

16. Nagashima, T. and Nakaniski, K.: "Optimum Performance and Wake Geometry of a Coaxial Rotor in Hover." Vertica, Vol. 7, No. 3, 1983. pp. 225-239.

17. Walsh, J.L., Bingham, G.J., and Riley, M.F.: "Optimization Methods Applied to the Aerodynamic Design of Helicopter Rotor Blades." Journal of the American Helicopter Society, Vol. 32, No. 4, Oct. 1987.

18. Chattopadhyay, A., Walsh, J.L., and Riley, M.F.: "Integrated Aerodynamic Load/Dynamic Optimization of Helicopter Rotor Blades." Journal of Aircraft, Vol. 28, No. 1, January 1991. pp. 58-65.

19. Mantay, W.R. and Adelman, H.A.: "Status of Research on Multidisciplinary Rotorcraft Optimization at the Langley Research Center." Proceedings of the 46th Annual Forum of the American Helicopter Society, May 1990. pp. 471-481.

20. Chattopadhyay, A. and McCarthy, T.R.: "Optimum Design of Helicopter Rotor Blades with Multidisciplinary Couplings." AIAA Paper 92-0214, January 1992.

21. Scully, M.P.: "Computation of Helicopter Rotor Wake Geometry and Its Influence on Rotor Harmonic Airloads." MIT ASRL TR 178-1, March 1975.

22. Landgrebe, A.J.: "An Analytical and Experimental Investigation of Helicopter Rotor Hover Performance and Wake Geometry Characteristics." USAAMRDL TR 71-24, June 1971.

23. Bliss, D. B., Teske, M.E., and Quackenbush, T.R.: "A New Methodology for Free Wake Analyses Using Curved Vortex Elements." NASA CR 3958, December 1987.

24. Margason, R.J. and Lamar, J.E.: "Vortex Lattice FORTRAN Program for Estimating Subsonic Aerodynamic Characteristics of Complex Planforms." NASA TN-D 6142, February 1971.

25. Chiu, Y.D.: "Convergence of Discrete-Vortex Induced-Flow Calculations by Optimum Choice of Mesh." Ph.D. Thesis, Georgia Institute of Technology, School of Aerospace Engineering, August 1988.

26. Hough, G.R.: "Lattice Arrangement of Rapid Convergence." Vortex Lattice Utilization, NASA SP-405, May 1976. pp. 325-342

27. Felker, F.F., Signor, D.B., Young, L.A., and Betzina, M.D.: "Performance and Loads Data From a Hover Test of a 0.658-Scale V-22 Rotor and Wing." NASA TM 89419, April 1987.

28. Bliss, D.B. and Miller, W.O.: "Efficient Free Wake Calculations Using Analytical/Numerical Matching and Far Field Linearization." Proceedings of the 45th Annual Forum of the American Helicopter Society, May 1989. pp. 253-263

29. Bliss, D. B. and Miller, W.O.: "Vortex Filament Calculations by Analytical/ Numerical Matching with Comparison to Other Methods." AIAA Paper 89-1962, presented at the AIAA 20th Fluid Mechanics Conference, June 1989.

30. Bliss, D.B.: "Prediction of Tip Vortex Self-Induced Motion Parameters in Terms of Rotor Blade Loading." Proceedings of the American Helicopter Society National Specialists' Meeting on Aerodynamics and Aeroacoustics, February 1987.

31. Johnson, W.: "A Lifting-Surface Solution for Vortex-Induced Airloads." AIAA Journal, Vol. 9, No. 4, April 1971. pp. 689-695.

32. Djojodihardjo, R.H. and Widnall, S.E.: "A Numerical Method for the Calculation of Nonlinear, Unsteady Lifting Potential Flow Problems." AIAA Journal, Vol. 7:2001-2009, 1969. No. 10, October 1969, pp. 2001-2009

33. Magnus, A.E. and Epton, M.A.: "PANAIR: A Computer Program for Predicting Subsonic or Supersonic Linear Potential Flows about Arbitrary Bodies." NASA-CR-3251, November 1981.

34. Ueda, T. and Dowell, E.H.: "A New Solution Method for Lifting Surfaces in Subsonic Flow." AIAA Journal, Vol. 20, No. 3, March 1982. pp. 348-355.

35. Biggers, J.C., Lee, A., Orloff, K.L., and Lemmer,. O.J.: "Laser Velocimeter Measurements of Two-Bladed Helicopter Rotor Flow Fields." NASA TM X-73238, May 1977.

36. Chigier, N.A. and Corsiglia, V.R.: "Tip Vortices; Velocity Distributions." NASA TM X-62, September 1971. NASA TM X-62087.

37. Norman, T.R. and Light, J.S.: "Rotor Tip Vortex Geometry Measurements Using the Wide-Field Shadowgraph Technique." Journal of the American Helicopter Society, Vol. 32, No. 2, April 1987.

38. Nikolsky, A.A. and Gray, R.B.: "An Aerodynamic Analysis of a Single-Bladed Rotor in Hovering and Low-Speed Forward Flight as Determined from Smoke Studies of the Vorticity Distribution in the Wake." Princeton University Aeronautical Engineering Department Report No. 356, September 1956.

39. Tung, C. and Branum, L.: "Model Tilt-Rotor Hover Performance and Surface Pressure Measurement." Proceedings of the 46th Annual Forum of the American Helicopter Society, May 1990. pp. 785-796.

40. Bilanin, A.J. and Donaldson, C. duP.: "Estimation of Velocities and Roll-Up in Aircraft Vortex Wakes." Journal of Aircraft, Vol. 12, No. 7., July 1975. pp. 578-585.

41. Strawn, R.C.: "Wing Tip Vortex Calculations with an Unstructured Adaptive-Grid Euler Solver." Proceedings of the 47th Annual Forum of the American Helicopter Society, May 1991. pp. 65-76.

42. Kandil, O.A., Wong, T.-C., and Liu, C.H.: "Analysis and Computation of Trailing Vortices and Their Hazardous Effects." Proceedings of the FAA International Wake Vortex Symposium, Washington, D.C., October 1991.

43. Hackbusch, W.: "Introduction to Multi-grid Methods for the Numerical Solution of Boundary Value Problems." *Computational Methods for Turbulent, Transonic, and Viscous Flows* (ed., Essers, J.A.), Springer-Verlag, New York, 1981. pp. 45-92.

44. Mendenhall, M.R., Spangler, S.B. and Perkins, S.C., Jr.: "Vortex Shedding from Circular and Non-Circular Bodies at High Angle of Attack." AIAA-79-0026, 1979.

45. Felker, F.F., Betzina, M.D., and Signor, D.B.: "Performance and Loads Data from A Hover Test of a Full-Scale XV-15 Rotor." NASA TM 86833, 1985.

46. Spalart, P.R.: "Numerical Simulation of Separated Flows." Ph.D. Thesis, Stanford University, 1982.

47. Bryson, A.E.: "Symmetric Vortex Separation on Circular Cylinders and Cones." Journal of Applied Mechanics, Series E, Vol. 26, No. 4, Dec. 1959. pp. 643-648.

48. Pullin, D.: "The Large-Scale Structure of Unsteady Self-Similar Rolled-Up Vortex Sheets." Journal of Fluid Mechanics, Vol. 88, October 13, 1978. pp. 401-430.

49. Celi, R. and Friedmann, P.P.: "Aeroelastic Modeling of Swept Tip Rotor Blades Using Finite Elements." Journal of the American Helicopter Society, Vol. 33, No. 2, April 1988.

50. A.C. Hindmarsh: "Banded Linear Systems with Pivoting." Lawrence Livermore Laboratory Report UCID-30045, 1972.

51. G.N. Vanderplaats: *Numerical Optimization Techniques for Engineering Design: With Applications*, McGraw-Hill Book Co., New York, 1984.

52. Press, W.H., Brian, B.P., Teukolsky, S.A., and Vetterling, W.T.: *Numerical Recipes*, Cambridge University Press, 1986.

53. Topping, B.H.V. and Robinson, D.J.: "Selecting Nonlinear Optimization Techniques for Structural Design." Engineering Computation, Vol. 1, September 1984.

54. Bertsekas, D.P.: *Constrained Optimization and Lagrange Multiplier Methods*, Academic Press, New York, 1982.

55. Powell, M.J.D.: "The Convergence of Variable Metric Methods for Nonlinearly Constrained Optimization Calculation." *Nonlinear Programming 3*, (eds., Mangasarian, O.L., Meyer, R. and Robinson, S.), Academic Press, New York, 1978.

56. Luenberger, D.G.: *Introduction to Linear and Nonlinear Programming*, Addison-Wesley Publishing Company, Reading, Massaachusetts, 1973.

57. Dhingra, A.K., Rao, S.S., and Miura, H.: "Multiobjective Decision Making in a Fuzzy Environment with Applications to Helicopter Design." AIAA Journal, Vol. 28 , No. 4, April 1990. pp. 703-710.

58. Künzi, H.P., Tzschach, H.G., and Zehnder, C.A.: *Numerical Methods of Mathematical Optimization*, Academic Press, New York, 1971.

59. Wolfe, P.: "Methods of Nonlinear Programming." *Recent Advances in Mathematical Programming*, (eds., Graves, R.L and Wolfe, P.), McGraw-Hill, New York, 1963.

60. Tung, C. and Ramachandran, K.: "Hover Performance Analysis of Advanced Rotor Blades." Proceedings of the 48th Annual Forum of the American Helicopter Society, June 1992. pp. 1367-1384.

61. Carpenter, P.J.: "Lift and Profile-Drag Characteristics of an NACA 0012 Airfoil Section as Derived from Measured Helicopter-Rotor Hovering Performance." NACA TN-4357, September 1958.

62. Davenport, F.J., Magee, J.P., and Austin, E.E.: "Analysis of Propeller and Rotor Performance in Static and Axial Flight by an Explicit Vortex Influence Technique." The Boeing Co. Vertol Division Report No. R-372, December 1967.

63. Lorber, P.F., Stauter, R.C., Pollack, M.J., and Landgrebe, A.J.: "A Comprehensive Hover Test of the Airloads and Airflow of an Extensively Instrumented Model Helicopter Rotor: Volume I - Rotor Airloads and Performance." USAAVSCOM TR 91-D-16A, October 1991.

64. Lorber, P.F., Stauter, R.C., Pollack, M.J., and Landgrebe, A.J.: "A Comprehensive Hover Test of the Airloads and Airflow of an Extensively Instrumented Model Helicopter Rotor: Volume IV - Correlation of a Lifting Line and a Lifting Surface Method With Model Rotor Hover Data." USAAVSCOM TR 91-D-16D, November 1991.

65. Lorber, P.F., Stauter, R.C., Pollack, M.J., and Landgrebe, A.J.: "A Comprehensive Hover Test of the Airloads and Airflow of an Extensively Instrumented Model Helicopter Rotor: Volume V - Supplemental Graphical and Tabulated Data." USAAVSCOM TR 91-D-16E, October 1991.

66. Felker, F.F.: "Results From a Test of a 2/3-Scale V-22 Rotor and Wing in the 40- by 80-Foot Wind Tunnel." Proceedings of the 47th Annual Forum of the American Helicopter Society, May 1991.

67. Felker, F.: Private Communication, February 1992.

REPORT DOCUMENTATION PAGE

Form Approved
OMB No. 0704-0188

1. AGENCY USE ONLY *(Leave blank)*

2. REPORT DATE
April 1993

3. REPORT TYPE AND DATES COVERED
Contractor Report

4. TITLE AND SUBTITLE
Rotor Design Optimization Using a Free Wake Analysis

5. FUNDING NUMBERS
505-59-36

6. AUTHOR(S)
Todd R. Quackenbush, Alexander H. Boschitsch,
Daniel A. Wachspress, and Kiat Chua

7. PERFORMING ORGANIZATION NAME(S) AND ADDRESS(ES)
Continuum Dynamics, Inc.
P.O. Box 3073
Princeton, NJ 08543

8. PERFORMING ORGANIZATION REPORT NUMBER
A-93050

9. SPONSORING/MONITORING AGENCY NAME(S) AND ADDRESS(ES)
National Aeronautics and Space Administration
Washington, DC 20546-0001

10. SPONSORING/MONITORING AGENCY REPORT NUMBER
NASA CR-177612
NAS2-13092

11. SUPPLEMENTARY NOTES
Point of Contact: Jeffrey Light, Ames Research Center, MS T-042, Moffett Field, CA 94035-1000;
(415) 604-4881

12a. DISTRIBUTION/AVAILABILITY STATEMENT
Unclassified — Unlimited
Subject Category 02

12b. DISTRIBUTION CODE

13. ABSTRACT *(Maximum 200 words)*

The aim of this effort has been to develop a comprehensive performance optimization capability for tiltrotor and helicopter blades. The analysis incorporates the validated EHPIC (Evaluation of Hover Performance using Influence Coefficients) model of helicopter rotor aerodynamics within a general linear/quadratic programming algorithm that allows optimization using a variety of objective functions involving the performance. The resulting computer code, EHPIC/HERO (HElicopter Rotor Optimization), improves upon several features of the previous EHPIC performance model and allows optimization utilizing a wide spectrum of design variables, including twist, chord, anhedral, and sweep. The new analysis supports optimization of a variety of objective functions, including weighted measures of rotor thrust, power and propulsive efficiency. The fundamental strength of the approach is that an efficient search for improved versions of the baseline design can be carried out while retaining the demonstrated accuracy inherent in the EHPIC free wake/vortex lattice performance analysis. Sample problems are described that demonstrate the success of this approach for several representative rotor configurations in hover and axial flight. The present report also discusses features that have been introduced to convert earlier demonstration versions of this analysis into a generally applicable tool for researchers and designers.

14. SUBJECT TERMS
Design optimization, Rotor performance, Free wake analysis

15. NUMBER OF PAGES
132

16. PRICE CODE
A07

17. SECURITY CLASSIFICATION OF REPORT
Unclassified

18. SECURITY CLASSIFICATION OF THIS PAGE
Unclassified

19. SECURITY CLASSIFICATION OF ABSTRACT

20. LIMITATION OF ABSTRACT